Modelling dust liberation in bulk material handling systems

Derakhshani, Sayed Mohammadebrahim

DOI
10.4233/uuid:0d8c6401-fc4e-4b7b-babc-6eb9573d79b3

Publication date
2016

Document Version
Final published version

Citation (APA)
Derakhshani, S. M. (2016). *Modelling dust liberation in bulk material handling systems*. [Dissertation (TU Delft), Delft University of Technology]. https://doi.org/10.4233/uuid:0d8c6401-fc4e-4b7b-babc-6eb9573d79b3

Modelling Dust Liberation in Bulk Material Handling Systems

Sayed Mohammadebrahim DERAKHSHANI

Modelling Dust Liberation in Bulk Material Handling Systems

Proefschrift

ter verkrijging van de graad van doctor
aan de Technische Universiteit Delft,
op gezag van de Rector Magnificus prof. ir. K.C.A.M. Luyben,
voorzitter van het College voor Promoties,
in het openbaar te verdedigen op
dinsdag 3 mei 2016 om 10.00 uur

door

Sayed Mohammadebrahim DERAKHSHANI

Master of Science in Mechanical Engineering, Iran University of Science and Technology, Iran
geboren te Isfahan, Iran.

Dit proefschrift is goedgekeurd door de
Promotor: Prof. dr. ir. G. Lodewijks
Copromotor: Dr. ir. D. L. Schott

Samenstelling promotiecommissie:

Rector Magnificus,	voorzitter
Prof. dr. ir. G. Lodewijks,	Technische Universiteit Delft, promotor
Dr. ir. D. L. Schott,	Technische Universiteit Delft, copromotor

Independent members:

Prof. dr. ir. B. J. Boersma,	Technische Universiteit Delft
Prof. dr. ir. J. R. van Ommen,	Technische Universiteit Delft
Prof. dr. Ing. A. Katterfeld,	Universitat Magdeburg
Prof. dr. ir. J. A. M. Kuipers,	Technische Universiteit Eindhoven
Dr. ir. A. Thornton,	Universiteit Twente

Sayed Mohammadebrahim Derakhshani,
Modelling Dust Liberation in Bulk Material Handling Systems,
Ph.D. Thesis Delft University of Technology, with summary in Dutch.

Published and distributed by: Sayed Mohammadebrahim Derakhshani
E-mail: e.derakhshani@gmail.com

Keywords: Dust liberation phenomenon, Discrete Element Method (DEM), Computational Fluid Dynamics (CFD), Conveyor, Transfer point.

ISBN 978-94-6186-643-1
Printed in the Netherlands.

To my lovely wife

"Even under the assumption that God's existence is unlikely, the potential benefits of believing are so vast as to make betting on theism rational."

Blaise Pascal, 1623-1662

Contents

Chapter

1

Introduction

Dust consists of suspended particles in the atmosphere that can be liberated from different origins by anything, from human activity and atmospheric events to industrial processes [1, 2]. Industrial dust is one of the main types of dust, which is liberated from a variety of sources, such as unsealed surfaces, dry bulk material handling equipment, bulk storage terminals, construction, agricultural activities and mining industries [3–6].

Dust has negative effects on the environmental conditions, human health as well as industrial equipment and processes [7]. It is reported by Witt et al. [8] that spillage of materials from the belt conveyor systems in the bulk storage terminals is in the order of 1.5% and it can increase maintenance costs by up to 20%. The Royal Institute of technology in Sweden performed a study on 40 plants to determine the amount of material losses during the handling process. It was indicated that the value of the bulk material spillage during the handling process reaches nearly 0.2 $wt\%$. Also, the other costs such as the cost of labor devoted to cleaning up spillage, cost of medical check-ups for personnel due to dusty environment should be added to the mentioned costs [9, 10].

1.1 Dust liberation phenomenon

Glossary of Atmospheric Chemistry Terms [11] defines dust as: “Small, dry, solid particles projected into the air by natural forces, such as wind, volcanic eruption, and by mechanical or man-made processes such as crushing grinding milling, drilling, demolition, shovelling, conveying, screening, bagging, and sweeping.”.

Figure 1.1 shows how Handbook of Chemistry and Physics [12] categorized the particles

based on their size into three types of dust, namely, suspended atmospheric dust, settling atmospheric dust, and heavy industrial dust.

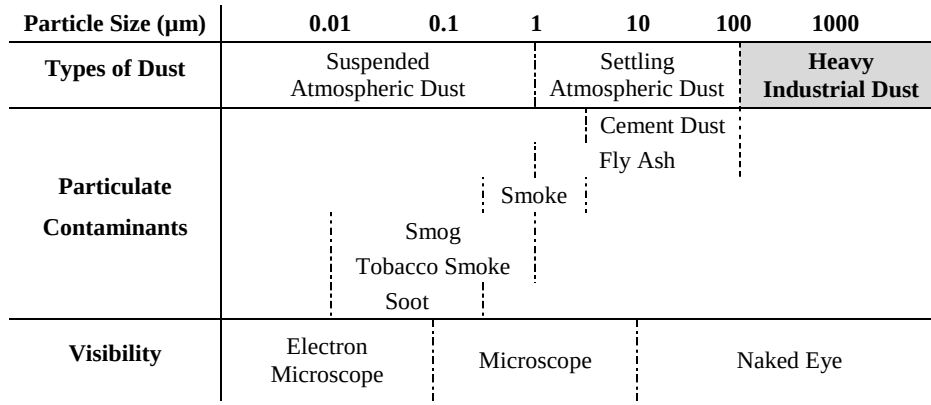

Figure 1.1: Categorization of dust according to the particle size and visibility of particles.

The first two types of dust have no significant effect on the hydrodynamic properties of airflow [13], while the heavy industrial dust, along with the larger particles can affect the hydrodynamic of airflow, for example, at the transfer point of a belt conveyor with the discharge trajectory of materials. Hence, particles with the diameters in the range 100-1000 μm not only have the ability to be liberated as the heavy industrial dust into the surrounding air, but also affect the hydrodynamics of the airflow.

The transfer point of a belt conveyor is a place with a very high potential for dust to be liberated [14], see Figure 1.2. Heavy industrial dust can be liberated from the discharge trajectory of the materials due to the interaction between the dry bulk materials and the bulk material handling systems. As a result of these collisions, some fine particles are liberated from the discharge trajectory and are carried with the airflow into the surrounding air as dust.

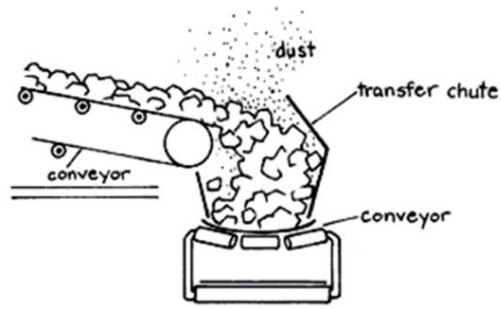

Figure 1.2: Schematic picture of dust liberation at the transfer point of a belt conveyor.

Due to undesirable effects of dust, minimizing the rate of dust liberation at the transfer point has been a major issue in the design of transfer points from the beginning of invention of belt conveyors [9]. This problem has not been solved yet and it is of importance to employ

a reliable and cost effective tool in studying the dust liberation in the field of bulk material handling systems. This tool will help designers to minimize the rate of dust liberation from a bulk material handling system beforehand of construction process through modifying its design.

A number of factors that can change the rate of dust liberation at the transfer point of a belt conveyor are the material properties, the design of conveyor, the inter-particle collisions, the interaction between particles and equipment, and the surrounding air effect [15–19]. In this study, a selected tool is utilized to study and investigate the effect of these factors on the dust liberation at the transfer point of a belt conveyor.

1.2 Thesis objectives and research question

Having a good understanding of the dust liberation phenomenon helps to prevent dust liberation or to minimize its negative effects on the environment, the equipment and human health. Industrial dust are considered as one of the sources of dust which is widely liberated from the bulk material handling systems during the transportation process. This study will focus on the transfer point of a belt conveyor to determine which factors should be considered in the design of a belt conveyor to decrease dust liberation at the transfer point.

The scientific techniques such as experimental investigations and numerical methods are existing cost-effective ways that are employed as reliable tools in studying the dust liberation phenomenon. A number of advantages of numerical methods compared to experimental investigations are the lower cost of numerical methods compared to the experimental investigations, the possibility of extracting more detailed information from the numerical results, and the relative ease of performing a simulation whereas it is difficult to repeat an experiment. Hence, the numerical techniques are considered as the affordable ways for studying the dust liberation and make it possible to identify the factors that have influence on the dust liberation. Indeed, numerical techniques give designers the opportunity to optimize the design of equipment before construction and minimize the rate of dust liberation from a belt conveyor.

In this thesis, a numerical method will be chosen and employed to simulate the dust liberation at the transfer point of a belt conveyor. Accordingly, the dust liberation at the transfer point will be numerically studied and its dispersion into the surrounding air of the conveyor will be investigated.

The objective of this research is to take the advantages of numerical methods as reliable design tools in modelling the material transportation at the transfer point of a belt conveyor. In this way, the factors that have the potential in changing the rate of dust liberation will be identified by a numerical technique and the dust liberation at this point will be numerically modelled. Accordingly, the main research questions of this thesis are defined as follows:

“1. What numerical method can be employed as a tool in studying the dust liberation in bulk material handling systems?”

“2. How to assess the validation of the selected numerical method for the application of dust liberation modelling?”

“3. Which factors should be considered in the design of the transfer point of a belt conveyor?”

1.3 Research methodology

A number of studies have been conducted in the past years with the aim of modelling dust liberation at the transfer point of conveyors with numerical techniques [8, 15, 20–23]. In this study, a literature review will be conducted to answer for the first main question of this research and then the proper numerical method for simulating dust liberation at the transfer point of a convener will be selected.

On the other side, numerical models need to be calibrated and validated with reliable data to ensure that they are realistic tools for simulating the natural phenomena and industrial processes. In this thesis, a series of experiments and simulations will be conducted to determine the parameters and sub-models of the numerical method and then the numerical model will be validated for the application of dust liberation modelling. In this way, the second main research question of this research will be answered.

Finally, the numerical model together with the experimental investigations will be used to determine the discharge trajectory of materials at the transfer point of a belt conveyor. Through this way, the numerical model will be re-evaluated based on the experimental results of a conveyor system. In addition, a series of simulations will be conducted to investigate which factors should be considered in the design of the transfer point of a belt conveyor. As a result, the third main research question of this thesis will be answered.

1.4 Outline of thesis

In this thesis, the dust liberation at the transfer point of a belt conveyor will be modelled with a numerical method. The outline of the thesis is structured as follows:

In Chapter 2, the numerical techniques will be reviewed in detail to select a suitable method for modelling the dust liberation at the transfer point of a belt conveyor. The numerical techniques are compared with each other from the viewpoint of accuracy and computational effort as well as the ability of modelling the particle phase. At the end, the theoretical framework of the selected model will be presented in detail.

In Chapter 3, the Discrete Element Method (DEM)-Computational Fluid Dynamics (CFD) coupling technique that was proposed in Chapter 2 will be utilized in modelling a Single Particle Sedimentation (SPS) within three types of fluid. In this way, the CFD-DEM parameters (the CFD cell size and coupling interval) will be calibrated and the proper CFD-DEM sub-models (drag force and voidage models) will be selected. Also, the optimum ratio of the particle diameter to the CFD cell size ($D_p/\Delta x$) and the critical ratio of the domain width to the particle diameter (W/D_p) will be determined in this chapter.

In Chapter 4, the validated CFD-DEM model of Chapter 3 will be re-evaluated for a dense regime of particles flow in which the inter-particle collisions will be considered in the simulation. Also, the microscopic and macroscopic properties of quartz sand will be determined through experimental studies and numerical investigations. The DEM and CFD-DEM models will be employed to determine the coefficients of rolling and sliding friction between the sand particles ($\mu_{r,pp}$ and $\mu_{s,pp}$). In the last part of this chapter, the effect of DEM boundary condition on the computational time will be investigated through utilizing a slice of DEM domain instead of the whole domain in a way that the slice of material represents the realistic mechanical behaviour of materials.

In Chapter 5, the validated CFD-DEM model of Chapter 4 will be checked through modelling a dense regime of particles flow inside a fluidized bed. The interaction between the airflow and sand particles will be experimentally and numerically studied to finalize the validation process of the CFD-DEM model. The Coefficient of Restitution (CoR) between the sand particles together with the coefficients of rolling and sliding friction between the sand particles and wall ($\mu_{r,pw}$ and $\mu_{s,pw}$) will be determined in this chapter.

In Chapter 6, the CFD-DEM model of Chapter 4 will be utilized in simulating the discharge trajectory of sand particles at the transfer point a belt conveyor. The basic principles of dust liberation at the transfer points will be reviewed in this chapter. Also, a series of experiments and simulations will be conducted to determine the coefficients of rolling and sliding friction between the sand particles and belt conveyor ($\mu_{r,pb}$ and $\mu_{s,pb}$). At the end, the effective factors on the dust liberation at the transfer point such as the size and density of particles, the velocity and direction of airflow, and the viscous effects near the belt conveyor are numerically modelled and studied.

Finally, in Chapter 7, the conclusions of this research and the recommendations for the future researches are presented. The flowchart of this PhD thesis is represented in Figure 1.3.

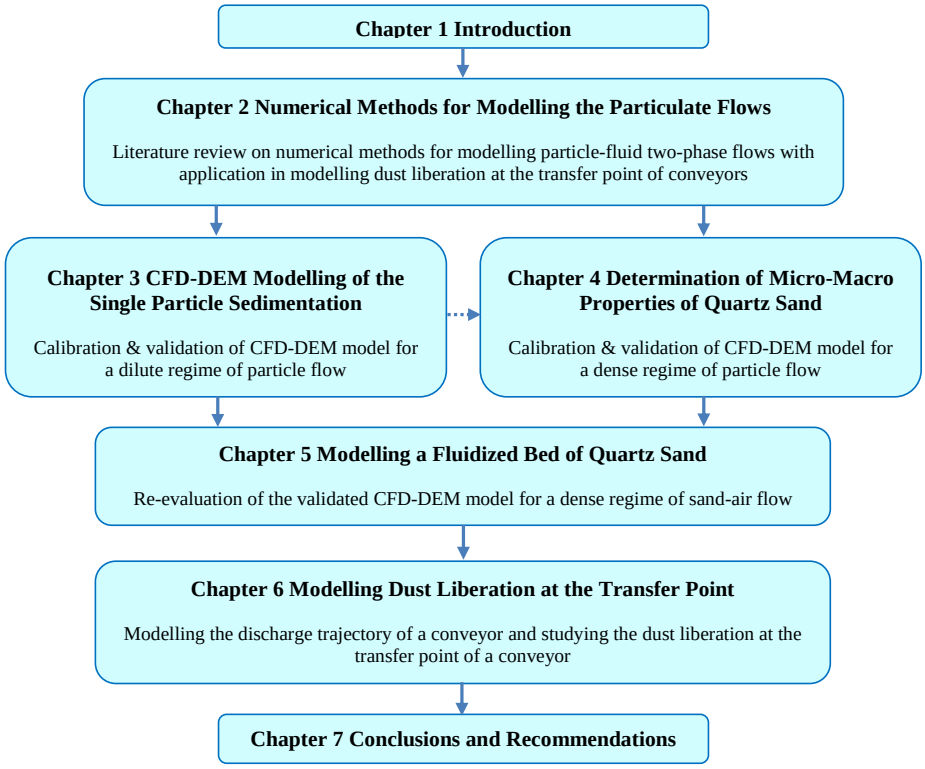

Figure 1.3: Road map for this thesis.

Bibliography

[1] H. S. Chaube and V. S. Pundhir, *Crop Diseases and Their Management*. PHI Learning, 2005.

[2] C. Gualtieri and D. T. Mihailovic, *Fluid Mechanics of Environmental Interfaces, Second Edition*, ser. EBL-Schweitzer. CRC Press, 2012.

[3] C. R. Woodcock and J. S. Mason, *Bulk Solids Handling: An Introduction to the Practice and Technology*. Springer Netherlands, 1988.

[4] V. Mody and R. Jakhete, *Dust Control Handbook*, ser. Pollution technology review. Noyes Data Corporation, 1988.

[5] W. E. Gibbs, *The dust hazard in industry*, ser. Chemical engineering. Benn, 1925.

[6] J. M. Stellman and I. L. Office, *Encyclopaedia of Occupational Health and Safety: Guides, indexes, directory*, ser. Encyclopaedia of Occupational Health and Safety. International Labour Office, 1998.

[7] S. M. Derakhshani, D. L. Schott, and G. Lodewijks, "Modeling Dust Liberation at the Belt Conveyor Transfer Point With CFD and DEM," in *11th International Congress on Bulk Materials Storage, Handling and Transportation*, no. July, Newcastle, Australia, 2013.

[8] P. Witt, K. Carey, and T. Nguyen, "Prediction of dust loss from conveyors using computational fluid dynamics modelling," *Applied Mathematical Modelling*, vol. 26, no. 2, pp. 297–309, feb 2002.

[9] R. T. Swinderman, L. J. Goldbeck, and A. D. Marti, *Foundations 3: The Practical Resource for Total Dust and Material Control*. Martin Engineering, 2002.

[10] M. A. Alspaugh, *Bulk Material Handling by Conveyor Belt 7*. Society for Mining, Metallurgy, and Exploration, 2008.

[11] J. G. Calvert, "Glossary of atmospheric chemistry terms," *Pure and Applied Chemistry*, vol. 62, no. 11, jan 1990.

[12] R. C. Weast, *Handbook of Chemistry and Physics*, 53rd ed. Chemical Rubber Pub., 1972.

[13] S. Rabha, M. Schubert, and U. Hampel, "Intrinsic flow behavior in a slurry bubble column: A study on the effect of particle size," *Chemical Engineering Science*, vol. 93, pp. 401–411, apr 2013.

[14] R. Jakhete, V. Mody, U. S. B. of Mines, M. M. Corporation, and M. Associates, *Dust Control Handbook for Minerals Processing: A Mining Research Contract Report*, ser. Contract (United States. Bureau of Mines). Bureau of Mines, U.S. Department of Interior, 1987.

[15] D. Hastie and P. Wypych, "Experimental validation of particle flow through conveyor transfer hoods via continuum and discrete element methods," *Mechanics of Materials*, vol. 42, no. 4, pp. 383–394, apr 2010.

[16] M. Combarros Garcia, H. Feise, S. Strege, and A. Kwade, "Segregation in heaps and silos: Comparison between experiment, simulation and continuum model," *Powder Technology*, oct 2015.

[17] C. Lin, Y. Yen, and J. Miller, "Plant-site evaluations of the OPSA system for on-line particle size measurement from moving belt conveyors," *Minerals Engineering*, vol. 13, no. 8-9, pp. 897–909, aug 2000.

[18] J. M. N. T. Gray, J. Goddard, P. Giovine, and J. T. Jenkins, "Particle size segregation in granular avalanches: A brief review of recent progress," in *IUTAM-ISIMM Symposium on Mathematical Modeling and Physical Instances of Granular Flows*, vol. 1227, no. 1. AIP Publishing, may 2010, pp. 343–362.

[19] Z. Liu, P. Cooper, and P. W. Wypych, "Experimental Investigation of Air Entrainment in Free-Falling Particle Plumes," *Particulate Science and Technology*, vol. 25, no. 4, pp. 357–373, aug 2007.

[20] X. Chen and C. Wheeler, "Computational Fluid Dynamics (CFD) modelling of transfer chutes: Assessment of viscosity, drag and turbulence models," *International Journal of Multiphase Flow*, vol. 69, pp. 42–53, mar 2015.

[21] P. McIlvenna and R. Mossad, "Two dimensional transfer chute analysis using a continuum method," dec 2003.

[22] C. Wheeler and X. Chen, "Computational Fluid Dynamics (CFD) modelling of transfer chutes: a study of the influence of model parameters," *Chemical Engineering Science*, vol. 95, pp. 194–202, may 2013.

[23] A. Katterfeld, T. J. Donohue, and C. A. Wheeler, "Simulation based dust predication of transfer chutes," 2010.

Chapter

2

Numerical Methods for Modelling the Particulate Flows

The importance of studying the dust liberation phenomenon in bulk material handling systems was reviewed in Chapter 1. A number of advantages of numerical methods compared to experimental approaches were discussed and then the first main research question of this thesis was defined as: "What numerical method can be employed as a tool in studying the dust liberation in bulk material handling systems?".

In this chapter, the numerical approaches are reviewed in detail to answer the first research question through selecting a numerical method with the application in modelling the dust liberation from bulk material handling systems. The factors that influence the rate of dust liberation from bulk material handling systems like a belt conveyor are the physical properties of particles, the inter-particle interactions, and the particle-equipment collisions. These factors, as well as the computational cost of the numerical technique, are regarded as the most important criteria in the selection of numerical method in this study.

The advantages and disadvantages of the numerous numerical methods in modelling particle-fluid two-phase flows will be briefly reviewed in section 2.1 and the appropriate approach for modelling the dust liberation at the transfer point of a belt conveyor will be selected. The theoretical background of the DEM method will be presented in section 2.2 and the sub-models and important parameters of the CFD-DEM coupling method will be introduced in section 2.3.

2.1 Modelling the particle-fluid two-phase flow

Leonhard Euler (1707-1783) proposed the Euler equations, which describe conservation of mass, and conservation of momentum for an inviscid fluid. Claude-Louis Navier (1785-1836) and George Gabriel Stokes (1819-1903) introduced viscous transport into the Euler equations, which resulted in the Navier-Stokes equations [1]. Recently, high speed computers have been used to solve approximations of the Navier-Stokes and continuity equations using a variety of numerical techniques like Finite Difference Method (FDM), Finite Volume Method (FVM), and Finite Element Method (FEM). This area of study is called CFD which is based on the Navier-Stokes equations [2, 3].

Two main approaches for modelling the interaction between particles and fluid phases [4] are the Eulerian-Eulerian and Eulerian-Lagrangian approaches. In both approaches, the fluid phase is modelled according to the continuum theories through solving the Navier-Stokes equations. However, in the first, the particle phase is considered as artificial continuum media while in the latter, the position of particle phase is tracked individually during the time.

1. Eulerian-Eulerian approach

The behaviour of material, particle and fluid phases, is modelled as a continuous mass rather than discrete particles in the Eulerian-Eulerian approach. The modified Navier-Stokes equations are used in this approach to model dispersed and continuous phases as separate inter-penetrating and interacting fluids. The momentum exchange between the phases are simulated by source terms in the governing equations of each phase [5].

2. Eulerian-Lagrangian approach

In the Eulerian-Lagrangian approach, the fluid is considered as a continuous medium and particles are assumed as points in the fluid. In this approach, the Navier-Stokes equations are modified to account the effect of fluid-particle interaction and Newton's second law is applied to track continuously the motion of a large amount of particles in a Lagrangian frame [5].

The particles in this approach can be formulated in two ways: point particle approximation (one-way coupling) and real particle size consideration (two-way or four-way coupling). In the one-way coupling, the particles are considered as points which are distributed in the continuum media. Therefore, the Navier-Stokes equations are solved for a continuous medium without any modification and particles are carried by the fluid flow. In this method, the dispersed phase does not have any influence on the continuous phase and the momentum is only transferred from the fluid phase to the particle phase. In the second case, the real size of a particle is considered in the modelling which leads to the momentum exchange between the dispersed and continuous phases, the so-called two-way coupling. The interaction between particles along with the momentum exchange between the continuum and particle phases is implemented in the four-way coupling.

2.1.1 Review of numerical methods for modelling the particulate flows

The numerical approaches that are widely used in modelling the particle-fluid two-phase flows are reviewed in this part.

Two-Fluid Model

The Two-Fluid Model (TFM) is one of Eulerian-Eulerian approaches [6] that is conducted in the numerical simulations such as modelling the dust liberation at the transfer point of conveyors [7, 8]. In this method, the size of computational cell is much larger than the size of particles of the dispersed flow which greatly reduces the computational time. The drawback of TFM is that some properties of the particle phase such as the coefficient of restitution and coefficients of sliding and rolling friction between particles are not implemented; in the other words, the interaction between particles and particles-equipment can not be modelled exactly with TFM.

Immersed Boundary Method

The Immersed Boundary Method (IBM) was originally developed by Peskin in 1972 [9], so that the fluid and bodies are represented by the Eulerian and Lagrangian coordinates, respectively. In this method, the CFD cells around the particles are dynamically refined in which the CFD cells are much smaller than the particle size and the fluid field is fully resolved around each particle. Implementation of the fine grids will lead to the detailed information about the fluid flow around a particle. On the other hand, this makes IBM very expensive from the viewpoint of computational time and this issue limits the application of IBM to a limited number of particles.

Direct Numerical Simulation

The Direct Numerical Simulation (DNS) [10] is a special kind of CFD in which the Navier-Stokes equations are fully resolved without any turbulence model. In the DNS, all the spatial scales of the turbulence are fully resolved in the computational mesh, from the smallest dissipative scales, up to the integral scale, associated with the motions containing most of the kinetic energy [11]. The computational time for exact solutions of a low Reynolds number takes a couple of weeks on today's largest supercomputers which is the main drawback of DNS [12].

Lattice Boltzmann Method

The Lattice Boltzmann Method (LBM) is a numerical technique that has been developed for modelling physical phenomena of Newtonian fluid flows based on the discrete Boltzmann equation which is coupled to the collision models such as Bhatnagar-Gross-Krook (BGK) [13]. In the other words, the LBM is based on the microscopic models and mesoscopic kinetic equations while the FDM, FEM, and FVM methods discretize the macroscopic continuum equations [14].

The ability to easily represent complex physical phenomena, ranging from multiphase flows to chemical interactions between the fluid and the surrounding environment is one of the advantages of this technique. In comparison, with the traditional methods, the LBM technique has a number of disadvantages. For instance, the combination of high and low resolution areas or application of curved grids is difficult.

Also, a few commercial or open sources softwares have been developed based on the Lattice Boltzmann theory.

Smoothed-Particle Hydrodynamics

The Smoothed-Particle Hydrodynamics (SPH) [15, 16] is a mesh free particle method that is developed based on the interpolation method to approximate values and derivatives of continuous field quantities by a set of discrete elements. The SPH has some advantages compared to the traditional CFD methods and also it has some intrinsic limitations. It can easily deal with complicated geometric settings and introducing more than one material is often trivial for SPH while the traditional methods have difficulty with the interface problems [17].

Some disadvantages are, for instance, implementation of a boundary condition is very hard and it is computationally slower than the other traditional methods because the time step is adjusted according to the sound speed within the fluid [18].

Discrete Element Method

The Discrete Element Method (DEM) is a numerical technique for computing the motion and collisions of particles that was developed by Cundall and Strack [19] in order to solve the problems of the rock mechanics. Afterwards, researchers focused on other applications of DEM such as modelling the granular materiel or powder mechanics [20, 21].

The DEM is essentially a Lagrangian approach which is capable to accurately model the inter-particle collision and the particle-equipment interactions. The DEM is relatively computationally intensive, which limits either the length of a simulation or the number of particles. On the other hand, parallel processing capability is one of the advantages of DEM codes to scale up the number of particles or duration of the simulation [22]. The DEM can be used in the design and optimization of processes and equipment to avoid the expensive prototyping and predictable errors.

Coupled Computational Frameworks

A number of researches have been focused on coupling between the DEM method with other numerical methods to increase the accuracy of simulation results by having more detailed information about the particle phase in the whole domain of fluid phase. Coupling DEM with CFD methods will lead to have the four-way coupling technique with the capability of modelling the inter-particle collisions as well as the interaction between particles and equipment.

The IBM and DNS techniques can be coupled with DEM to include the inter-particle collisions in the modelling [23, 24]. However, these kinds of coupling requires substantially more grid resolution and consequently more computational effort. Hence, the IBM-DEM and DNS-DEM coupling techniques can be applied in the small systems to study the physical process in detail and consequently improving the accuracy of the large scale models.

There is a number of obvious advantages of LBM-DEM and SPH-DEM approaches [25, 26]. The traditional CFD solvers have enormous difficulties to tackle the complexity of the geometry while in LBM-DEM and SPH-DEM techniques the particle movement and domain deformation are inherently included [27] and they have an

extreme flexibility to treat with complex boundary conditions. Parallel processing is the other advantage of these approaches because the collisions are calculated locally.

The first difference between the CFD-DEM method with SPH-DEM and LBM-DEM methods is about the way that the force is calculated in the governing equations of these methods. In the CFD-DEM method, the aggregate coupling force is calculated first and then it is distributed to particles while in the SPH-DEM and LBM-DEM models the coupling force is calculated on for individual particles and then the total force is applied to the SPH and LBM particles. Due to the high cost of the drag force calculation, the cost of SPH-DEM and LBM-DEM is much higher than CFD-DEM [28]. Also, the void fraction field is utilized in the CFD-DEM method to capture the effect of the particle phase onto the fluid phase [29] which is the latter difference between these methods.

2.1.2 Selecting the suitable method for modelling dust liberation

Numerical techniques provide the opportunity to obtain detailed information about the fluid and particle interaction at lower cost than the expensive experiments. A number of numerical models with the ability to be used in the modelling particle-fluid two-phase flows were introduced.

The collision between equipment, material and air molecules, and the effect of surrounding air on the discharge trajectory was addressed in Chapter 1 as some reasons for dust liberation at the transfer points. It is seen that the dust liberation phenomenon is inherently a particle-fluid two-phase flow, therefore, the following criteria should be considered in the selection of numerical method which is suitable for modelling dust liberation at the transfer point of a belt conveyor.

1. The microscopic properties of the particle phase

The coefficient of restitution and the coefficients of rolling and sliding friction are three microscopic properties of material. These microscopic properties are unique for different materials and they have a significant effect on the macroscopic properties of material such as the Angle of Repose (AoR), the erosion rate, and the rate of dust liberation [30–32]. TFM is inherently an Eulerian-Eulerian approach and therefore the microscopic properties of particles are not modelled by this method. The CFD, IBM, DNS, and LBM techniques have the same disadvantage that can be fixed through coupling with a Lagrangian technique such as DEM to include the material properties in the simulation.

2. Inter-particles and particle-equipment collisions

The collision between particles and equipment is one of the causes of dust liberation in the bulk material handling. Some particles will leave the discharge trajectory due to the inter-particle and particle-equipment collisions and will be carried with the airflow as the dust into the surrounding air. Therefore, the selected numerical technique should be able to model the collision between particles and equipment.

Hence, the numerical techniques that utilize the Eulerian technique to simulate

the particle phase are not able to accurately model the collision between particles and equipment. For instance, the TFM, CFD, IBM, DNS, and LBM methods individually are not able to model the inter-particle collision and they need to be coupled with a Lagrangian technique such as DEM to obtain more information about the particle and equipment collisions.

3. The computational effort

It was explained in part 2.1.2 that more detailed information about the fluid flow can be extracted by utilizing the IBM, DNS, LBM, and SPH techniques. On the other hand, it is necessary to link these techniques to a Lagrangian technique to obtain more information about the collisions between particles and equipment. The IBM, DNS, LBM, and SPH are generally expensive techniques and coupling with a Lagrangian technique extremely increases the computational effort. These techniques get illogical, especially, for simulations with numerous particles. The other option is coupling the CFD with DEM to decrease the computational effort on the fluid side while the detailed information about the particle level can be obtained by DEM model.

The criteria that need to be considered in the selection of the suitable technique for modelling the dust liberation at the transfer point of a belt conveyor are summarized in Table 2.1.

Table 2.1: Summary of numerical techniques for modelling particle-fluid flows.

Numerical method	Microscopic properties	Particles and equipment collisions	Fluid-particle interactions
CFD	No	No	No
DEM	Yes	Yes	No
TFM	No	Yes	Yes
CFD-DEM	Yes	Yes	Yes
DNS, IBM, SPH, LBM	No	No	Yes
(DNS, IBM, SPH, LBM)-DEM	Yes	Yes	Yes

The collision between particles and equipment and the pressure difference around the trajectory of material are two reasons that fine particles are separated from the discharge trajectory of material. It should be noted that the detailed information about the fluid flow around each particle is not necessary and determining the pressure distribution in the domain is sufficient [33–35]. As seen in Table 2.1, the CFD-DEM coupling technique is able to model the collision between particles and equipment, modelling the microscopic properties of the materials as well as determining the pressure distribution in the domain with the computational effort far less than the other techniques. Consequently, the CFD-DEM coupling technique will be used in this study to model dust liberation at the transfer point of a belt conveyor.

2.2 Discrete Element Model (DEM)

In this study, LIGGGHTS-PUBLIC [36] as an open source and non-commercial software, is used to determine the microscopic properties of quartz sand and to simulate the inter-particle collision and the interaction between the particles and equipment. The capability of coupling with OpenFOAM [37] as an open source and non-commercial CFD software package is the other advantage of this software. In this section, the theoretical framework of the DEM will be described in detail.

2.2.1 Contact model

The movement of discrete particles is governed by Newton's second law of motion. The net force acting on an individual particle i comprises a gravitational force $m_i \boldsymbol{g}$ and particle-particle contact force $\boldsymbol{f}_{pp,i}$. The translational and rotational motions of particle i with mass m_i and the moment of inertia I_i are governed by the following equations:

$$m_i \frac{d\boldsymbol{u}_i}{dt} = \boldsymbol{f}_{pp,i} + m_i \boldsymbol{g} \tag{2.1}$$

$$I_i \frac{d\boldsymbol{\omega}_i}{dt} = \boldsymbol{M}_i = \sum_{j=1}^{k_c} (\boldsymbol{M}_{t,ij} + \boldsymbol{M}_{r,ij}) \tag{2.2}$$

In which, $\boldsymbol{u}_i$ and $\boldsymbol{\omega}_i$ are the translational and angular velocities of particles and k_c specifies the number of particles in collision with particle i. $\boldsymbol{M}_i$ is the momentum arising from the tangential components of the contact forces. The momentum acting on particle i by particle j is composed of two components: $\boldsymbol{M}_{t,ij}$ that is generated by the tangential force, and $\boldsymbol{M}_{r,ij}$, which is because of the rolling friction momentum [38].

Two linear and non-linear elastic contact models of the LIGGGHTS software are the Hookean and Hertz-Mindlin contact models, respectively. The Hertz-Mindlin contact model that is a well-known contact model for modelling the non-cohesive interactions [39] is shown in Figure 2.1. In this model, the first spring-dashpot represents the normal contact between particles and/or geometry, the coefficient of Coulomb friction μ_c represents shear interactions and the second spring-dashpot undertakes the tangential interaction between particles.

When the overlap contact distance δ_{ij} between two particles of radii R_i and R_j is less than $R_{ij} = R_i + R_j$, the following formula for the frictional force between two granular particles is used:

$$\boldsymbol{f}_{pp,i} = (k_n \delta_{n,ij} - \gamma_n u_{n,ij}) + (k_t \delta_{t,ij} - \gamma_t u_{t,ij}) \tag{2.3}$$

Where k and γ are the stiffness and visco-elastic damping constant of spherical particles, respectively. Also, the relative velocity between two particles is defined

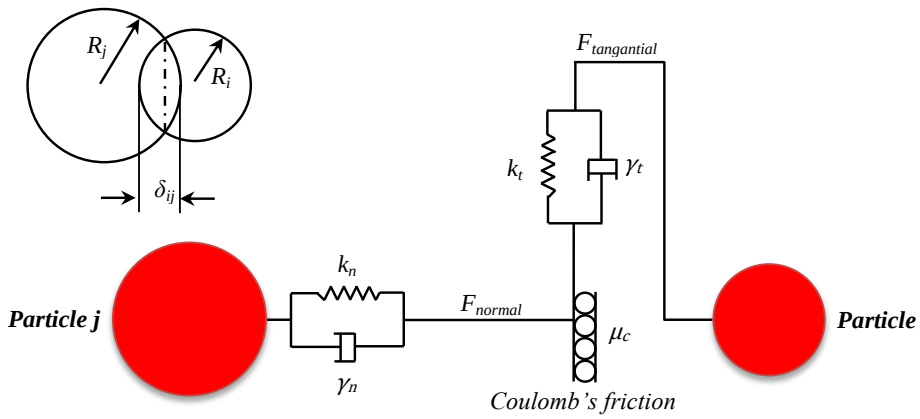

Figure 2.1: Schematic picture of simplified Hertz-Mindlin contact model between two particles.

by u_{ij}. The tangential force between two particles grows according to a tangential spring and dashpot model until $F_t/F_n = \mu_c$ and then is held at $F_t = \mu_c F_n$ until the particles loose contact. Equation 2.4 shows the formulation of stiffness constants in the normal and tangential directions.

$$k_t = 8G_{eff}\sqrt{R_{eff}\delta_n} \tag{2.4}$$
$$k_n = 4/3E_{eff}\sqrt{R_{eff}\delta_n} \tag{2.5}$$

Where E_{eff}, G_{eff}, and R_{eff} are the effective Young's modulus, the effective shear modulus, and the effective radius, respectively, which are expressed by the following equations.

$$1/E_{eff} = (1-\nu_1^2)/E_1 + (1-\nu_2^2)/E_2 \tag{2.6}$$
$$1/G_{eff} = 2(2-\nu_1)(1+\nu_1)/E_1 + 2(2-\nu_2)(1+\nu_2)/E_2 \tag{2.7}$$
$$1/R_{eff} = 1/R_1 + 1/R_2 \tag{2.8}$$

The formulation of the visco-elastic damping constant in the normal and tangential directions is shown in Equations 2.9 and 2.10.

$$\gamma_t = -2\beta_d\sqrt{5/6}\sqrt{S_t m_{eff}} \tag{2.9}$$
$$\gamma_n = -2\beta_d\sqrt{5/6}\sqrt{S_n m_{eff}} \tag{2.10}$$

Where β_d is the dimensionless damping coefficient and the effective mass m_{eff} is

expressed by $1/m_{eff} = 1/m_1 + 1/m_2$. The S_n, S_t, and β_d are formulated as below:

$$S_t = 8G_{eff}\sqrt{R_{eff}\delta_n} \tag{2.11}$$

$$S_n = 2E_{eff}\sqrt{R_{eff}\delta_n} \tag{2.12}$$

$$\beta_d = ln\,(e)/\sqrt{ln^2\,(e) + \pi^2} \tag{2.13}$$

2.2.2 Governing equations of rolling resistance

The granular material with irregular and complicated shapes are widely used in many industrial processes and fields [40, 41]. One of the expensive parts of DEM modelling is considering the particle shape in the simulation. Therefore, rolling friction is incorporated in DEM as an alternative solution of the particle shape consideration [42–45].

Ai et al. [46] assessed four different types of rolling resistance models. It was indicated that model C produced satisfactory predictions of the stockpile formation while models A and B both had a deficiency in modelling a stable pile. Model C is also known as elastic-plastic spring-dashpot model that applies a momentum consisting of two components: a spring momentum $\boldsymbol{M}_r^k$ and a viscous damping momentum $\boldsymbol{M}_r^d$ on the particle to account for the rolling friction. The resistant momentum between two particle i and j can be represented as:

$$\boldsymbol{M}_r = \boldsymbol{M}_r^k + \boldsymbol{M}_r^d \tag{2.14}$$

Figure 2.2 shows the mechanism of rolling resistance which generates a resistant moment $\boldsymbol{M}_r$.

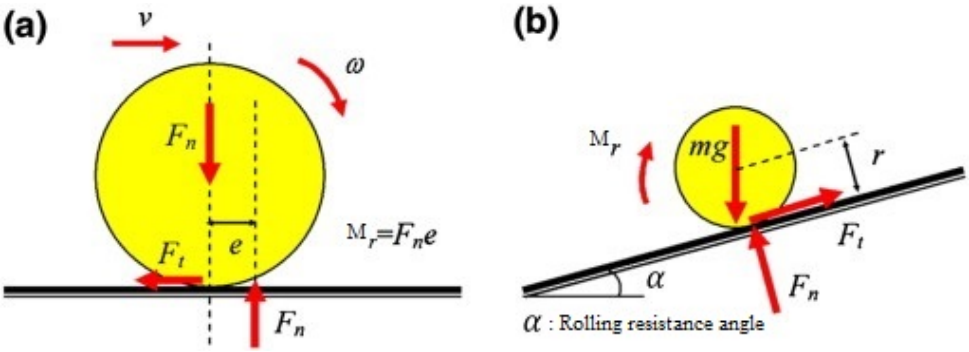

Figure 2.2: Rolling resistance and rolling resistance angle a) mechanism of rolling resistance; b) rolling resistance angle [46].

According to Wensrich [30], in the modified version of model C, the rolling damping is not being considered in the new formulation of rolling stiffness. Equation 2.15 is represented the rolling stiffness of the modified model C:

$$k_r = k_t R_{eff}^2 \tag{2.15}$$

Since the rolling oscillations are partly small in comparison with the typical time constants in the DEM, the motion effect of shear damping at the contact is negligible. So mobilization of the shear damping occurs at the higher levels of rolling stiffness and it is not necessary to use an additional parameter (rolling damping) in the DEM simulation [30, 46, 47]. Thus, the modified version of model C will be used in this study. The modified resistant momentum between two particles i and j can be represented:

$$\boldsymbol{M}_r = \boldsymbol{M}_r^k = -k_r \triangle \theta_r \tag{2.16}$$

2.2.3 DEM time step

One of the important subjects in DEM simulation is determination of the time step. A sufficient short time step is required to ensure the numerical stability and accuracy of DEM simulation. On the other hand, a DEM simulation is limited by computational effort which limits utilization of the small DEM time-steps.

On the other hand, it is essential that the ratio of skin size that is the extra distance beyond force cut off to the distance that particles can travel relative to each other at one time-step be greater than 1, otherwise, some interactions may be missed or overlap energy may be generated artificially [48]. To ensure about this issue, Rayleigh and Hertz time are implemented in DEM code. The formulation of Rayleigh time step t_r and Hertz time step t_h are given in Equations 2.17 and 2.18 [48]. In order to be sure about the accuracy of DEM simulations, it is better to use 10 percent of Rayleigh time as the DEM time step [49].

$$t_r = \frac{\pi D_p}{2} \sqrt{(\rho_p / G)} / (0.163\nu + 0.8766) \tag{2.17}$$

$$t_h = 2.87 \times \left(m^2 / \left(\frac{D_p}{2} \times E^2 \times u_{max} \right) \right)^{0.2} \tag{2.18}$$

Where ν and G are Poisson ratio and shear modulus between particles, respectively.

2.3 CFD-DEM coupling method

In the CFD-DEM model, the motion of particles is calculated by DEM while CFD is utilized to solve the local averaged Navier-Stokes equations for the fluid phase. The CFDEM open source software [48] together with the other open source software packages, OpenFOAM and LIGGGHTS, has been used to implement the coupling

between CFD and DEM. Figure 2.3 illustrates how information exchanges between CFD and DEM models.

In this section, the theoretical framework of the three sets of Navier-Stokes equation, drag force models, and voidage models that are widely used in the field of particle-fluid two-phase flows are presented in detail.

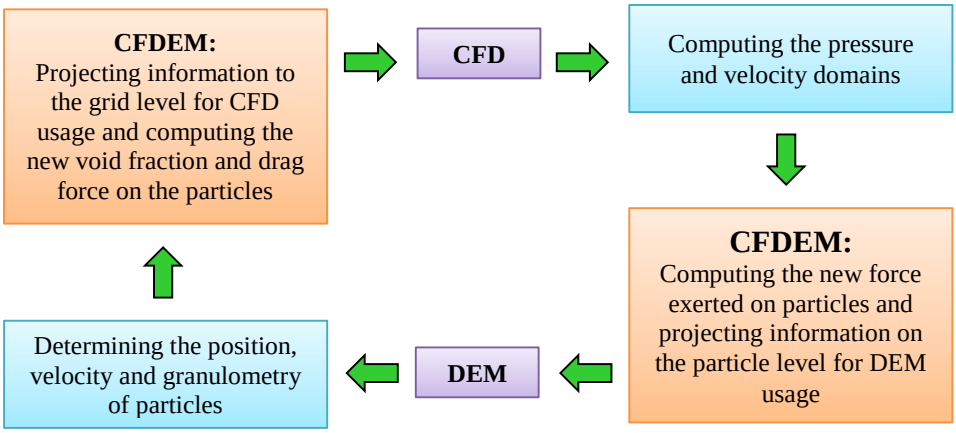

Figure 2.3: Information exchange between CFD and DEM models.

The coupling interval (CI) determines the time passing between two CFD and DEM data exchanges which is defined as follows:

$$\Delta t_{CFD} = CI \times \Delta t_{DEM} \tag{2.19}$$

2.3.1 The governing equations of the particle and fluid phases

In the CFD-DEM coupling method, the fluid phase is treated as a continuum media and the fluid flow is calculated by Navier-Stokes equations based on the law of conservation of mass and momentum. The particle phase is considered as a discrete phase and the motion of particles are determined by Newton's second law of motion. The governing equation for the transnational motion of particle i with mass of m_i is written as follows [29]:

$$m_i \frac{d\boldsymbol{u}_i}{dt} = \boldsymbol{f}_{pf,i} + \boldsymbol{f}_{pp,i} + m_i \boldsymbol{g} \tag{2.20}$$

Where $\boldsymbol{u}_i$ is the translational velocity of a particle. The fluid-particle interaction force $\boldsymbol{f}_{pf,i}$, the gravitational force $m_i \boldsymbol{g}$, and the inter-particle collision force $\boldsymbol{f}_{pp,i}$ are the involving forces in Equation 2.20. The rotational motion of particle, $\boldsymbol{M}_i$, which arises from the tangential components of the contact forces was already defined by Equation 2.2.

The fluid-particle interaction force is the sum of all types of particle-fluid interaction forces including the drag force $\boldsymbol{f}_{d,i}$, pressure gradient force $\boldsymbol{f}_{\bigtriangledown p,i}$, viscous force $\boldsymbol{f}_{\bigtriangledown.\tau,i}$, virtual mass force $\boldsymbol{f}_{vm,i}$, Basset force $\boldsymbol{f}_B$, and lift forces such as Saffman $\boldsymbol{f}_{Saff}$ and Magnus force $\boldsymbol{f}_{Mag}$ [50] that act contrary to the gravitational force $m_i\boldsymbol{g}$. The lift forces, including Saffman and Magnus lift forces, are due to the rotation of particle and for the spherical particle without rotational motion, the effect of lift forces is negligible [51]. Therefore, the fluid-particle interaction force on an individual particle i is as follows:

$$\boldsymbol{f}_{pf,i} = \boldsymbol{f}_{d,i} + \boldsymbol{f}_{\bigtriangledown p,i} + \boldsymbol{f}_{\bigtriangledown.\tau,i} + \boldsymbol{f}_i^{''} \tag{2.21}$$

$$\boldsymbol{f}_i^{''} = \boldsymbol{f}_{vm,i} + \boldsymbol{f}_{B,i} + \boldsymbol{f}_{Saff,i} + \boldsymbol{f}_{Mag,i} \tag{2.22}$$

Depending on the treatment of the pressure drop in the Navier-Stokes equations, three sets of formulation have been proposed to be applied in the CFD-DEM coupling model, referred to as set I, II, and III [29]. Sets II and III are known as model A and B, respectively, and set I is named as Bfull model because its similarity to model B. The conservation of mass for both phases in all three sets is formulated as follows:

$$\frac{\partial(\varepsilon_f\rho_f)}{\partial t} + \bigtriangledown.(\varepsilon_f\rho_f\boldsymbol{u}_f) = 0 \tag{2.23}$$

$$\frac{\partial(\varepsilon_p\rho_p)}{\partial t} + \bigtriangledown.(\varepsilon_p\rho_p\boldsymbol{u}_p) = 0 \tag{2.24}$$

Where ε_f and ε_p are the fluid and particle void fractions in a numerical cell. The relation between the void fractions is as follows:

$$\varepsilon_f + \varepsilon_p = 1 \tag{2.25}$$

The momentum conservation equations for sets I, II, and III are written as follows:

$$I: \begin{cases} \dfrac{\partial(\rho_f\varepsilon_f\mathbf{u}_f)}{\partial t} + \bigtriangledown.(\rho_f\varepsilon_f\mathbf{u}_f\mathbf{u}_f) = -\bigtriangledown p - \mathbf{F}_{pf}^{setI} + \bigtriangledown.\tau + \rho_f\varepsilon_f\mathbf{g} & \text{(2.26a)} \\ \boldsymbol{F}_{pf}^{I} = \dfrac{1}{\Delta V}\sum_{i=1}^{n}(\boldsymbol{f}_{d,i} + \boldsymbol{f}_{\bigtriangledown p,i} + \boldsymbol{f}_{\bigtriangledown.\tau,i} + \boldsymbol{f}_i^{''}) & \text{(2.26b)} \\ \boldsymbol{f}_{pf,i} = \boldsymbol{f}_{d,i} + \boldsymbol{f}_{\bigtriangledown p,i} + \boldsymbol{f}_{\bigtriangledown.\tau,i} + \boldsymbol{f}_i^{''} & \text{(2.26c)} \end{cases}$$

$$II: \begin{cases} \dfrac{\partial(\rho_f\varepsilon_f\mathbf{u}_f)}{\partial t} + \bigtriangledown.(\rho_f\varepsilon_f\mathbf{u}_f\mathbf{u}_f) = -\varepsilon_f\bigtriangledown p - \mathbf{F}_{pf}^{setII} + \varepsilon_f\bigtriangledown.\tau + \rho_f\varepsilon_f\mathbf{g} & \text{(2.27a)} \\ \boldsymbol{F}_{pf}^{II} = \dfrac{1}{\Delta V}\sum_{i=1}^{n}(\boldsymbol{f}_{d,i} + \boldsymbol{f}_i^{''}) - \dfrac{1}{\Delta V}\sum_{i=1}^{n}(\rho_f V_{p,i}\mathbf{g}) & \text{(2.27b)} \\ \boldsymbol{f}_{pf,i} = \boldsymbol{f}_{d,i} + \boldsymbol{f}_{\bigtriangledown p,i} + \boldsymbol{f}_{\bigtriangledown.\tau,i} + \boldsymbol{f}_i^{''} & \text{(2.27c)} \end{cases}$$

$$III: \begin{cases} \dfrac{\partial(\rho_f \varepsilon_f \mathbf{u}_f)}{\partial t} + \bigtriangledown.(\rho_f \varepsilon_f \mathbf{u}_f \mathbf{u}_f) = -\bigtriangledown p - \mathbf{F}_{pf}^{setIII} + \bigtriangledown.\tau + \rho_f \varepsilon_f \mathbf{g} & \text{(2.28a)} \\ \boldsymbol{F}_{pf}^{III} = \dfrac{1}{\varepsilon_f \Delta V} \sum_{i=1}^{n} (\boldsymbol{f}_{d,i} + \boldsymbol{f}_i^{''}) - \dfrac{1}{\Delta V} \sum_{i=1}^{n} (\rho_f V_{p,i} \mathbf{g}) & \text{(2.28b)} \\ \boldsymbol{f}_{pf,i} = \dfrac{(\boldsymbol{f}_{d,i} + \boldsymbol{f}_i^{''})}{\varepsilon_f} - \rho_f V_{p,i} \mathbf{g} & \text{(2.28c)} \end{cases}$$

Where V and $V_{p,i}$ are the total volume of a numerical cell and the volume of a particle, respectively. The investigations of Zhou et al. [29] shows that all three models are usable for studies such as fluidization and pneumatic conveying. However, set III is a simplified version of set I and it is usable when the particle phase is steady and uniform [52]. Considering the objective of this research, set I will be employed in the CFD-DEM simulations of this study.

2.3.2 Drag force models

The formulation of the drag force $\boldsymbol{f}_d$ is as follows:

$$\boldsymbol{f}_d = ksl(\boldsymbol{u}_f - \boldsymbol{u}_p) \tag{2.29}$$

Where the ksl is the momentum exchange coefficient that represents the amount of drag force exchange between the CFD and DEM models. Many correlations have been proposed to calculate the drag force between the particle and fluid phases, particularly, the equations of Ergun [53], Di Felice [54], Gidaspow [55], and Koch Hill [56]. In this study, these well-known drag force models are evaluated by different benchmarking tests to select the proper drag model for simulating the dust liberation phenomenon.

Ergun drag model

Flow through a packed bed can be regarded as fluid flow through number of submerged objects such as spherical particles with diameter of D_p. To calculate the pressure drop in a packed bed in a specified flow rate, the following equation is proposed by Ergun [53] for $\varepsilon_f \leq 0.8$:

$$ksl = \frac{\Delta p}{H} = 150 \frac{\mu_f}{{D_p}^2} \frac{(1-\varepsilon_f)^2}{\varepsilon_f} + 1.75 \frac{\rho_f}{D_p} (1-\varepsilon_f) |u_f - u_p| \qquad \varepsilon_f \leq 0.8 \tag{2.30}$$

Where Δp is the pressure drop, H is the height of the bed, D_p is the particle diameter, ε_f is the porosity of the bed, μ_f is the fluid viscosity, ($u_{fp} = \boldsymbol{u}_f - \boldsymbol{u}_p$) is the superficial velocity (the volumetric fluid flow rate divided by the cross-sectional area of the bed), and ρ_f is the fluid density. As seen in the Ergun equation, the pressure drop is a function of the packing size, length of bed, volume fraction of fluid,

density and viscosity of fluid phase, superficial velocity and particle diameter.

Wen-Yu drag model

The Wen-Yu drag model [57] uses a correlation from the experimental data of Richardson and Zaki [58]. This model is valid when the internal forces are negligible which means that the viscous forces dominate the flow behaviour.

$$ksl = \frac{3}{4} C_d \frac{\varepsilon_f(1-\varepsilon_f)}{D_p} \rho_f |u_f - u_p| {\varepsilon_f}^{-2.65} \qquad \varepsilon_f > 0.8 \tag{2.31}$$

Where the drag coefficient C_d is described by:

$$C_d = \begin{cases} \dfrac{24}{Re_p}[1 + 0.15(Re_p)^{0.687}] & Re_p \leq 1000 \quad (2.32a) \\ 0.44 & Re_p > 1000 \quad (2.32b) \end{cases}$$

The particle Reynolds number is given by:

$$Re_p = \frac{\varepsilon_f \rho_f |u_f - u_p| D_p}{\mu_f} \tag{2.33}$$

Gidaspow drag model

The Gidaspow drag model [55] is a combination of the Wen-Yu and Ergun equations. The combination of the two drag models 2.30 and 2.31 in the Gidaspow drag model is defined as:

$$ksl = \begin{cases} Wen - Yu\ model & \varepsilon_f > 0.8 \quad (2.34a) \\ Ergun\ model & \varepsilon_f \leq 0.8 \quad (2.34b) \end{cases}$$

Di Felice drag model

Di Felice [29, 54] proposed an empirical expression for the momentum exchange coefficient ksl as follows:

$$ksl = \frac{\pi {D_p}^2}{8} \rho_f C_d |u_f - u_p| {\varepsilon_f}^{(2-\xi)} \tag{2.35}$$

Where C_d and ξ are given as below:

$$C_d = [0.63 + \frac{4.8}{\sqrt{Re_p}}]^2 \tag{2.36}$$

$$\xi = 3.7 - 0.65 exp[-\frac{(1.5 - logRe_p)^2}{2}] \tag{2.37}$$

Koch-Hill drag model

Koch and Hill [56] proposed a new drag model based on the Lattice-Boltzmann simulation results as follows:

$$ksl = \frac{18\mu_f {\varepsilon_f}^2 \varepsilon_p}{{D_p}^2}(F_0(\varepsilon_p) + \frac{1}{2}F_3(\varepsilon_p)Re_p) \tag{2.38}$$

Where:

$$F_0(\varepsilon_p) \begin{cases} \dfrac{1 + 3\sqrt{\frac{\varepsilon_p}{2}} + \frac{135}{64}\varepsilon_p ln(\varepsilon_p) + 16.14\varepsilon_p}{1 + 0.681\varepsilon_p - 8.48{\varepsilon_p}^2 + 8.16{\varepsilon_p}^3} & \varepsilon_p < 0.4 \quad (2.39a) \\ \dfrac{10\varepsilon_p}{{\varepsilon_f}^3} \qquad \varepsilon_p \geq 0.4 & (2.39b) \end{cases}$$

$$F_3(\varepsilon_p) = 0.0673 + 0.212\varepsilon_p + \frac{0.0232}{{\varepsilon_f}^5} \tag{2.40}$$

2.3.3 Voidage models

The voidage models of the CFDEM package that are used to determine the void fraction of CFD cells are centre, divided, and big particle models. The centre and divided models are valid for the cases that the particle size is less than the CFD grid [48]. The void fraction distribution between CFD cells are shown for all voidage models in Figure 2.4.

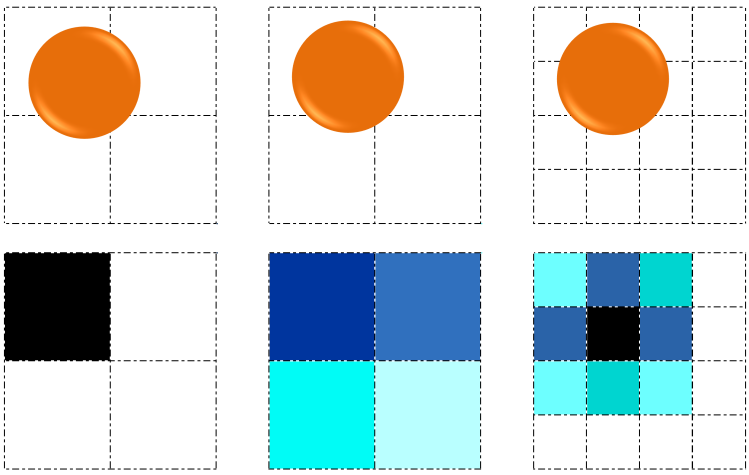

Figure 2.4: Schematic picture of particle volume distribution between CFD cells for centre, Divided, and big particle models.

In the centre model, the total volume of a particle is specified for a fluid cell in which the particle centre is located, whilst in the divided model the void fraction is calculated based on the distribution of particle volume between the CFD cells. The big particle model is usable for the cases where the size of particle is larger than the CFD grid and the void fraction is calculated in a similar way as the divided model.

If the centre or divided voidage models utilize in the CFD-DEM model, the fluid flow around a particle is not solved in detail and the CFD-DEM model is known as unresolved model. Whereas, some information about the fluid flow around a particle can be obtained through utilization of the big particle model and the CFD-DEM model is referred to resolved model.

2.4 Conclusions

The objective of this chapter was selecting a proper numerical approach for modelling the dust liberation in bulk material handling systems. It was concluded that the CFD-DEM coupling method is the proper technique for modelling the dust liberation at the transfer point of a belt conveyor as a bulk material handling system. The other results of this chapter are presented below.

1. It was indicated that it is neither possible nor necessary to fully resolve the flow and pressure field of the fluid phase around the particles in the discharge trajectory of a belt conveyor. Hence, the unresolved CFD model are utilized to simulate the fluid phase while more detailed information about the particle phase such as position and velocity of particles are determined with the DEM model.

2. A number of advantages of the CFD-DEM coupling method compared to the other numerical methods are the lower computational effort than the other coupled methods, the ability to determine the microscopic properties of the materials, modelling the inter-particles and particle-equipment collisions, improving the accuracy of airflow field simulation through the obtained information from the particle phase.

Bibliography

[1] J. S. Rao, *History of Rotating Machinery Dynamics*, ser. History of Mechanism and Machine Science. Springer Netherlands, 2011.

[2] C. Kleinstreuer, *Two-Phase Flow: Theory and Applications*. CRC Press, 2003.

[3] J. Li, W. Ge, W. Wang, N. Yang, X. Liu, L. Wang, X. He, X. Wang, J. Wang, and M. Kwauk, *From Multiscale Modeling to Meso-Science: A Chemical Engineering Perspective*. Springer Science & Business Media, 2013.

[4] L. S. Fan and C. Zhu, *Principles of Gas-Solid Flows*, ser. Cambridge Series in Chemical Engineering. Cambridge University Press, 2005.

[5] B. V. Balakin, A. C. Hoffmann, P. Kosinski, and L. D. Rhyne, "Eulerian-Eulerian CFD model for the sedimentation of spherical particles in suspension with high particle concentrations," *Engineering Applications of Computational Fluid Mechanics*, vol. 4, no. 1, pp. 116–126, 2010.

[6] T. B. Anderson and R. O. Y. Jackson, "A Fluid Mechanical Description of Fluidized Beds," *Industrial & Engineering Chemistry Fundamentals*, vol. 6, no. 4, pp. 527–539, 1967.

[7] P. Witt, K. Carey, and T. Nguyen, "Prediction of dust loss from conveyors using computational fluid dynamics modelling," *Applied Mathematical Modelling*, vol. 26, no. 2, pp. 297–309, feb 2002.

[8] X. Chen and C. Wheeler, "Computational Fluid Dynamics (CFD) modelling of transfer chutes: Assessment of viscosity, drag and turbulence models," *International Journal of Multiphase Flow*, vol. 69, pp. 42–53, mar 2015.

[9] C. Peskin, "Flow patterns around heart valves: a digital computer method for solving the equations of motion," 1972.

[10] B. S. A. Orszagt and S. Orszag, "Analytical theories of turbulence," *Journal of Fluid Mechanics*, vol. 41, no. 02, pp. 363–386, 1970.

[11] A. Issakhov, "Numerical Methods for Solving Turbulent Flows by Using Parallel Technologies," *Journal of Computer and Communications*, vol. 01, no. 01, pp. 1–5, 2013.

[12] S. Kurien and M. Taylor, "Direct Numerical Simulation of Turbulence: Data Generation and Statistical Analysis," *Los Alamos Science*, vol. 29, pp. 142–151, 2005.

[13] P. Lallemand and L.-S. Luo, "Theory of the lattice Boltzmann Method: Dispersion, Dissipation, Isotropy, Galilean Invariance, and Stability," 2000.

[14] Y. Y. Al-Jahmany, G. Brenner, and P. O. Brunn, "Comparative study of lattice-Boltzmann and finite volume methods for the simulation of laminar flow through a 4:1 planar contraction," *International Journal for Numerical Methods in Fluids*, vol. 46, no. 9, pp. 903–920, 2004.

[15] L. B. Lucy, "A numerical approach to the testing of the fission hypothesis," *The astronomical journal*, vol. 82, pp. 1013–1024, 1977.

[16] R. A. Gingold and J. Monaghan, "Smoothed particle hydrodynamics: theory and application to non-spherical stars," *Mon. Not. R. astr. Soc.*, no. 181, pp. 375–389, 1977.

[17] J. J. Monaghan, "Smoothed particle hydrodynamics," pp. 1703–1759, 2005.

[18] A. J. C. Crespo, "Application of the Smoothed Particle Hydrodynamics model SPHysics to free-surface hydrodynamics," Ph.D. dissertation, UNIVERSIDADE DE VIGO.

[19] P. Cundall and O. Strack, "Discrete numerical model for granular assemblies," *International Journal of Rock Mechanics and Mining Sciences & Geomechanics Abstracts*, vol. 16, no. 4, p. 77, aug 1979.

[20] Y. Guo and J. S. Curtis, "Discrete Element Method Simulations for Complex Granular Flows," *Annual Review of Fluid Mechanics*, vol. 47, no. 1, pp. 21–46, jan 2015.

[21] M. Marigo and E. H. Stitt, "Discrete Element Method (DEM) for Industrial Applications: Comments on Calibration and Validation for the Modelling of Cylindrical Pellets," *KONA Powder and Particle Journal*, vol. 32, pp. 236–252, 2015.

[22] N. Weerasekara, M. Powell, P. Cleary, L. Tavares, M. Evertsson, R. Morrison, J. Quist, and R. Carvalho, "The contribution of DEM to the science of comminution," *Powder Technology*, vol. 248, pp. 3–24, nov 2013.

[23] H. Zhang, Y. Tan, S. Shu, X. Niu, F. X. Trias, D. Yang, H. Li, and Y. Sheng, "Numerical investigation on the role of discrete element method in combined LBM-IBM-DEM modeling," *Computers & Fluids*, vol. 94, pp. 37–48, may 2014.

[24] Q. Wang, Y. Feng, J. Lu, W. Yin, H. Yang, P. J. Witt, and M. Zhang, "Numerical study of particle segregation in a coal beneficiation fluidized bed by a TFM-DEM hybrid model: Influence of coal particle size and density," *Chemical Engineering Journal*, vol. 260, pp. 240–257, jan 2015.

[25] N. Gui, W. Xu, L. Ge, and J. Yan, "LBE-DEM coupled simulation of gas-solid two-phase cross jets," *Science China Technological Sciences*, vol. 56, no. 6, pp. 1377–1386, may 2013.

[26] C. Bischof, *Parallel Computing: Architectures, Algorithms, and Applications*. IOS Press, 2008.

[27] A. Leonardi, F. K. Wittel, M. Mendoza, and H. J. Herrmann, "Coupled DEM-LBM method for the free-surface simulation of heterogeneous suspensions," *Computational Particle Mechanics*, vol. 1, no. 1, pp. 3–13, feb 2014.

[28] D. Gao and J. Sun, "Using DEM in Particulate Flow Simulations," *Cdn.Intechopen.Com*, pp. 29–50, 2003.

[29] Z. Y. ZHOU, S. B. KUANG, K. W. CHU, and A.-B. B. YU, "Discrete particle simulation of particle-fluid flow: model formulations and their applicability," *Journal of Fluid Mechanics*, vol. 661, pp. 482–510, aug 2010.

[30] C. Wensrich and A. Katterfeld, "Rolling friction as a technique for modelling particle shape in DEM," *Powder Technology*, vol. 217, pp. 409–417, feb 2012.

[31] K. G. Budinski, *Friction, Wear, and Erosion Atlas*. CRC Press, 2013, vol. 6.

[32] Y. Shao, *Physics and Modelling of Wind Erosion*. Springer Science & Business Media, 2008.

[33] S. M. Derakhshani, D. L. Schott, and G. Lodewijks, "Dust emission modelling around a stockpile by using computational fluid dynamics and discrete element method," in *Powders & Grains*, University of New South Wales (UNSW), Ed., Sydney, Australia, 2013, pp. 1055–1058.

[34] Andrew B. Cecala;, Andrew D. O'Brien;, Joseph Schall;, Jay F. Colinet;, William R. Fox;, Robert J. Franta;, Jerry Joy;, Wm. Randolph Reed;, Patrick W. Reeser;, John R. Rounds;, Schultz Mark J.;, A. B. Cecala, A. D. O'Brien, J. Schall, J. F. Colinet, W. R. Fox, R. J. Franta, J. Joy, W. R. Reed, P. W. Reeser, J. R. Rounds, and M. J. Schultz, "Dust Control Handbook for Industrial Minerals Mining and Processing," Department 0f Health and Human Services, Pittsburgh, WA, USA, Tech. Rep., 2012.

[35] R. Dennis and D. V. Bubenick, "Fugitive Emissions Control for Solid Materials Handling Operations," *Journal of the Air Pollution Control Association*, vol. 33, no. 12, pp. 1156–1161, dec 1983.

[36] C. Goniva, C. Kloss, and A. Hager, "An Open Source CFD-DEM Perspective," *5th OpenFOAM*, pp. 1–10, 2010.

[37] H. G. Weller, G. Tabor, H. Jasak, and C. Fureby, "A tensorial approach to computational continuum mechanics using object-oriented techniques," *Computers in Physics*, vol. 12, no. 6, p. 620, 1998.

[38] Y. Guo, "A coupled DEM / CFD analysis of die filling process," Ph.D. dissertation, The University of Birmingham, 2010.

[39] R. D. Mindlin and H. Deresiewicz, "Elastic spheres in contact under varying oblique forces," *J. Appl. Mech*, vol. 20, pp. 327–344, 1953.

[40] R. P. Jensen, T. B. Edil, P. J. Bosscher, M. E. Plesha, and N. B. Kahla, "Effect of Particle Shape on Interface Behavior of DEM Simulated Granular Materials," *International Journal of Geomechanics*, vol. 1, no. 1, pp. 1–19, jan 2001.

[41] M. Pasha, C. Hare, M. Ghadiri, A. Gunadi, and P. M. Piccione, "Effect of particle shape on flow in discrete element method simulation of a rotary batch seed coater," *Powder Technology*, nov 2015.

[42] Elias Gomes dos Santos, Luiz Carlos da Silva Carvalho, André Luiz Amarante Mesquita, and Alexandre Luiz Amarante Mesquita, "A study about the particle shape effect using the discrete element method (DEM)," in *15th Brazilian Congress of Thermal Sciences and Engineering*. Belém, PA, Brazil: ABCM, 2014.

[43] G. J. W. King and E. A. Dickin, "The evaluation of grain shapes in silica sands from a simple flow test," *Matériaux et Constructions*, vol. 5, no. 2, pp. 85–92, mar 1972.

[44] M. J. Vepraskas and D. K. Cassel, "Sphericity and Roundness of Sand in Coastal Plain Soils and Relationships with Soil Physical Properties1," *Soil Science Society of America Journal*, vol. 51, no. 5, p. 1108, 1987.

[45] F. J. Pettijohn, P. E. Potter, and R. Siever, *Sand and Sandstone*. Springer Science & Business Media, 2012.

[46] J. Ai, J.-F. Chen, J. M. Rotter, and J. Y. Ooi, "Assessment of rolling resistance models in discrete element simulations," *Powder Technology*, vol. 206, no. 3, pp. 269–282, jan 2011.

[47] K. Iwashita and M. Oda, "Rolling Resistance at Contacts in Simulation of Shear Band Development by DEM," *Journal of Engineering Mechanics*, vol. 124, no. 3, pp. 285–292, mar 1998.

[48] C. Kloss, C. Goniva, A. Hager, S. Amberger, and S. Pirker, "Models, algorithms and validation for opensource DEM and CFD-DEM," *Progress in Computational Fluid Dynamics*, vol. 12, no. 2-3, pp. 140–152, 2012.

[49] A. Jensen, K. Fraser, and G. Laird, "Improving the Precision of Discrete Element Simulations through Calibration Models," in *13th International LS-DYNA Users Conference*, Michigan, USA, 2014.

[50] N. I. Kolev, *Multiphase Flow Dynamics 2*, 2005, vol. 2.

[51] J. Matas, J. Morris, and E. Guazzelli, "Lateral Forces on a Sphere," *Oil & Gas Science and Technology*, vol. 59, no. 1, pp. 59–70, jan 2004.

[52] S. Sundaresan, "Multiphase Flow and Fluidization. By D. G IDASPOW . Academic Press, 1994. 467 pp. ISBN 0-12-282470-9." *Journal of Fluid Mechanics*, vol. 287, no. -1, p. 405, mar 1995.

[53] S. Ergun, "Fluid flow through packed columns," *Chemical Engineering and Processing*, vol. 48, pp. 89–94, 1952.

[54] R. Di Felice, "The voidage function for fluid-particle interaction systems," *International Journal of Multiphase Flow*, vol. 20, no. 1, pp. 153–159, feb 1994.

[55] J. Gidaspow, D.; Bezburuah, R.; Ding, "Hydrodynamics of circulating fluidized beds: Kinetic theory approach," in *7th international conference on fluidization*, Gold Coast, Australia, 1992.

[56] D. L. Koch and R. J. Hill, "Inertial Effects in Suspension and Porous media flows," *Annual Review of Fluid Mechanics*, vol. 33, no. 1, pp. 619–647, jan 2001.

[57] C. Wen and Y. Yu, "Mechanics of Fluidization," in *A.I.Ch.E. Series*, vol. 62, 1966, pp. 100–111.

[58] J. Richardson and W. Zaki, "Sedimentation and fluidisation: Part I," *Chemical Engineering Research and Design*, vol. 75, pp. S82–S100, dec 1997.

Chapter

3

CFD-DEM Modelling of the Single Particle Sedimentation

A number of numerical approaches with the ability of modelling the fluid-particle two-phase flows were reviewed in Chapter 2. It was concluded that the CFD-DEM method is the proper method for modelling dust liberation at the transfer point of a belt conveyor.

In this chapter, the reliability and accuracy of the CFD-DEM model is evaluated for a dilute regime of particle flow through modelling the SPS. The analytical solution [1], numerical results [2, 3], and experimental data [4] are used in the calibration, verification, and validation processes of the CFD-DEM model. Firstly, the CFD-DEM model is calibrated and the optimum ratio of the particle diameter to the CFD cell size ($D_p/\Delta x$) together with the drag force and voidage model are determined. In addition, a parametric study is conducted to investigate in which ratios of domain width to particle diameter W/D_p, the voidage models are usable so that the walls do not influence the simulation results. Secondly, the sedimentation of a particle from air into water is used to verify the calibrated model. Finally, the particle sedimentation at different particle Reynolds numbers is utilized to assess the validity of the verified CFD-DEM model.

In section 3.1, the analytical formulation of the SPS together with the equations

Parts of this chapter have been published in Engineering Computations, vol:33, iss:4 (2016).

of momentum exchange between the fluid and particle phases will be extracted in detail. In section 3.2, the benchmarking tests that are utilized in the calibration, verification, and validation of the CFD-DEM model will be presented. Finally, in section 3.3, the validity of CFD-DEM model will be investigated for a dilute regime of particle flow.

3.1 The analytical framework of the SPS

The trajectory and terminal velocity of a particle during the sedimentation process can be analytically extracted in order to be used in the accuracy evaluation of the numerical models [1, 5]. There is not particle-particle force ($\boldsymbol{f}_{pp,i} = 0$) for a single particle which leads to have the two-way coupling model [6]. The other influential forces in the SPS process are categorized into driving forces and damping forces. The only driving force in the SPS is the gravity force $m_i \boldsymbol{g}$ that forces the particle to settle downward through the fluid. On the other hand, the damping forces are the Archimedes or buoyancy force $\boldsymbol{f}_{A,i}$, drag force $\boldsymbol{f}_{d,i}$, virtual mass force $\boldsymbol{f}_{vm,i}$, Basset force $\boldsymbol{f}_{B,i}$, and Saffman $\boldsymbol{f}_{Saff,i}$ and Magnus $\boldsymbol{f}_{Mag,i}$ lift forces that act contrary to the gravitational force. The fluid-particle interaction force $\boldsymbol{f}_{pf,i}$ of Equation 2.20 is represented as follows:

$$\boldsymbol{f}_{pf,i} = \boldsymbol{f}_{A,i} + \boldsymbol{f}_{d,i} + \boldsymbol{f}_{vm,i} + \boldsymbol{f}_{B,i} + \boldsymbol{f}_{Saff,i} + \boldsymbol{f}_{Mag,i} \tag{3.1}$$

The lift forces, including Saffman and Magnus lift forces, are due to the rotation of the particle [7]. In this study, it is assumed that the particle is perfectly spherical and without rotational motion, therefore the effect of lift forces will be negligible. The Archimedes force $\boldsymbol{f}_{A,i}$ and the drag force $\boldsymbol{f}_{d,i}$ in Equation 3.1 are formulated as follows:

$$\boldsymbol{f}_{A,i} = \boldsymbol{g}\rho_f u_p \tag{3.2}$$

$$\boldsymbol{f}_{d,i} = \frac{1}{8} C_D \pi D_p^2 \rho_f {\boldsymbol{u}_p}^2 \tag{3.3}$$

In which, the C_D is the drag coefficient for a spherical particle. The following relation for the drag coefficient is proposed by Abraham [8].

$$C_D = \frac{24}{9.06^2}\left(\frac{9.06}{\sqrt{Re_p}} + 1\right)^2 \qquad 0.2 \leq Re_p \leq 1000 \tag{3.4}$$

$$Re_p = \frac{\rho_f u_p D_d}{\mu_f} \tag{3.5}$$

It should be noted that the drag coefficient has a constant value of 0.44 for the

Reynolds numbers bigger than 1000 and smaller than 2×10^5 [8].

The virtual mass force $\boldsymbol{f}_{vm,i}$ that is also called the apparent mass is the required force for accelerating the surrounding fluid around a particle. The Basset force $\boldsymbol{f}_{B,i}$ is because of the lagging boundary layer development with changing the relative velocity during the movement of a particle in the viscous fluid. The virtual mass force $\boldsymbol{f}_{vm,i}$ and Basset force $\boldsymbol{f}_{B,i}$ are presented below.

$$\boldsymbol{f}_{vm,i} = C_A \ \rho_f \boldsymbol{u}_p \ \frac{d\boldsymbol{u}_p}{dt} \tag{3.6}$$

$$\boldsymbol{f}_{B,i} = C_H \ {D_p}^2 \sqrt{\pi \rho_f \mu_f} \ \int_0^t \frac{\partial \boldsymbol{u}_p}{\partial t'} / \sqrt{t - t'} dt' \tag{3.7}$$

C_A and C_H are, respectively, the coefficients of the added mass and history term [9] that were determined by experiments [10]. The relation between the C_A, C_H, and the acceleration number $A_C = u_p^2/aD_p$ is illustrated in Figure 3.1. In which, 'a' is the acceleration of a particle during the movement within a fluid.

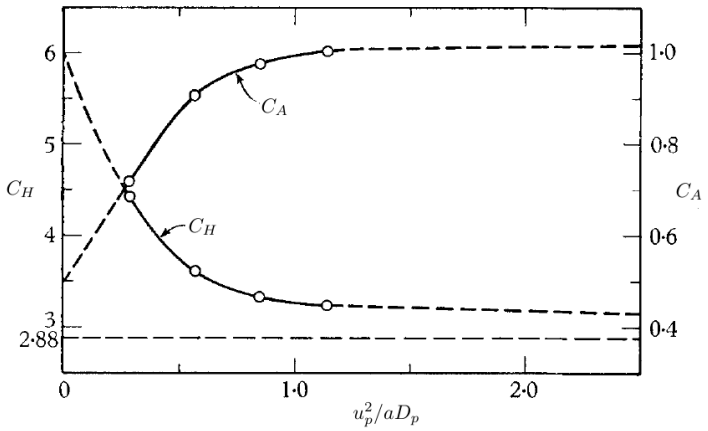

Figure 3.1: Variation of the coefficients of the added mass, C_A, and history term, C_H, with the acceleration number, $A_C = u_p^2/aD_p$, [11].

The sedimentation of a spherical particle inside a container consists of three stages: acceleration, constant speed, and deceleration. Each of these stages are influenced by a series of driving and damping forces. For instance, the Basset and virtual mass forces play a role in the acceleration state of the SPS and the lubrication force is an important force when a particle gets close enough to the wall of domain [12, 13].

The net forces acting on the particle become zero, when a particle reaches into constant speed which is known as the terminal velocity of particle u_t. At this stage, the weight of a spherical particle is exactly equal to the upward drag force and buoyancy force [14]. In other words, $\frac{du_p}{dt}$ gets zero in Equations 3.6 and 3.7. The balance of forces at the terminal velocity of a spherical particle is shown in

Equation 3.8.

$$m\boldsymbol{g} = \boldsymbol{f}_A + \boldsymbol{f}_d \tag{3.8}$$

Substitution of Equations 3.2 and 3.3 in Equation 3.8 and solving for terminal velocity u_t will yield the following expression:

$$u_t = \sqrt{\frac{4gD_p}{3C_d}(\frac{\rho_p - \rho_f}{\rho_f})} \tag{3.9}$$

In the Stokes flow where the inertial forces are small compared with viscous forces ($Re_p << 1$) [15], the drag force is represented by the following equation.

$$\boldsymbol{f}_{d,i} = 6\pi\mu D_p u_p \tag{3.10}$$

Substitution of Equations 3.10 in Equation 3.8 and solving for terminal velocity will yield to the terminal velocity of a spherical particle moving under Stokes flow condition as follows:

$$u_t = \frac{g{D^2}_p}{18\mu_f}(\rho_p - \rho_f) \tag{3.11}$$

In this study, the terminal velocity of a spherical particle will be used as a reference value in selecting the suitable drag force and voidage models as well as calibrating the CFD cell size and coupling interval in the CFD-DEM model.

3.2 Benchmarking tests

The calibration, verification, and validation of the CFD-DEM model needs to be conducted based on the reliable data such as analytical solution, numerical results, and experimental data. Bagherzadeh [1] analytically modelled the particle sedimentation within different fluids. Zhao et al. [2] and Derakhshani et al. [3] utilized the un resolved CFD-DEM method and fully resolved IBM-DEM method respectively to model a particle sedimentation within air and water. Cate et al. [4] experimentally extracted the trajectory and velocity of a settling particle within silicon oil for different Reynolds numbers. These experimental data was also used in the validation of the IBM-DEM method [3]. Hence, in the cases that the experimental data are not available like the study carried with Zhao [2], the results of IBM-DEM method will be utilized together with the analytical solution as reliable values to assess the accuracy of the CFD-DEM model. The results of these studied will be used in this research to study the sedimentation of a particle with unresolved and resolved CFD-DEM model.

3.2.1 Test set-up

The particle is located in (L/2, W/2, h) of the container and then it is released within the fluid at t=0 s. The geometric characteristics of benchmarking tests are illustrated in Figure 3.2.

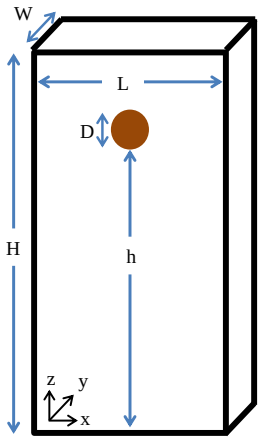

Size and position (mm)	Case A	Case B
Length (L)	20	100
Width (W)	10	100
Height (H)	30	160
Height of particle (h)	45	120
Particle diameter (D_p)	1	15

Figure 3.2: Schematic picture of domain geometry and particle position at t=0 s.

The particle sedimentation was investigated in cases A and B within three medium: air, water, and silicon oil. The physical properties of the fluids and particles involved in the simulations are presented in Table 3.1.

Table 3.1: The physical properties of fluid and particle phases used for benchmarking tests.

Type of fluids	Case ID	$\rho_f\,(kg/m^3)$	$\mu_f \times 10^{-3}\,(kg/m.s)$	$\rho_p\,(kg/m^3)$	$D_p\,(mm)$
Water [2]	A1	998.2	0.998	1.2	1
Air [2]	A2	1.19	0.0184		
Silicon oil [4]	B1	970	373	1120	15
	B2	965	212		
	B3	962	113		
	B4	960	58		

3.2.2 Calibration, verification, and validation plan

The CFD-DEM model is calibrated through determination of its parameters (CFD cell size and coupling interval) and sub-models (drag force and voidage models). Cases A1 and B1 are the benchmarking tests that are firstly used in the calibration of the CFD-DEM model.

As explained in section 2.3.3, the centre and divided voidage models are valid for the cases that the particle size is less than the CFD cells while the big particle model can be used even in the cases that the size of particle is larger than the CFD

cells. Accordingly, the CFD cell size, the voidage model, and the size of domain are dependent items that should simultaneously be considered in the calibration process.

Almost all iterative methods converge with a finer grid to a higher accuracy, but it requires considerable computational effort [16]. In this study, the grid dependency analysis is performed to determine the optimum size of the CFD cell. The grid dependency analysis is firstly performed for case A1 to determine the relation between the ratio of particle diameter to the CFD cell size $D_p/\Delta x$ and the voidage models. Four values of $D_p/\Delta x$ (0.5, 1, 2, and 4) are chosen to analyse the dependency of the simulation results on the CFD cell size. In this way, the validity of the centre and divided voidage models is also evaluated for the cases that the size of CFD cells is in the order of particle diameter.

In case B1, utilization of $D_p/\Delta x = 0.5$ will lead to have only three CFD cells in the width of domain ($W/D_p = 3$) that is not common in the CFD. Accordingly, the big particle model is the only usable model in this case and the $D_p/\Delta x$ of 2, 4, and 6 is used in the grid dependency analysis.

As already stated, the ratio of domain width to the particle diameter (W/D_p) is an important factor that should be considered in the calibration process. Therefore, a parametric study is conducted for case A1 to investigate in which ratios of W/D_p, the centre/divided voidage model is usable so that the walls do not influence on the simulation results.

The drag force and coupling interval are the other items that are selected in the calibration process. The CFD-DEM parameters and sub-models that are used in the calibration of the CFD-DEM model are presented in Table 3.2.

Table 3.2: Range of parameter variations and different models used in the CFD-DEM model.

Case ID	Drag model	Voidage model	Coupling interval	$D_p/\Delta x$	W/D_p
A [2]	Di Felice Gidaspow Koch-Hill	Centre Divided Big particle	10 and 100	0.5, 1, 2, 4	5, 10, 20
B [4]	Gidaspow Di Felice	Big particle	100	2, 4, 6	6.7

After calibrating the CFD-DEM model, the sedimentation of the particle from air (case A2) into water (case A1) is simulated to verify the CFD-DEM model. At the end, the experimental results that were carried out at particle Reynolds numbers ranging from 4.1 to 31.9 (cases B2 to B4) are used to validate the verified CFD-DEM model.

3.2.3 The accuracy of CFD-DEM model

The accuracy of simulation results are assessed in accordance with the percent error which is defined as the difference between the simulation results (S) and the reference

value (R) as follows:

$$Percent\,error = \frac{|R - S|}{R} \times 100 \tag{3.12}$$

The reference value in this study is selected based on the analytical result and the experimental data for case A and case B, respectively.

3.3 The CFD-DEM modelling of the SPS

The aim of this section is to calibrate the CFD-DEM parameters and to identify the proper sub-models of CFD-DEM method. As already mentioned, the terminal velocity of a particle during the sedimentation process will be used as a reference value to calibrate, verify, and validate the CFD-DEM model.

3.3.1 The CFD-DEM calibration

Grid Dependency Analysis ($D_p/\Delta x$)

Figure 3.3 shows the terminal velocity of a particle within water (case A1). As seen, the predicted terminal velocities with the centre and divided models at $D_p/\Delta x = 0.5$ are 0.150 m/s and 0.152 m/s, respectively. The obtained results are in agreement with the analytical value, 0.160 m/s, with the percent errors of 6.2% and 5.0% for the centre and divided models. On the other hand, by utilizing the finer grid ($D_p/\Delta x$=1), the void fraction of CFD cells tends toward zero where the centre and divided models are not valid [17].

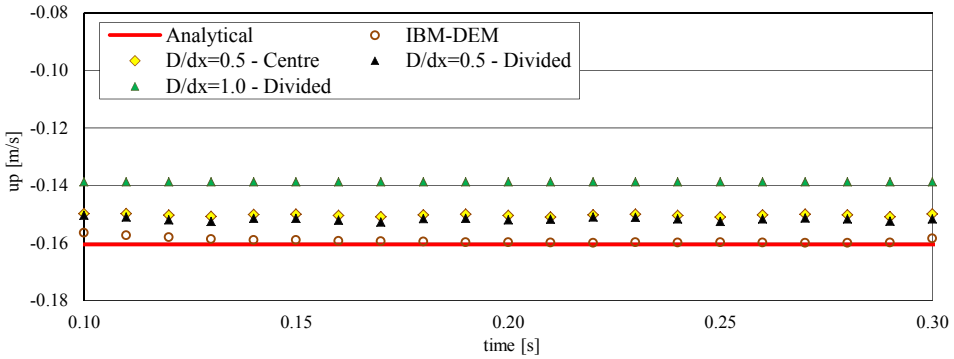

Figure 3.3: The effect of voidage models and the CFD cell size on the accuracy of the determined terminal velocity: case A1.

The big particle model with $D_p/\Delta x$ ratios of 2 and 4 was used to investigate the effect of utilizing the finer grid on the accuracy of the CFD-DEM model. Figure 3.4 shows that the terminal velocity of the particle is 0.152 m/s with the percent error of 5% for both ratios of $D_p/\Delta x$.

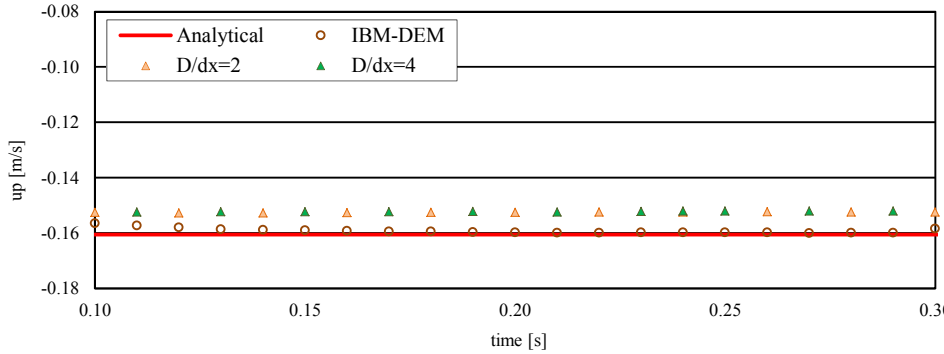

Figure 3.4: Evaluating the accuracy of big particle model versus the CFD cell size: case A1.

Hence, the grid dependency analysis along with the big particle voidage model was performed for case B1 to determine the proper value of $D_p/\Delta x$. The results of the grid dependency analysis are shown in Figure 3.5.

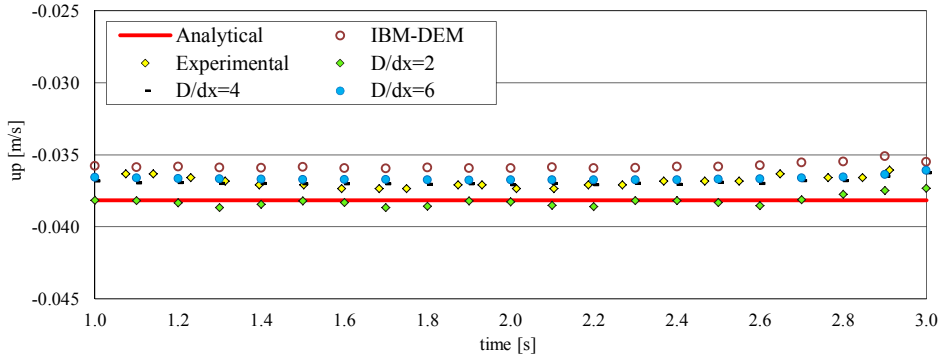

Figure 3.5: Assessing the accuracy of the big particle model for different size of CFD grid: case B1.

As seen, the terminal velocity of a particle with $D_p/\Delta x$=4 is 0.0369 m/s that is in good agreement with the analytical value, 0.0382 m/s, and the experimental result, 0.0373 m/s, with the percent error of 1.1%. It should be noted that the reported uncertainty of the experimental data is 5% [4] which confirms the accuracy of the CFD-DEM results.

The difference between the terminal velocity of the particle through utilizing the finer grid ($D_p/\Delta x = 6$) is very negligible which confirms $D_p/\Delta x = 4$ as the optimum size of the CFD cell. Consequently, the big particle model with $D_p/\Delta x = 4$ should be used in the cases that the utilization of the big particle model is unavoidable in the CFD-DEM model.

The CFD-DEM coupling interval

Typically, the information is exchanged between CFD and DEM models every 10-100 DEM time steps. Here, the effect of coupling interval on the computational time

and the accuracy of numerical results was evaluated for case B1. The experimental terminal velocity of case B1, 0.0373 m/s, was used to assess the accuracy of results. The CFD-DEM results according to the coupling intervals of 10 and 100 times DEM time step are compared in Table 3.3.

Table 3.3: Determining the optimum value of coupling interval between CFD-DEM.

Coupling interval [-]	Computational time [sec]	Terminal velocity [m/s]	Percent error [%]
10	42489	0.0389	4.3
100	2112	0.0386	3.5

The results indicated a significant difference between the computational time of two different coupling intervals. Hence, the coupling interval of 100 is selected because it is much faster than the other without significant compromising in the accuracy of results.

Drag force models

Figure 3.6 shows a comparison between the terminal velocities of a settling particle within water (case A1) for three different drag models: Di Felice, Gidaspow, and Koch-Hill.

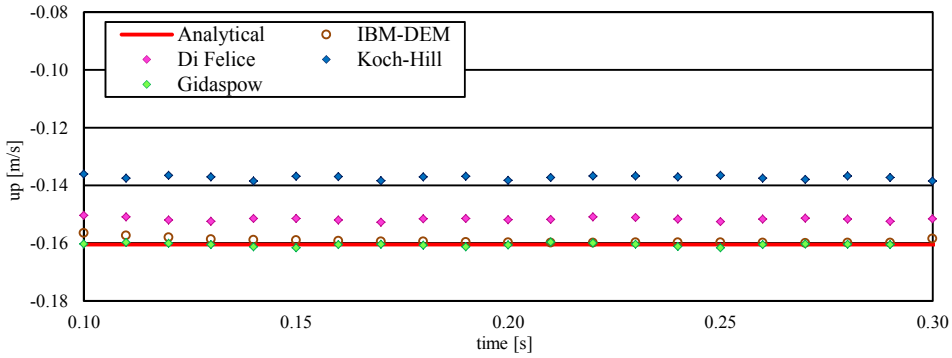

Figure 3.6: Evaluating the drag force models based on the analytical solution with $D_p/\Delta x = 0.5$ and Divided model: case A1.

It can be seen that the Di Felice and Gidaspow drag models are in better agreement with the analytical results than Koch-Hill. The percent error for Di Felice is 5.0% and for Gidaspow is 0.1%. The Di Felice and Gidaspow drag models were assessed again by the experimental data of a settling particle within silicon oil, case B1. Figure 3.7 shows that the results obtained by the Gidaspow drag model are very well fitted to experimental data with the percent error of 1.1%. Consequently, the Gidaspow drag model is considered as a reliable and accurate drag model and is selected for CFD-DEM simulations in this study.

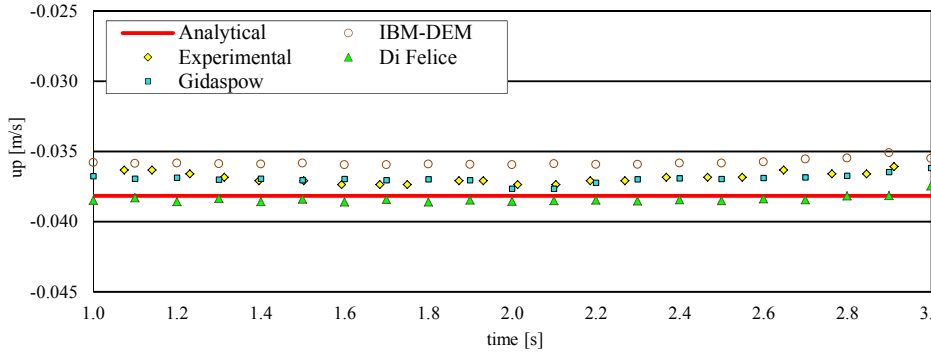

Figure 3.7: Evaluating the accuracy of drag force models based on the experimental data, IBM-DEM results, and analytical solution: case B1.

The domain size effect (W/D_p)

It was indicated in the previous parts that the divided and big particle models are respectively the proper voidage models in the modelling case A1 and case B1. The main reason that the divided model was not usable for case B was the W/D_p ratio.

A parametric study was conducted to check the validity domain of the voidage models based on W/D_p ratios. The ratio of W/D_p is 10 for case A according to Figure 3.2. Hence, it will be varied in the range of 5, 10 and 20 by assuming W=L to investigate the accuracy and validity of voidage models based on W/D_p.

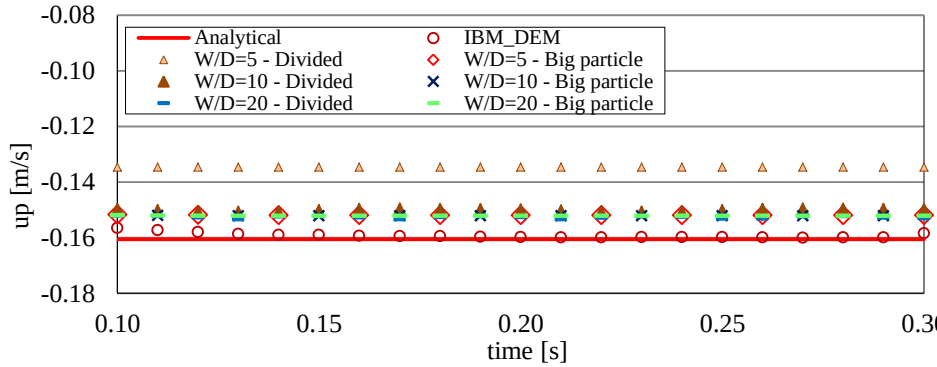

Figure 3.8: Evaluating the effect of domain size on the accuracy of CFD-DEM results base on case A1.

Figure 3.8 shows that the divided model becomes valid where W/D_p is larger than 10 while the big particle model is accurate in the whole range of W/D_p ratios. In addition, it was seen that the big particle model with $D_p/\Delta x$=4 is a reliable voidage model with the percent error of 5% even when the ratio of W/D_p is small in the order of 5.

Considering the computational expenses of the big particle model and the similarity between the results of big particle and divided models, it was concluded that the divided model can be used with W/D_p ratios bigger than 10 while the big particle model is usable for $5 \leq W/D_p$.

3.3.2 The CFD-DEM verification

In this part, sedimentation within the air into the water was used to verify the calibrated CFD-DEM model. As seen, when the particle enters into the water its speed decreases due to the strong viscous effect. After 0.2 second, the particle touches the bottom of the container and its speed gets zero. A comparison between the CFD-DEM results and numerical results of Zhao [2] for a particle that falls from air into water is shown in Figure 3.9.

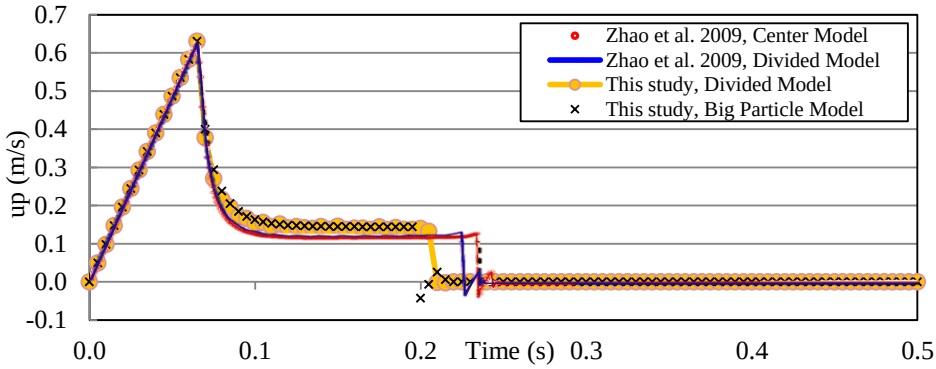

Figure 3.9: Particle sedimentation within air into water: a comparison between CFD-DEM results and results of Zhao et al. [2].

Evaluating the CFD-DEM results with the analytical solution indicated that all three voidage models are able to predict the terminal velocity of a settling particle. The difference between the results of Zhao and this study is 5% for both divided and big particle models. In this study, the particle reached to the bottom of the container about 0.03 second early because the predicted particle terminal velocity of this research within the water is about 5% bigger than Zhao's terminal velocity.

It was seen that the centre and divided models with $D_p/\Delta x$ of 0.5 and the big particle model with $D_p/\Delta x$ of 4 are respectively the proper CFD cell size and voidage models when the W/D_p ratio is greater than 10. Consequently, the parameters and sub-models that are presented in Table 3.4 are verified in this step and can be used in the validated model.

Table 3.4: Parameters and sub-models of the verified CFD-DEM model.

Case ID	$D_p/\Delta x$	Voidage model	Drag force model	Coupling interval
A	0.5	Divided	Gidaspow	100
B	4	Big particle		

3.3.3 The CFD-DEM validation

In this section, cases B2 to B4 were simulated with the verified CFD-DEM model to assess the validity of the model in accordance with cases that have already not been used in the calibration and verification processes. Figure 3.10 shows a comparison between the results of this study with the experimental data, analytical solution, and IBM-DEM results.

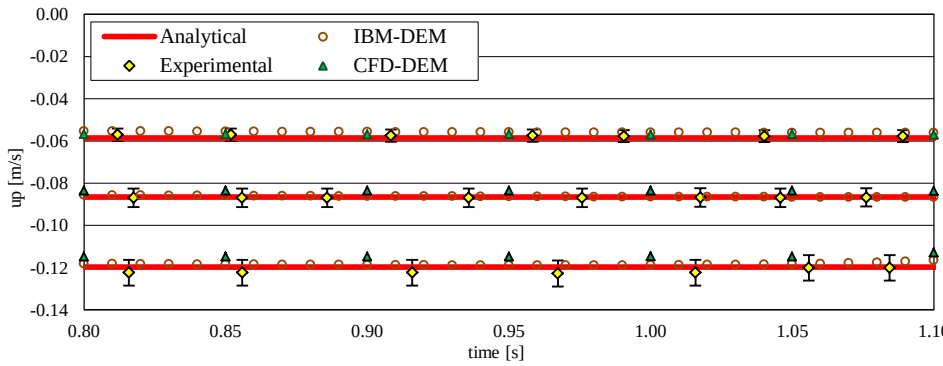

Figure 3.10: Validation of the CFD-DEM model based on the experimental results of cases B2 to B4.

The error bars in this figure illustrate 5% uncertainty for the experimental values [4]. The relative percent errors between the results of this study and experimental data for cases B2 to B4 are 1.6%, 3.7%, and 4.6%, respectively which indicate a good agreement between the simulation results and experimental data.

The percent error in case B4 increased because in this case the viscosity of silicon oil is less than the other cases which increases the terminal velocity of the particle. Therefore, the particle reaches into its terminal velocity in the places close to the bottom of container at $t = 1.05\,s$ while the sedimentation time is only $1.2\,s$. As already stated, the lubrication force has an important roll when a particle gets close to walls of domain which is not included in the CFD-DEM model of this study. Accordingly, it can be one of the reasons for the increase in the percent error of case B4 while still is less than the uncertainty of the experimental data.

Finally, it can be concluded that the CFD-DEM model with the proposed $D_p/\Delta x$, voidage model, coupling interval, and drag force model (see Table 3.4) is a reliable and accurate model for modelling a dilute regime of particle flow such as the SPS phenomenon.

3.4 Conclusions

The objective of this chapter was evaluating the accuracy and reliability of the CFD-DEM model through modelling a dilute regime of particle flow like a Single Particle

Sedimentation within different fluids. The results of this chapter are presented in the following.

1. There is not any inter-particle collision in the fluid-particle two-phase flows like the SPS. Consequently, the CFD-DEM model is validated for a dilute regime of particle flow which the 2-way coupling incorporates between the fluid and particle phases.

2. According to the grid dependency analysis, the ratio of the particle diameter to the CFD cell size ($D_p/\Delta x$) was determined equal to 0.5. This ratio along with the divided voidage model should be used where the ratio of the domain width to the particle diameter W/D_p is larger than 10.

3. The grid dependency analysis indicated that the big particle voidage model together with $D_p/\Delta x = 4$ can be utilized for $W/D_p > 5$ in the CFD-DEM model where the divided voidage is not applicable.

4. The numerical benchmarks indicated that the CFD-DEM results obtained with the Gidaspow drag force model are more accurate than the other drag force models. Also, the coupling interval of 100 times DEM time step will lead to sufficiently fast simulation and accurate enough results in the SPS modelling.

Bibliography

[1] M. Bagherzadeh, "Modelling single particle settlement by CFD-DEM coupling method," Ph.D. dissertation, Delft University of Technology, 2014.

[2] J. Zhao and T. Shan, "Coupled CFD-DEM simulation of fluid-particle interaction in geomechanics," *Powder Technology*, vol. 239, pp. 248–258, may 2013.

[3] S. M. Derakhshani, D. L. Schott, and G. Lodewijks, "Assessing Reliability and Accuracy of IBM-DEM Coupling Method: Modelling Single Particle Sedimentation," in *23rd Annual International Mechanical Engineering Conference*, Tehran, Iran, 2015.

[4] A. ten Cate, C. H. Nieuwstad, J. J. Derksen, and H. E. A. Van den Akker, "Particle imaging velocimetry experiments and lattice-Boltzmann simulations on a single sphere settling under gravity," *Physics of Fluids*, vol. 14, no. 11, p. 4012, 2002.

[5] C. Van Rhee, "On the sedimentation process in a Trailing Suction Hopper Dredger," Ph.D. dissertation, TU Delft, Delft University of Technology, 2002.

[6] S. Srivastava, K. Yazdchi, and S. Luding, "Mesoscale dynamic coupling of finite- and discrete-element methods for fluid-particle interactions," *Philosophical Transactions of the Royal Society A: Mathematical, Physical and Engineering Sciences*, vol. 372, no. 2021, pp. 20 130 386–20 130 386, jun 2014.

[7] J. Matas, J. Morris, and E. Guazzelli, "Lateral Forces on a Sphere," *Oil & Gas Science and Technology*, vol. 59, no. 1, pp. 59–70, jan 2004.

[8] F. F. Abraham, "Functional Dependence of Drag Coefficient of a Sphere on Reynolds Number," *Physics of Fluids*, vol. 13, no. 8, p. 2194, 1970.

[9] N. I. Kolev, *Multiphase Flow Dynamics 2*, 2005, vol. 2.

[10] F. Odar and W. S. Hamilton, "Forces on a sphere accelerating in a viscous fluid," *Journal of Fluid Mechanics*, vol. 18, no. 02, p. 302, mar 2006.

[11] F. Odar, "Verification of the proposed equation for calculation of the forces on a sphere accelerating in a viscous fluid," *Journal of Fluid Mechanics*, vol. 25, no. 03, p. 591, jul 1966.

[12] P. Poesio, G. Ooms, A. T. Cate, and J. C. R. Hunt, "Interaction and collisions between particles in a linear shear flow near a wall at low Reynolds number," *Journal of Fluid Mechanics*, vol. 555, p. 113, may 2006.

[13] W. Zhang, R. Noda, and M. Horio, "Evaluation of lubrication force on colliding particles for DEM simulation of fluidized beds," *Powder Technology*, vol. 158, no. 1-3, pp. 92–101, oct 2005.

[14] H. Lamb, *Hydrodynamics*, ser. Dover Books on Physics. Dover Publications, 1945.

[15] B. J. Kirby, *Micro- and Nanoscale Fluid Mechanics: Transport in Microfluidic Devices*. Cambridge University Press, 2010.

[16] F. Alobaid, J. Ströhle, and B. Epple, "Extended CFD/DEM model for the simulation of circulating fluidized bed," *Advanced Powder Technology*, vol. 24, no. 1, pp. 403–415, oct 2013.

[17] C. Kloss, C. Goniva, A. Hager, S. Amberger, and S. Pirker, "Models, algorithms and validation for opensource DEM and CFD-DEM," *Progress in Computational Fluid Dynamics*, vol. 12, no. 2-3, pp. 140–152, 2012.

Chapter

4

Determination of Micro-Macro Properties of Quartz Sand

The Single Particle Sedimentation (SPS) within air, water, and silicon oil was modelled with the CFD-DEM coupling method in Chapter 3. A number of parameters and sub-models of the CFD-DEM model were determined through modelling the SPS and assessing the validity of the CFD-DEM model with the experimental data. It was concluded that the validated CFD-DEM model is reliable for modelling a dilute regime of particle flow because only a single particle was employed in the SPS modelling.

In this chapter, the validated CFD-DEM model of Chapter 3 is re-evaluated for a dense regime of particle flow in which the inter-particle collisions are considered in the DEM simulation. For this purpose, a series of experiments are conducted and the CFD-DEM model of Chapter 3 is utilized to re-evaluate its validity based on experimental data for a dense regime of particle flow. The coefficients of rolling and sliding friction between the sand particles ($\mu_{r,pp}$ and $\mu_{s,pp}$) are determined with the DEM model as well as CFD-DEM model. Also, the effect of utilization of different boundary conditions in the DEM model is investigated.

A number of physical properties of sand particles will be introduced in section 4.1. In section 4.2, three sets of benchmarking tests will be used to re-evaluate the CFD-

Parts of this chapter have been published in Powder Technology **269**, 127 (2015) [1].

DEM model and to determine $\mu_{r,pp}$ and $\mu_{s,pp}$ as the microscopic properties of sand particles. The macroscopic properties of sand, namely, the Angle of Repose (AoR) and the discharging time of sand particles from an hourglass, will experimentally be measured in section 4.3. The microscopic properties of sand will be determined with the DEM model as well as the CFD-DEM models in section 4.4. Also, the effect of utilizing various DEM boundary conditions on the computational time of simulations will be examined in this section.

4.1 The physical properties of quartz sand

In Chapter 1 was explained that the particles with the diameters in the range 0.1-1.0 mm belong to the heavy industrial dust group. From the viewpoint of particle size, various types of materials such as sand can be located in this group of materials. Sand will be employed in this research, because it is the second most abundant mineral material on the surface of earth [2] and the fine particles of the sand composition can be liberated as the dust at the transfer point of a belt conveyor.

Various types of sand with different physical properties are widely employed in the industrial process. Hence, It is necessary to have an accurate and reliable determination of the physical and mechanical properties of sand to use in the numerical model. In order to determine the physical properties of sand, a series of experiments are conducted to measure the particle and bulk density of sand together with the Particle Size Distribution (PSD) of sand particles.

The AoR as one of the macroscopic properties of quartz sand is measured in this study. Two main types of the AoR, namely, the static and dynamic angles, were widely used in earlier studies [3–5]. Also, there are at least eight methods of measuring the AoR with slightly different values of the AoR [6, 7]. There are several technical issues such as human factors, test procedure, equipment design, and methods of evaluation that affect the amount of the AoR. Therefore, the published values of the AoR for the same materials are rarely comparable with each other. In this study, three different series of experiments; hourglass, rectangular container, and conical pile formation; are carried out to measure the AoR of quartz sand together with some other values.

The other macroscopic property, known as the discharging time, is the time that it takes the particles to leave the top part of an hourglass. This value is used along with the AoR to accurately determine the coefficients of rolling ($\mu_{r,pp}$) and sliding ($\mu_{s,pp}$) friction of quartz sand with the CFD-DEM model.

4.1.1 Particle Size Distribution (PSD)

A sieve analysis is performed to determine the particle size distribution of the materials. Sieve analysis is one of the traditional measurement techniques for the separation of fine particles from coarse particles by means of a meshed or perforated surface. This method is frequently used because of its simplicity, cheapness, availability, and

precision. Available sieve sizes are regulated by standards. The standard sieve series are specified in ISO 565:1990, ISO 3310-1:2000 (international), EN 933-1 (European) and ASTM E11:01 (US). In this study, ISO 3310-1:2000, which is based on the principle of a fixed ratio between the sieve openings, was used to evaluate the granulometry of quartz sand. In the ISO standard, the relation between sieve size and the particular size is specified by number series that are called preferred numbers [8]. The nominal aperture sizes of wire mesh series used in this study were 0.063, 0.150, 0.212, 0.300, 0.425, 0.500 and 0.6 mm. Also, the nest of sieves is assembled with the coarsest mesh at the top to the finest mesh at the bottom and then the sieve test carried out by a vibrating machine for 10 min. Also, before each experiment, the powder was stored in the drying oven ($120°C$) for at least 24 h, which could make them dried completely.

4.1.2 Particle and bulk density

Particle density is a relatively well-defined quantity. Particle density is not dependent on the degree of compaction of material, whereas the bulk density has different values depending on whether it measures in the freely settled or compacted state [9].

In this study, the particle density is determined using an ultra-pycnometer 1000. By putting the sand inside the sample cell, the ultra-pycnometer measures the occupied volume of the sample cell through the injection of helium inside the sealed sample cell. By default, this procedure is repeated for five times by ultra-pycnometer and at the end the average density of sand particles is measured by the pycnometer.

The most common method of measuring the bulk density is collecting a known volume of the sample without any compaction and determining the mass. Measurements of bulk density are commonly made by carefully collecting a soil sample of known volume and then drying the sample in an oven to determine the dry mass fraction. In this study, the same procedure is done to determine the bulk density of dried quartz sand.

4.2 Benchmarking tests

The hourglass, rectangular container, and conical pile formation are three different tests that are carried out to measure the macroscopic properties of quartz sand. The test procedure is described in the following.

4.2.1 The hourglass

The hourglass was used to measure two macroscopic properties of quartz sand, namely, the discharging time and the AoR. Figure 4.1 shows the laboratory equipment that was used in the determination of these two macroscopic properties. The inner diameter of the upper transparent chamber is $32\,mm$ which fills with a certain amount of quartz sand. Sand particles flow from the top part when the plug of the

hourglass neck is pulled ($t = 0\,s$). The time that it takes the sand particles to leave the upper part of the hourglass is measured as the discharging time with an accuracy of $\pm 0.1\,s$.

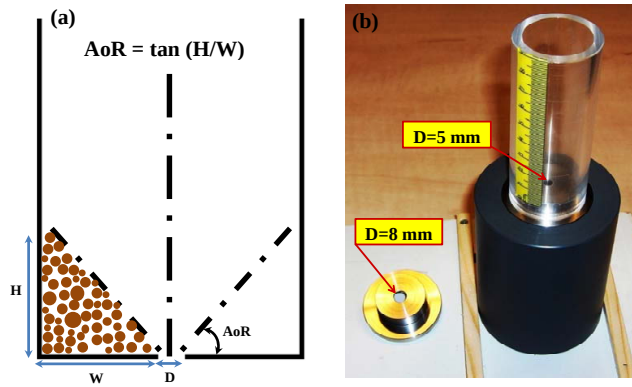

Figure 4.1: a) Schematic picture of the calculating method of the AoR within the hourglass b) The hourglass experimental set-up that was used in the measurement of the AoR and discharging time.

The AoR and discharging time of the sand particles is measured for different amounts of sand: 25, 50, and 75 g. Also, two different neck diameters of the bottom lid, 5 and 8 mm, are used to determine the effect of neck diameter on the discharging time. In each experiment, the AoR of the sandpile is measured when the sand particles on the upper part of the hourglass gets stable.

4.2.2 The conical pile formation

Conical piles form in many industrial processes and especially in bulk terminals while materials are stored in the yards. In this study, two methods are employed to form a conical pile: funnel method and cylindrical method.

In the funnel method, the sand particles are poured over a base through a funnel that is kept close to the tip of the sand pile to decrease the effect of particle velocity on the AoR. Figure 4.2 shows the other way of conical pile forming that is the cylindrical method. In this method, sand particles are poured into a hollow cylinder and then the cylindrical wall moves upward with a constant speed to create a conical pile. The velocity of the cylinder is a key parameter that affects the AoR. Here, the cylinder lifts upward with a constant speed of $10\,mm/s$ and then it is kept in the constant height of $10\,mm$ from the base. The conical pile gradually forms during the discharging process of quartz sand.

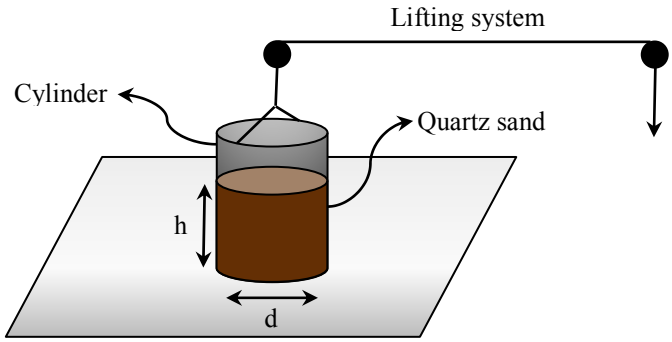

Figure 4.2: Schematic picture of the experimental set-up to determine the AoR in the conical pile formation test.

4.2.3 The rectangular container

The rectangular container test is an experimental technique to illustrate the effect of a domain on the macroscopic properties of the materials. In this research, a rectangular container with adjustable walls is utilized to investigate the effect of walls on the AoR for various widths of container. The experimental set-up of rectangular container is shown in Figure 4.3.

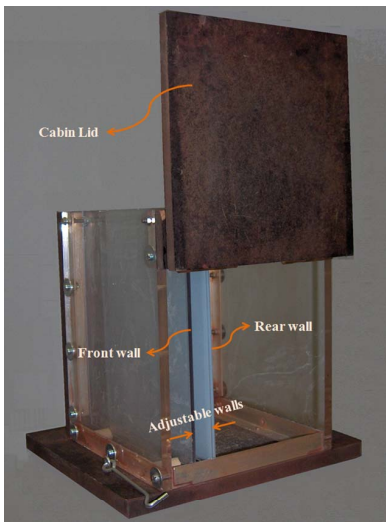

Figure 4.3: Experimental set-up of the rectangular container (sand particles are poured between the front and rear walls).

The front and rear walls of container have an additional restriction on the mobility of particles that are in contact with them. Indeed, the particles close to the walls are influenced by the walls and it is propagated into the particle assembly in the whole

domain. To investigate the wall effect on the AoR, two adjustable walls are placed inside the container while the distance between these walls can be changed between 4 to 200 times the particle diameter. The distance between the walls is increased to the extent that the AoR gets constant in the mid plane of the container. This distance is the critical width of the container where the front and rear walls do not any influence on the AoR.

4.3 Experimental results

Determining the uncertainty of experimental results is an important issue in the laboratory activities. In this section, the uncertainty of the AoR and discharging time is determined. The physical properties of sand are measured by a series of experiments and then the experimental results of the benchmarking tests are presented in detail.

4.3.1 Uncertainty of experimental results

No physical quantity can be measured with perfect certainty, hence experimental measurements are subject to some uncertainties [10]. Experimental error is the difference between a measurement value and the true value. The four main sources of experimental uncertainties are limited accuracy of the measuring apparatus, limitation and simplifications of the experimental procedure, uncontrolled environment changes and human errors [11].

Determination of the uncertainty in the experimental results is performed based on the applicability of the results. The experimental results of this study are supposed to be used in validation of the numerical results, therefore, each experiment is repeated several times to obtain a consistence average of the desired quantities.

The AoR is one of the quantities that is experimentally measured with various levels of uncertainty. According to the accuracy of the chronometer which was used to measure the discharging time, the uncertainty of the measured time is in the order of $\pm 0.1\,s$ which was confirmed through repeating the experiments for three times. Grasselli and Herrmann [12] did a series of experiments to measure the AoR of a pile for the powder material with a particle size of $0.250\,mm$. They determined the AoR with the uncertainty of $\pm 1.6°$. The experimental observations of this study revealed that the uncertainty of the measured angle of reposes is in the order of $\pm 1.1°$ which is about the $\pm 2.8\%$ of the measured angles.

4.3.2 Determining the PSD of quartz sand

The Particle Size Distribution (PSD) is another mechanical properties of material that is important because of its application in the modelling the dust liberation phenomenon. Hence, it is necessary to determine the PSD of quartz sand to be used in the DEM model. A sieve analysis was performed to characterize the particle

size distribution of quartz sand and the result of the sieve analysis is illustrated in Figure 4.4.

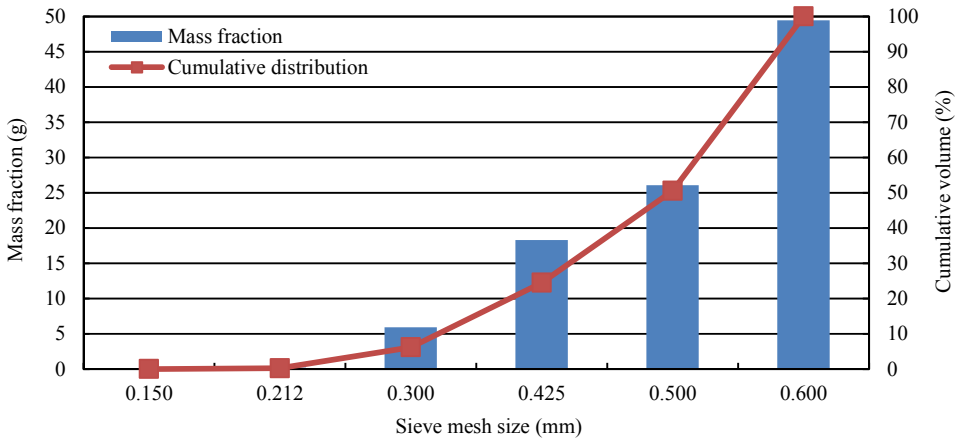

Figure 4.4: Sieve analysis results of quartz sand based on ISO 3310-1:2000 standard.

The experimental results indicated that the D_{50} value of quartz sand is $0.600\,mm$. Table 4.1 shows the PSD of quartz sand that is used in DEM simulation in which contains a wide range of particle diameters; from fine particles to coarse particles.

Table 4.1: Particle size distribution of quartz sand used in DEM simulation.

Particle diameter (mm)	Mass of sand (g)	Mass fraction (%)	Cumulative distribution (%)
0.300	14.18	6.21	6.21
0.425	41.71	18.29	24.50
0.500	59.39	26.05	50.55
0.600	112.78	49.45	100

4.3.3 Particle and bulk density of quartz sand

The average of five experiments with the deviation of 0.005% shows that the particle density of quartz sand is equal to $2653\,kg/m^3$. It was observed that repeating an experiment for three times results in a consistent value for the bulk density of quartz sand. The experimental results indicated that the bulk density of quartz sand is $1530\,kg/m^3$.

4.3.4 The hourglass test

The hourglass was filled with three different amounts of sand 25, 50, and 75 g, which led to different discharging times.It was observed that three times is sufficient to repeat each experiment to make sure about the consistency of the results. The

experimental results are presented in Table 4.2 for two different sizes of the hourglass neck.

Table 4.2: Discharging time of quartz sand versus the amount of sand in the hourglass test.

Neck diameter of hourglass (mm)	Mass of sand (g)	Experimental discharging time (sec)	AoR (degree)
5	25	6.6	41.6
	50	16.2	41.6
	75	25.3	41.6
8	25	2.6	38.8
	50	4.9	39.8
	75	7.3	39.8

4.3.5 The Conical pile formation test

Figure 4.5 shows the experimental results of the conical pile test that were obtained by the cylindrical method and the funnel method.

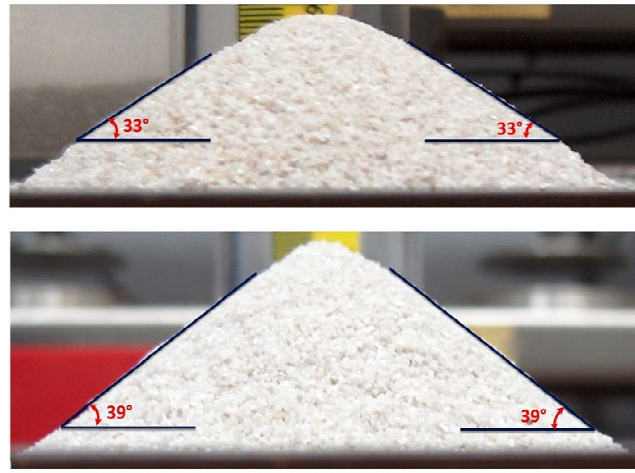

Figure 4.5: A comparison between the Angle of Repose of the conical pile which formed with the cylindrical method (top) and funnel method(bottom).

The experimental results indicated that the mean values of the AoR based on the cylindrical and funnel methods are 33° and 39°, respectively. This is in accordance with previous research [7] that illustrated the dependency of the AoR on the experimental method. The difference between the AoR can be explained by the concept of mean kinetic energy of particles. In the cylindrical test when the walls moved up, the majority of particles dropped down, while at the funnel test, particles were poured slowly over the base so that the average kinetic energy of particles in the cylindrical test are higher than the averaged kinetic energy of particles in the funnel test.

4.3.6 The rectangular container test

The effect of the boundary condition on the AoR was checked through utilization of the adjustable domain. The width of container was changed from 4 to 200 times of the D_{50} of sand particles. The wall effect on the amount of the AoR for particles close to the wall and particles in the central plane of container is illustrated in Figure 4.6. The experimental results show that the AoR in the middle plane of container tends toward 35.1° while the AoR is close to 36° for the particles near the walls. This difference shows that the wall effect on the AoR should be considered in the DEM simulations.

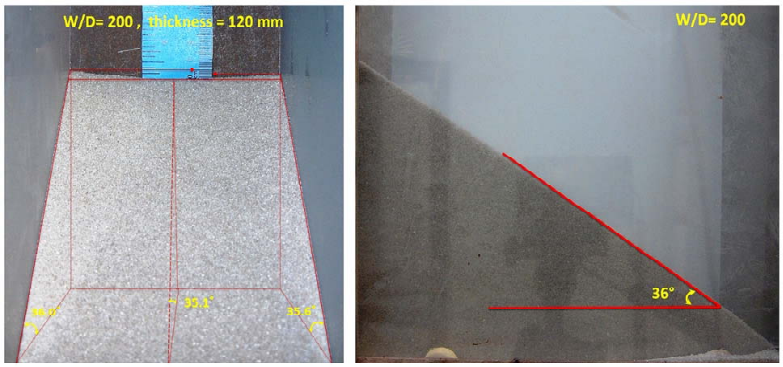

Figure 4.6: The variation of the AoR on the middle plane versus the distance between the adjustable walls for $W/D_p = 200$.

The distance between the adjustable walls is gradually increased from 4 to 200 times of particle diameter to investigate the variations of the AoR according to the changes of the container width. The variations of the AoR versus the container width is shown in Figure 4.7.

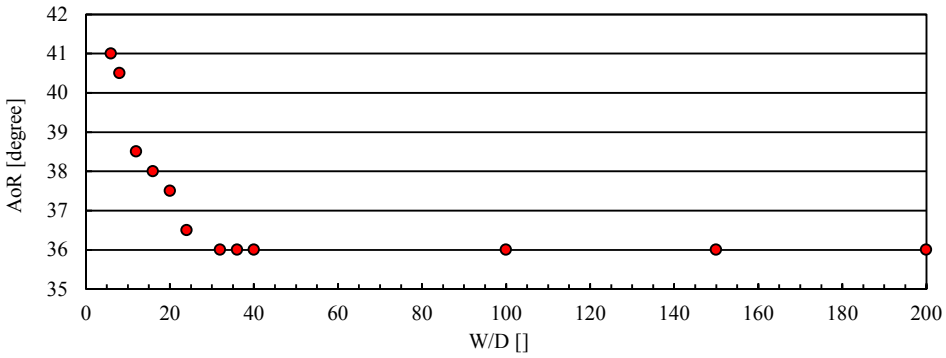

Figure 4.7: The variation of the AoR versus W/D_p in the rectangular container test.

It was observed that the AoR gets constant when the container width is larger

than 32 times of the particle diameter. Therefore, the critical value of container width is 32 because the walls do not have any more effect on the assembly of particles that are located in the centre of the container.

4.4 Determining the microscopic properties of quartz sand

The DEM model needs to be initialized by a number of material properties. In this study, it is assumed that the sand particles are spherical and non-cohesive material. Some properties of quartz sand that were used in DEM modelling are presented in Table 4.3.

Table 4.3: Properties of quartz sand used in the DEM simulations.

Parameter	Symbol	Base value
Particle diameter	D_p	Table 4.1
Particle density	ρ_p	2653 kg/m^3
Young's modulus	E	50e6 N/m^2
Poisson ratio	ν	0.3
Coefficient of restitution	e	0.9 [13]

The time step of the DEM model is the other important parameter that has a considerable effect on the accuracy of DEM results and the numerical computation time. By considering the Rayleigh and Hertz criteria [14] and running a number of benchmark simulations, the proper time-step for DEM simulation was determined equal to 2.0e-06 s, which is in the order of 10% of Rayleigh time step.

The first simulation stands on the experimental results of the hourglass test, including the discharging time and the AoR. In this simulation, the coefficients of rolling and sliding friction, $\mu_{s,pp}$ and $\mu_{r,pp}$, are calibrated by the experimental results. The verification stage is performed with a new set of the experimental results of the hourglass. At the end, the verified DEM will be validated by doing a comparison between the experimental results of the conical pile test and DEM simulations. This process is shown in Figure 4.8. The same process is conducted for the CFD-DEM model to assess the effect of air on the amount of determined values of $\mu_{s,pp}$ and $\mu_{r,pp}$.

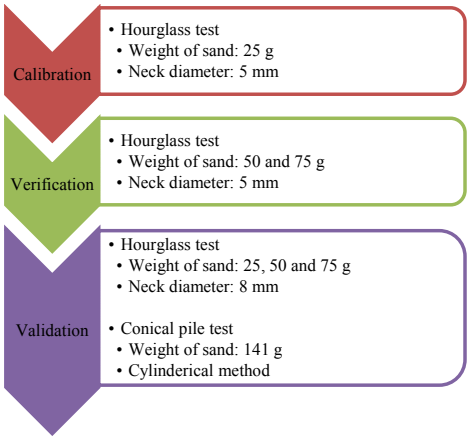

Figure 4.8: A flowchart of calibration, verification, and validation process of the DEM and CFD-DEM models together with the specification of the experimental tests.

4.4.1 Accuracy assessment of the numerical results

The accuracy of DEM and CFD-DEM simulations, which is the closeness of the simulation results to the experimental values [11], should be evaluated by an accredited criterion. In this study, the percent error is used as a criterion to assess the accuracy of simulation results so that the experimental results are considered as the reference data (R) in the percent error(see Equation 3.12).

The Maximum Allowable Percent Error (MAPE) is a criterion that is used in this study. In order to determine the maximum allowable percent error of the simulation result, knowing the minimum amount of experimental result (E) and the uncertainty of experimental and simulation results is necessary. The uncertainty of the measured time and the AoR in this study is in the order of $\pm$ 0.1 s and $\pm 1.1^{\circ}$, respectively. Also, the same numerical uncertainty is assumed for the simulation results of the measured time and the AoR. The relation that is used to determine the MAPE is as follows:

$$Maximum\,Allowable\,Percent\,Error\,(MAPE) = \frac{|2 \times R_{uncertainty}|}{R_{min}} \times 100 \quad (4.1)$$

The MAPE criterion is actually the maximum relative error that is possible to be observed between the results of a quite similar experiment due to the uncertainty of the experimental results. For instance, if the measured time is $R_{min} = 2.0\,sec$ with the uncertainty of $R_{uncertainty} = \pm 0.1\,sec$, the MAPE will be calculated as follows:

$$MAPE = \frac{|(R_{min} + |R_{uncertainty}|) - (R_{min} - |R_{uncertainty}|)|}{R_{min}} \times 100 \quad (4.2)$$

According to the assumed values for R_{min} and $R_{uncertainty}$, the MAPE will be 10% which means the possibility of a relative error in the order of 10% even between the results of a quite similar experiment. Consequently, the maximum acceptable relative error between the experimental data and simulation results of this example is assumed to be 10%.

4.4.2 DEM calibration: Modelling the hourglass

It was confirmed in literatures [15] and [16] that the different combinations of the coefficients of rolling and sliding friction in DEM simulation can lead to an identical AoR. In this study, the discharging time was measured along with the AoR in the experiments in order to determine the reliable and practical values for coefficients of rolling and sliding friction of the sand particles.

The hourglass with the same geometry of the experimental set-up was simulated with DEM to determine the microscopic properties of sand particles. The number of particles in DEM simulations was 162,997 particles which represents 25 g of quartz sand. In the DEM simulation, the coefficients of rolling and sliding friction as two main microscopic properties of granular materials are changed according to the ranges indicated in Table 4.4.

Table 4.4: The variation range of coefficients of rolling and sliding friction in DEM simulation.

Parameter	Variation range
Coefficient of sliding friction	0.2 - 0.7
Coefficient of rolling friction	0.0 - 0.5

Figure 4.9 shows the contour plot of the AoR as a function of $\mu_{s,pp}$ and $\mu_{r,pp}$ for 25 g of quartz sand. These results have been achieved for an hourglass with the neck diameter of 5 mm. With the increase in the value of $\mu_{s,pp}$ and $\mu_{r,pp}$, the AoR will gradually increase until $\mu_{s,pp}$ and $\mu_{r,pp}$ reach to 0.7 and 0.5, respectively. At these values, the blockage occurred and particles remained in the top part of the hourglass. These values are considered as the upper limits of the coefficients of friction in DEM simulation.

As expected, the AoR gradually increases with the increase of the coefficients of friction. The discharging time, the amount of the time that takes the sand particles leave the top part of the hourglass, was employed as the second macroscopic property in the calibration process. This time depends on the various parameters like coefficients of friction, neck diameter of the hourglass, and the amount of material.

The contour plot of the discharging time for 25 g of sand particles as a function of $\mu_{s,pp}$ and $\mu_{r,pp}$ is shown in Figure 4.10. As seen, the discharging time decreases as the coefficient of rolling friction increases. Indeed, a lower amount of sand leaves the hourglass because increasing the coefficient of rolling friction increases the AoR. Consequently, particles inside the hourglass get stable much faster than a low coefficient of rolling friction.

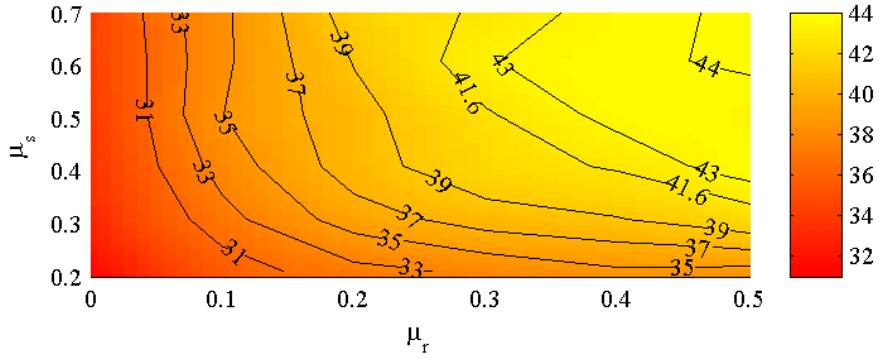

Figure 4.9: Effect of rolling and sliding coefficients of friction on the AoR for 25 g of quartz sand.

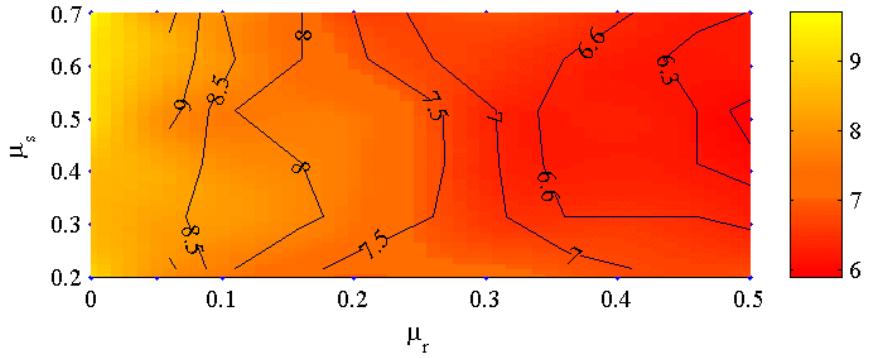

Figure 4.10: Effect of rolling and sliding coefficients of friction on the discharging time for 25 g of quartz sand.

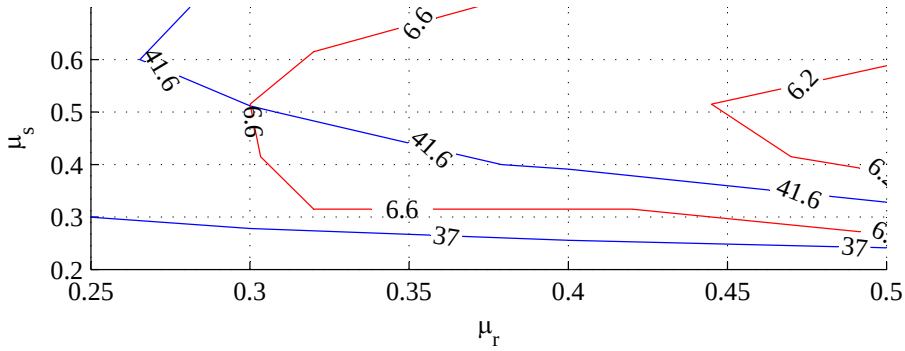

Figure 4.11: Intersection of AoR and discharging time of DEM simulations based on the experimental results for 25 g of quartz sand.

According to Table 4.2, the AoR is 41.6° and the discharging time experimentally took 6.6 s for 25 g of sand. The comparison between the DEM and experimental results for this amount of sand indicated that the coefficients of rolling and sliding friction should be 0.30 and 0.52, respectively. The intersection of these values versus the different combination of coefficients of friction is shown in Figure 4.11.

The accuracy and reliability of the calibrated model was verified by a new series of experimental results. For this purpose, the experimental results of the hourglass for 50 and 75 g of quartz sand in addition to the results that were obtained for the hourglass with the neck diameter of 8 mm were compared with the results that obtained with the calibrated DEM model.

Table 4.5: Verification of the calibrated DEM model according to the AoR for different amount of quartz sand.

Neck diameter of hourglass (mm)	Mass of sand (g)	AoR (degree)		Percent error (%)
		Experimental	DEM	
5	25	41.6	41.1	0.5
	50	41.6	42.8	2.9
	75	41.6	41.5	0.2
8	25	38.8	40.2	3.6
	50	39.8	41.1	3.3
	75	39.8	41.6	4.5

Table 4.6: Verification of the calibrated DEM model according to the discharging time for different amount of quartz sand.

Neck diameter of hourglass (mm)	Mass of sand (g)	Discharging time (sec)		Percent error (%)
		Experimental	DEM	
5	25	6.6	6.3	4.5
	50	16.2	15.3	5.6
	75	25.3	23.5	7.1
8	25	2.6	2.8	7.7
	50	4.9	4.7	4.1
	75	7.3	6.8	6.8

The minimum experimental values of the AoR and discharging time are 38.8° and 2.6 sec, respectively. Therefore, the MAPE values of AoR and discharging time will be 5.7% and 7.7% and the percent error of the simulation results should be less than these values (see section 4.4.1). As seen in Tables 4.5 and 4.6, the percent errors of DEM results are less than the MAPE values and consequently, the DEM model is verified based on the determined values for $\mu_{s,pp}$ and $\mu_{r,pp}$.

4.4.3 DEM validation: Modelling the conical pile formation

In this part, the validity of the verified DEM model was assessed by simulating a conical pile. The domain of DEM simulation is similar to the experimental domain of the conical pile test. The granulometry of quartz sand is based on the PSD given in Table 4.1 and the coefficients of rolling and sliding friction are 0.3 and 0.52, respectively. The wall of cylinder moved up with a constant velocity of 10 mm/s until the height of 10 mm. The conical pile gradually shaped with giving enough time to the sand particles to be settled on the base. The mean kinetic energy of particles was used as a criterion in the DEM simulation to assess the stability of the sandpile. In this study, the reference value of the mean kinetic energy of particles is $10^{-9}\, kg.m2/s2$ which means at this value the sandpile is stable and the DEM simulation results are ready for post processing.

The experimental value of the AoR was 33° in the cases that the conical pile was formed through the cylindrical method. In this experiment, the MAPE value of the experimental results with uncertainty of ±1.1° is 6.6%. Figure 4.12 shows that the average AoR of DEM simulation for the conical pile test is 34.2° with the percent error of 3.6% which is less than MAPE value and confirms the validation of the DEM model.

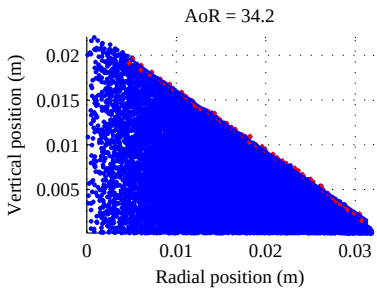

Figure 4.12: The comparison between the AoR of experimental data and DEM result.

4.4.4 CFD-DEM modelling of the hourglass

The microscopic properties between the sand particles, $\mu_{s,pp}$ and $\mu_{r,pp}$, can numerically be determined in two different ways: with and without considering the air effect in the calibration process. In section 4.4.2, the microscopic properties were determined by DEM and without considering the effect of air. In this section, the air effect on the calibrated microscopic properties of the DEM model was evaluated through coupling DEM model with CFD model.

The determined values of $\mu_{s,pp}$ and $\mu_{r,pp}$ was used in CFD-DEM model for the hourglass with 25 g of quartz sand and neck diameter of 5 mm. Table 4.7 presents the values and sub-models of the CFD-DEM model that are based on results obtained in Chapter 3.

Table 4.7: Numerical settings of CFD-DEM modelling of 25 g of quartz sand.

Drag model	Void fraction model	Coupling interval	Time step (*sec*)		Friction coefficient	
			DEM	CFD	μ_s	μ_r
Gidaspow	Divided	100	2.0e-6	2.0e-4	0.48, 0.50	0.27, 0.28
Archimedes					0.52, 0.55	0.30, 0.32

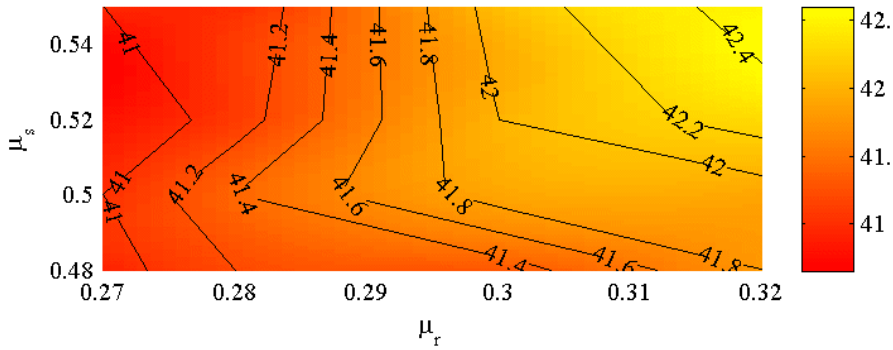

(a) The contour plot of the AoR (sec)

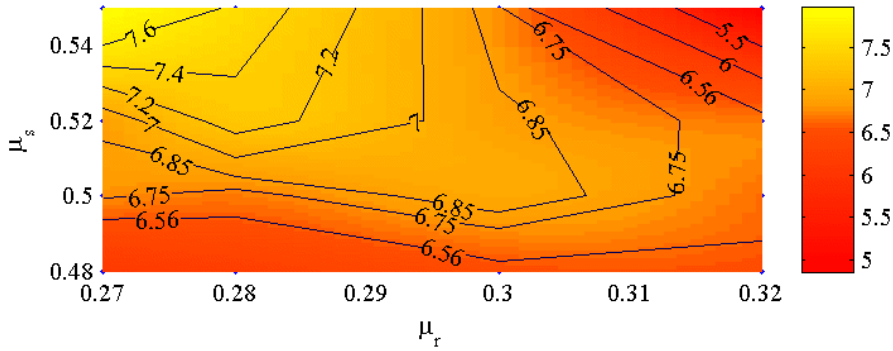

(b) The contour plot of the discharging time (sec)

Figure 4.13: The variations of the AoR and discharging time in accordance with the changes of coefficients of rolling and sliding friction: D=5 mm, m_p= 25 g.

The majority of particles get stable at the mean kinetic energy of $10^{-09}\, kg.m^2.s^{-2}$. The CFD-DEM simulations were conducted on a node with 16 GB of memory and two quad cores 2.33 GHz processors, so that each simulation took approximately 3 days. Figure 4.13 shows the contour plot of the AoR and discharging time as a function of $\mu_{s,pp}$ and $\mu_{r,pp}$ for 25 g of quartz sand.

Table 4.2 shows that the experimental values of AoR and discharging time are 41.6 ° and 6.6 s, respectively. The intersection point of these values specifies $\mu_{r,pp}$ and $\mu_{s,pp}$ with decimal places up to 3 in Figure 4.14. In the field of DEM studies, it is common to use values with decimal places up to 2 for coefficients of friction.

Hence, the specified $\mu_{r,pp}$ and $\mu_{s,pp}$ in Figure 4.14 were rounded up to 2 decimal places and $\mu_{r,pp}$ and $\mu_{s,pp}$ was determined equal to 0.30 and 0.49, respectively.

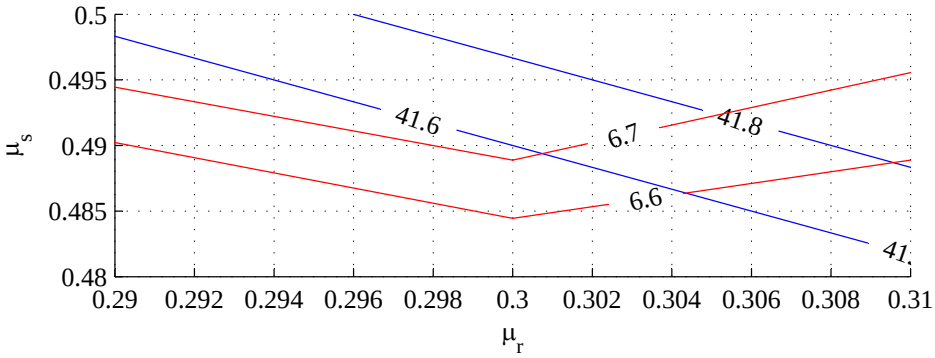

Figure 4.14: Intersection of AoR and discharging time at AoR of 41.6 ° and discharging time of 6.6 s: D=5 mm, m_p= 25 g.

To assess the validity of the determined values for $\mu_{r,pp}$ and $\mu_{s,pp}$, CFD-DEM simulations were conducted for 50 and 75 g in the hourglass with the neck diameter of 5 and 8 mm. Tables 4.8 and 4.9 show a comparison between the AoR and discharging time of CFD-DEM results and experimental data.

As seen in Tables 4.8 and 4.9, the CFD-DEM results are less than the MAPE values of AoR and discharging time (5.7% and 7.7%) which confirms the accuracy of the CFD-DEM model based on the modified $\mu_{r,pp}$ and $\mu_{s,pp}$ values.

Table 4.8: Verification of calibrated CFD-DEM model based on the AoR for different amount of quartz sand.

Diameter of neck (mm)	Mass of sand (g)	AoR (degree) Experimental	AoR (degree) CFD-DEM	Percent error (%)
5	25	41.6	41.6	0.5
	50	41.6	41.6	0.7
	75	41.6	41.6	1.2
8	25	38.8	38.9	3.8
	50	39.8	39.8	1.5
	75	39.8	39.8	4.0

Table 4.9: Verification of calibrated CFD-DEM model according to the discharging time for different amount of quartz sand.

Diameter of neck (mm)	Mass of sand (g)	Discharging time (sec) Experimental	CFD-DEM	Percent error (%)
5	25	6.6	6.7	1.5
	50	16.2	15.9	3.1
	75	25.3	25.1	0.8
8	25	2.6	2.50	3.8
	50	4.9	4.7	4.1
	75	7.3	7.0	5.5

4.4.5 Modelling the rectangular container

Investigating the effects of the domain size on the macroscopic properties of materials is an interesting subject and it was studied in this part. A rectangular container with the same geometry of the experimental set-up was used to assess the effect of interaction between particles and boundaries on the AoR. The distance between the adjustable walls was changed from 4 to 32 times of the particle diameter. Depending on the container width, it was filled with the various amounts of sand particles with the granulometry presented in Table 4.1. A comparison between the AoR of the experimental data and DEM results for various widths of container and two different boundary conditions of the DEM model is shown in Table 4.10.

Table 4.10: Comparison between the AoR of DEM simulation and experimental results (PSD based on Table 4.2 for quartz sand).

	Experiments	Periodic B.C.		Wall B.C.	
W/D_p	AoR (degree)	AoR (degree)	Computational time (sec)	AoR (degree)	Computational time (sec)
4	N.A.	35.9	1928	41.6	1698
6	41.0	35.6	4695	39.2	2681
8	40.5	35.3	9873	38.2	8206
12	38.5	35.2	17929	36.8	20217
24	36.5	35.1	35880	36.2	27592
32	35.1	35.2	37558	35.6	29624

Table 4.10 shows that the AoR gradually moves toward a constant value, while the distance between the adjustable walls is about 24 times of the particle diameter. The AoR gets constant at the $W/D_p = 32$ which means the wall boundary does not have any influence on the AoR at this value. as a result, the critical ratio of W/D_p was determined equal to 32 for cases that the wall boundary condition was employed in DEM simulation.

On the other hand, when the front and rear wall boundary conditions of container were replaced by the periodic boundary condition in DEM simulations, the results

indicated that the AoR was approximately same for all ratios of W/D_p. In such cases, the critical ratio of W/D_p will be 4, which indicates a significant decrease in the number of particles inside DEM domain.

A comparison between the computational speed of those types of boundary conditions (wall b.c. and periodic b.c.) indicated that at the same W/D_p, the periodic boundary condition is computationally more expensive than the fixed wall boundary condition. Indeed, the time that it takes the particles to get stable in the DEM simulation when the boundary condition is periodic is much longer than the time with the wall boundary condition. On the other hand, a similar AoR is obtained in $W/D_p = 4$ for periodic boundary condition while this value is achievable in $W/D_p = 32$ for the wall boundary condition. It is seen that the simulations with the periodic boundary condition are at least 15 times faster than the simulations with the wall boundary condition.

4.5 Conclusions

The objective of this chapter was evaluating the CFD-DEM model for a dense regime of particle flow. Also, a series of experiments and simulations were performed to determine the microscopic and macroscopic properties of quartz sand. The results of this chapter are concluded as follows.

1. The experimental results indicated that the AoR and discharging time in the hourglass test with 25 g of sand and neck diameter of 5 mm are 41.6° and 6.6 s, respectively. Also, it was observed that the experimental uncertainty of the AoR and discharging time is $\pm 1.1°$ and $\pm 0.1\, sec$, respectively.

2. The DEM was employed to determine the $\mu_{r,pp}$ and $\mu_{s,pp}$ between the sand particles without considering the effect of air on the macroscopic properties. The simulation results indicated that the DEM results will be equal to the experimental results in the cases that the $\mu_{r,pp}$ and $\mu_{s,pp}$ are equal to 0.30 and 0.52 in the DEM model.

3. The hourglass was also modelled with CFD-DEM in a way that the effect of air on the macroscopic properties was considered. It was observed that the $\mu_{r,pp}$ and $\mu_{s,pp}$ of 0.30 and 0.49 will lead to the experimental values of the AoR and discharging time.

4. It is possible to use a slice of the whole domain with the width (W) of 32 times the particle diameter (D_p) in the DEM simulation where the wall boundary condition is applied on the front and rare walls of the rectangular container. Moreover, the computational time can be reduced through employing the periodic boundary condition with the W/D_p of 4 in the DEM simulation.

5. It was concluded that the CFD-DEM model with its sub-models and parameters are also applicable in modelling a dense regime of particle flow when the rate of momentum exchange is hardly high between the particle and fluid phase.

Bibliography

[1] S. M. Derakhshani, D. L. Schott, and G. Lodewijks, "Micro-macro properties of quartz sand: Experimental investigation and DEM simulation," *Powder Technology*, vol. 269, pp. 127–138, jan 2015.

[2] S. Boggs, *Principles of Sedimentology and Stratigraphy*. Pearson Prentice Hall, 2006.

[3] M. G. Kleinhans, H. Markies, S. J. de Vet, A. C. in 't Veld, and F. N. Postema, "Static and dynamic angles of repose in loose granular materials under reduced gravity," *Journal of Geophysical Research*, vol. 116, no. E11, p. E11004, nov 2011.

[4] G. A. Anderson and C. J. Bern, "Dynamic Angle of Repose of Corncobs Placed by Three Mechanical Means," *Transactions of the ASAE*, vol. 27, no. 3, pp. 935–936, 1984.

[5] A. Mersmann, *Crystallization Technology Handbook*. CRC Press, 2001.

[6] D. Geldart, E. Abdullah, A. Hassanpour, L. Nwoke, and I. Wouters, "Characterization of powder flowability using measurement of angle of repose," *China Particuology*, vol. 4, no. 3-4, pp. 104–107, jul 2006.

[7] K. Ileleji and B. Zhou, "The angle of repose of bulk corn stover particles," *Powder Technology*, vol. 187, no. 2, pp. 110–118, oct 2008.

[8] O. D. Neikov, D. V. Lotsko, and S. Ipms, "SECTION 1 Powder Characterization and Testing," 2009.

[9] M. Rafiq Islam, A. B. Chhetri, and M. M. Khan, *Greening of Petroleum Operations: The Science of Sustainable Energy Production*. Hoboken, NJ:John Wiley & Sons, 2010.

[10] J. R. Taylor, *An Introduction to Error Analysis: The Study of Uncertainties in Physical Measurements*, ser. A series of books in physics. University Science Books, 1997.

[11] N. C. Barford, *Experimental measurements: precision, error and truth*. Addison Wesley Pub. Co., 1967.

[12] Y. Grasselli and H. J. H. Herrmann, "On the angles of dry granular heaps," *Physica A: Statistical Mechanics and its Applications*, vol. 246, no. 3-4, pp. 301–312, dec 1997.

[13] Y. Wang, Z. Zou, H. Li, and Q. Zhu, "A new drag model for TFM simulation of gas-solid bubbling fluidized beds with Geldart-B particles," *Particuology*, sep 2013.

[14] C. Kloss, C. Goniva, A. Hager, S. Amberger, and S. Pirker, "Models, algorithms and validation for opensource DEM and CFD-DEM," *Progress in Computational Fluid Dynamics*, vol. 12, no. 2-3, pp. 140–152, 2012.

[15] C. Wensrich and A. Katterfeld, "Rolling friction as a technique for modelling particle shape in DEM," *Powder Technology*, vol. 217, pp. 409–417, feb 2012.

[16] S. M. Derakhshani, D. L. Schott, and G. Lodewijks, "Reducing computational time by adjusting domain frame for fine granular materials with Discrete Element Method," in *Bulksolids Europe*, vol. 179, no. 3, Berlin, Germany, 2012, pp. 0–7.

Chapter

5

Modelling a Fluidized Bed of Quartz Sand

The coefficients of rolling and sliding friction ($\mu_{r,pp}$, $\mu_{s,pp}$) of the dried quartz sand were determined in Chapter 4. In addition, different DEM boundary conditions were compared through modelling the rectangular container. Also, the possibility of utilizing a fraction of the domain instead of whole domain was investigated. Finally, it was concluded that the CFD-DEM model is reliable for modelling a dense regime of particle flow when the rate of momentum exchange is hardly high between the particle and fluid phase.

The particle-fluid flow in the fluidized bed is likely similar to the particle-fluid flow at the transfer point of conveyors from the viewpoint of the particle-fluid flow regime and the number of particles that are involved in both cases. Hence, the validated CFD-DEM model of Chapter 4 is re-evaluated through modelling a dense regime of particle flow inside a fluidized bed in this chapter. The airflow has an initial speed in the fluidized bed which increases the rate of momentum exchange between the particle and fluid phases compared to case studies of previous chapters. The effect of CFD cell size, drag force model, particle size distribution, coefficients of friction between wall and particles, the DEM boundary condition, and the Coefficient of Restitution (CoR) on the accuracy of the simulation results are studied in this chapter.

In section 5.1 the theoretical background of the fluidized bed will be discussed briefly. The benchmarking test together with the properties of quartz sand and the geometry of the experimental set-up will be described in section 5.2. The results of the

conducted experiments will be presented in section 5.3 to determine the macroscopic properties of fluidized bed such as the Minimum Fluidization Velocity (Minimum Fluidization Velocity (MFV)) and pressure drop across the bed. At the end, the fluidized bed set-up will be simulated with the CFD-DEM model in section 5.4.

5.1 Basic principles of a fluidized bed

A fluidized bed is formed of a quantity of solid material that are placed within a container and it represents fluid-like properties when the upward flow passed up through the solid material [1]. In this section the macroscopic parameters that are usually used in this field of research are explained and then the different flow regimes within a fluidized bed are introduced.

5.1.1 Macroscopic parameters

The behaviour of a fluidized bed on the macroscopic level is described by a number of parameters like the Minimum Fluidization Velocity (MFV), bed pressure drop through a packed bed, the void fraction of the bed, and the height of the bed [2].

Minimum Fluidization Velocity (u_{mf})

A cylindrical column or another type of vessel that is filled with a packed material is called a fixed or packed bed [3]. To move from a packed bed to a fluidized bed state, it is necessary to continually increase the air velocity until the velocity reaches where the particles are suspended by the fluid flow, which is known as the Minimum Fluidization Velocity (MFV), u_{mf}.

It is seen in Figure 5.1 that at the point 'A' close to the MFV, the pressure within the fluidized bed drops and with increasing the airflow the pressure drop continues until point 'B' [3]. At this point, the flow regime will change to one of the six flow regimes that will be explained in section 5.1.2.

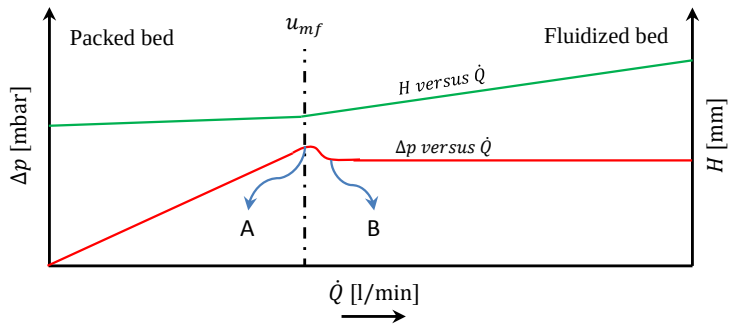

Figure 5.1: The pressure drop inside a fluidized bed vessel as a function of the airflow.

At this velocity (MFV), the bed will be in a state of quasi equilibrium so that the weight of particles inside the bed is equal to the drag and buoyancy forces. Beyond

the MFV, the particle bed will be suspended by the fluid flow and a further increase in the fluid velocity does not have a significant effect on the pressure drop, owing to sufficient percolation of the fluid flow. Therefore, the pressure drop for $\mathbf{u}_f > \mathbf{u}_{mf}$ is relatively constant.

Bed pressure drop (Δp)

When a fluid passes through a packed bed, the pressure drop that is caused by the friction between the particles and the fluid flow is approximately proportional to the fluid's superficial velocity, $\boldsymbol{u}_{fp} = (\mathbf{u}_f - \mathbf{u}_p)$. By increasing the velocity of the fluid, the hydrodynamic drag force will increase inside the packed bed and it can exceed to the weight of particles. At this point (point A), the particles will move up with the fluid flow and the bed starts to expand. Due to the expansion of the bed, the interstitial air velocity decreases which leads to reduction of the drag force (point B). In the air velocities beyond the MFV, the pressure drop gets constant and it is equal to the weight of the bed [4].

The pressure drop in the fluidized bed can be determined based on height of the bed H, particle diameter D_p, fluid void fraction of the bed ε_f, fluid viscosity μ_f, and the superficial velocity $\boldsymbol{u}_{fp}$, that was explained in section 2.3.2. Also, the required pressure drop for the MFV can be determined by the following equation:

$$\Delta p_{mf} = H(\rho_p - \rho_f)(1 - \varepsilon_{mf})g \tag{5.1}$$

Where the ε_{mf} is the void fraction of the bed at the MFV. The MFV can be calculated by substitution of Δp_{mf} in Equation 2.30.

Height of the bed (H)

By increasing the velocity of fluid, the height of packed bed starts to increase. The height of the bed can be measured by experimental study or it can be determined by the following equation.

$$H = \frac{m_p}{A(1 - \varepsilon_f)\rho_p} \tag{5.2}$$

where m_p, A, and ε_f are the mass of particles, cross-sectional area of the bed, and the fluid void fraction inside the bed, respectively .

Void fraction of the fluidized bed (ε_f)

The void fraction depends upon the material, shape, and size of particles. The fluid void fraction of the bed (ε_f) is defined as the ratio between the occupied volume of fluid phase (V_f) over the total volume of bed (V_b).

$$V_b = A \times H \tag{5.3}$$

$$\varepsilon_f = \frac{V_f}{V_b} \tag{5.4}$$

The relation between the particle and fluid void fraction is as follows:

$$\varepsilon_p + \varepsilon_f = 1 \tag{5.5}$$

5.1.2 Flow regimes in the fluidized bed

The flow regime within a fluidized bed can be laminar, transient or turbulent flow depends on the particle Reynolds number. Different parameters that influence the flow regime inside a fluidized bed are the fluid velocity, the physical properties of particle and fluid phases, and the size of set-up [5].

By increasing the rate of the fluid flow within a bed, the fluidized bed can pass through seven different flow regimes [6]. Figure 5.2 shows seven flow regimes that can be seen inside a fluidized bed by increasing the fluid velocity.

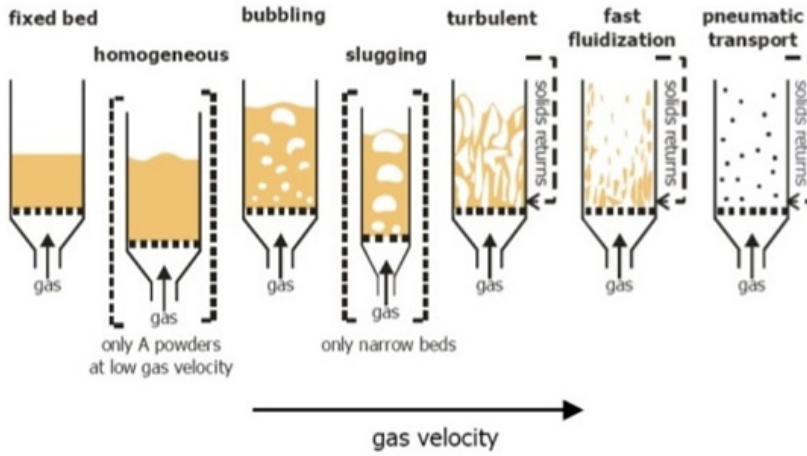

Figure 5.2: Seven types of fluid flow regime within a fluidized bed [7].

The case where the particles are not able to move inside the bed at the low velocities of the fluid is referred to the fixed bed regime. With increasing the fluid velocity beyond the MFV, the bed height will expand and particles start to move inside the vessel. This regime is called the homogeneous regime and it is usually seen for powders. The other possible regime is the bubbling regime that is seen by increasing the fluid velocity beyond the MFV. In small vessels, the slugging regime is seen when the velocity increases even more. In this regime, the size of bubbles are almost equal to the length of the vessel. As the fluid velocity increases even further, the turbulent, fast fluidization, and pneumatic transport will be seen respectively (see Figure 5.2).

As explained in section 2.3.2, the exerted drag force on a particle is calculated using the particle Reynolds number, Re_p (Equation 2.33). The flow regime within the fluidized bed vessel is determined based on the vessel Reynolds numbers Re_v,

which corresponding equation is [8]:

$$Re_v = \frac{\rho_f |u_f| D_h}{\mu_f} \tag{5.6}$$

Where D_h is the hydraulic diameter [8] and it is calculated as follows:

$$D_h = \frac{4A_v}{P_v} \tag{5.7}$$

In which, A_v and P_v are the area section of the vessel and the perimeter of vessel, respectively. The fluid flow regime inside the empty fluidized bed is laminar at $Re_v < 2300$, transient for $2300 \leq Re_v < 4000$, and turbulent for $Re_v \geq 4000$ [9]. The fluid flow regime inside the particle bed (around the particles) is considered as a laminar flow up to $Re_p = 10$ and it is a fully turbulent flow for $Re_p \geq 2000$ [8]. The fluid regime within the fluidized bed will be determined in section 5.2.4 based on these criteria and thereby, the appropriate laminar or turbulent models will be employed in the CFD model.

It was mentioned earlier that the sequence of the flow regime within a vessel depends on the various parameters such as particle size, particle and fluid densities, and the size of vessel. Geldart [5] did a series of experiments with the air fluidized bed under the ambient conditions and proposed four groups for classification of powders which is shown in Figure 5.3.

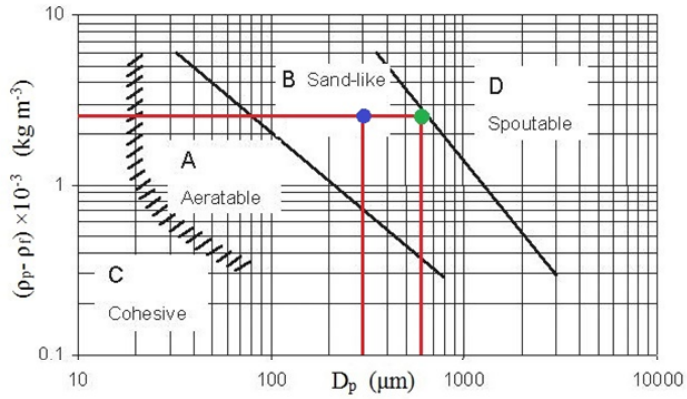

Figure 5.3: Geldart's classification of powders according to fluidization properties [5].

These four groups are introduced here:

Group A (Aeratable): The homogeneous regime is seen in this group at the fluid velocity a little beyond the MFV ($u_f > u_{mf}$). By increasing the fluid velocity, the bubbling regime will appear and this class of material tends to have a maximum size of bubbles.

Group B (Sand-like): The bubbles are formed directly after the MFV ($u_f = u_{mf}$) and the size of bubbles will increase with increasing the velocity of fluid.

Group C (Cohesive): In this group, the size of particles is very small and particles are cohesive so that the fluidization happens very rarely in this group. Channelling is the main problem that happens in the fluidization of these type of materials.

Group D (Spoutable): Big particles are categorized in this group of powders. If the fluid velocity gets greater than the MFV, the spout-fluidization regime is formed and particles are entered into the spouting motion.

The density of the quartz sand particles and air are 2650 and 1.2139 kg/m^3, respectively. Also, the minimum diameter of sand particles and the D_{50} of quartz sand, that is also the biggest size of sand particles, are respectively reported 0.3 mm and 0.6 mm in Table 4.1. The points with regard to these values are highlighted by the green and blue points in Figure 5.3. As seen, the fluidization in this study should be similar to the reported properties of Group B.

5.2 Benchmarking test

In this section, the experimental set-up and its components are illustrated. The measurement methodology and the parameters that will be used in simulations together with the numerical settings of the model are briefly introduced in this section.

5.2.1 Experimental setup

Figures 5.4 and 5.5 illustrate the fluidized bed set-up and the schematic layout of the experimental set-up. Airflow is pressurized by a compressor (1) up to 8 bar and then it relieves to 4 bar with a hand regulator (2) which guaranty the proper operation of the flow regulator (3). A PI controller (4) measures and controls the airflow in conjunction with the flow regulator.

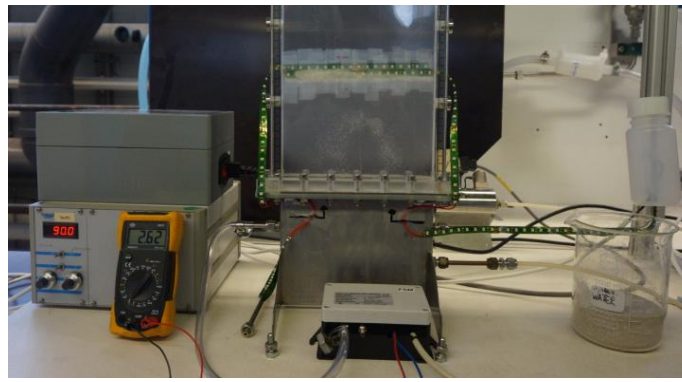

Figure 5.4: A picture of the experimental fluidization set-up together with its components.

The volumetric airflow rate is adjustable in the range of 0-100 l/min with an accuracy of 0.5%. The airflow enters into the rectangular fluidization vessel (8) which is composed of a distributor (5) where the airflow enters into the set-up. The airflow then goes through a fine screen (6) into the bottom of the bed (7). A pressure transducer (9) is used to measure the pressure inside the transducer in the range of 0-200 $mbar$ by a digital multi meter (10) with accuracy of 1 decimal place.

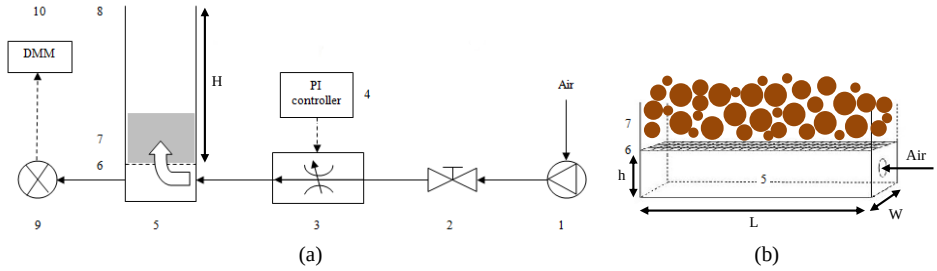

Figure 5.5: Schematic layout of the fluidized bed: a) the experimental set-up b) the vessel distributor in accordance with Table 5.1.

The geometric specification of the fluidization vessel is presented Table 5.1.

Table 5.1: The geometric size of the fluidized bed vessel.

L (mm)	W (mm)	H (mm)	h (mm)	Wall material
200	15	350	20	Plexiglass

The fluidized vessel is filled with quartz sand until different heights of 100, 150, 200, and 250 mm. It is possible to have the same height of sand with a different amount of sand due to consolidation. Hence, the weight of sand is measured at all height of sand and the vessels are filled according to the same weight of sand in similar experiments. On the other hand, the fluid velocity is set to the upper bound of the fluid volumetric flow for 1 minute and then it reduces very slowly to the lower bound of air flow to minimize the effect of consolidation effect between the sand particles.

The experiments are filmed with a Sony Alpha ILCE-5000 camera which is set to 50 frames per second with video resolution of 1920×1080. The measuring tape is on both sides of the vessel with the scale of 1 mm to measure the height of sand inside the fluidized bed set-up.

5.2.2 Measurement methodology

Variables that are measured in an experiment can be divided into three types of values: the independent values which are considered as the input parameters of the experiment, the dependent values that are measured during the experiment, and the

derived values which are extracted from the other experimental values. Table 5.2 shows an overview of these three types of experimental variables.

Table 5.2: Three types of experimental variables.

Input values	Measured values	Derived values
Fluid volumetric flow rate ($\dot{Q}$)	Pressure drop (Δp)	Fluid velocity (u_f)
		Bed void fraction (ε_f)
	Bed height (H)	Minimum fluidization velocity (u_{mf})

When the velocity of the air increases, a lot of fluctuations will be observed during the measurement of pressure and height of the bed. Hence, the experimental results are recorded for 10 seconds and the average values of this period are reported in this study [6]. According to Table 5.2, the pressure drop (Δp) is an independent value that is accurately measured with the pressure transducer. Accordingly, the pressure drop is considered as the reference value in modelling the fluidized bed set-up in this study.

5.2.3 Experimental plan

All experiments are performed according to the procedure that was explained earlier and each experiment is repeated three times since a high consistency of the measurement was observed by this number of repetitions [6]. The additional information regards to the experimental data are provided in Appendix A. The increment step of the airflow rate is considered as 5 l/min because the trend of moving from the packed bed toward the fluidized bed can be captured by this step. An overview of the experimental plan is shown in Table 5.3.

Table 5.3: Experimental plan for different height of the bed in the fluidized vessel.

Initial height of the bed (mm)	Volumetric flow rate of air	
	Variation range (l/min)	Increment interval (l/min)
Empty, 100, 150, 200, 250	0-100	5
Empty, 100, 150, 200, 250	100-0	5

5.2.4 Numerical settings of the CFD-DEM model

In the field of computational fluid dynamics choosing appropriate initial and boundary conditions is of great importance. In this study, a combination of Neumann and Dirichlet conditions [10] is used in the implementation of the pressure and velocity boundary conditions together with the no-slip wall boundary condition at the walls of vessel. Tables 5.4 shows the parameters and the voidage model that are used in the CFD-DEM simulations.

Table 5.4: The settings of parameters and voidage model that are used in the CFD-DEM model.

Voidage model	Coupling interval	Δt_{DEM} (sec)	Δt_{CFD} (sec)	$\mu_{s,pp}$	$\mu_{r,pp}$
Divided	100	1.0e-6	1.0e-4	0.49	0.3

In addition, a number of parameters need to be determined and the drag force model should be re-evaluated for the fluidization phenomenon. The rolling friction between particles and wall is deactivated in the DEM model because the coefficient of rolling friction is one of the parameters that will be determined in this study.The variation range and the drag models that will be checked in this chapter are listed in Tables 5.5.

Table 5.5: The variation range of parameters that will be determined with the CFD-DEM model.

Wall B.C.	$x/\Delta x$	Force models	CoR	$\mu_{s,pw}$	$\mu_{r,pw}$
wall periodic	10, 20, 30 40, 50, 60	Di Felice Gidaspow Koch-Hill	0.1, 0.5, 0.9	determined	0.1, 0.2 0.3, 0.4

The maximum volumetric airflow rate inside the vessel that will be used in the simulations of this chapter is 80 l/min which is about 0.43 m/s. At this velocity, the particle and vessel Reynold numbers inside the fluidized bed set-up are $Re_p = 17$ and $Re_v = 808$, respectively. Therefore, the airflow within the vessel is a laminar flow and based on the particle Reynolds number the drag force is calculated and exerted on each particle (see section 2.3.2).

5.3 Experimental results

The experimental results of the fluidized bed are presented in this section.

5.3.1 Determining the Minimum Fluidization Velocity (MFV)

Figure 5.6 shows the consolidation effect on the pressure drop during increasing and decreasing the airflow rate. This effect disappears beyond the MFV because the materials are mixed in the high flow rate of air.

The variation of the pressure drop and the bed height inside the fluidized bed was measured at the different height of the bed: 100, 150, 200, and 250 mm. The measurement was performed for both processes of increasing and decreasing the air velocity within the vessel that is illustrated in Figure 5.6.

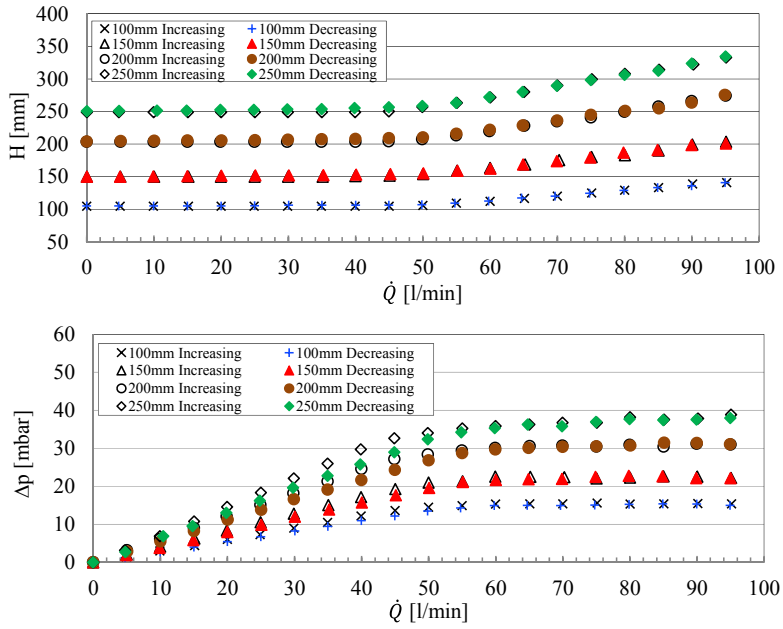

Figure 5.6: The variation of the bed height and the pressure drop within the fluidization bed versus the volumetric flow rate of air.

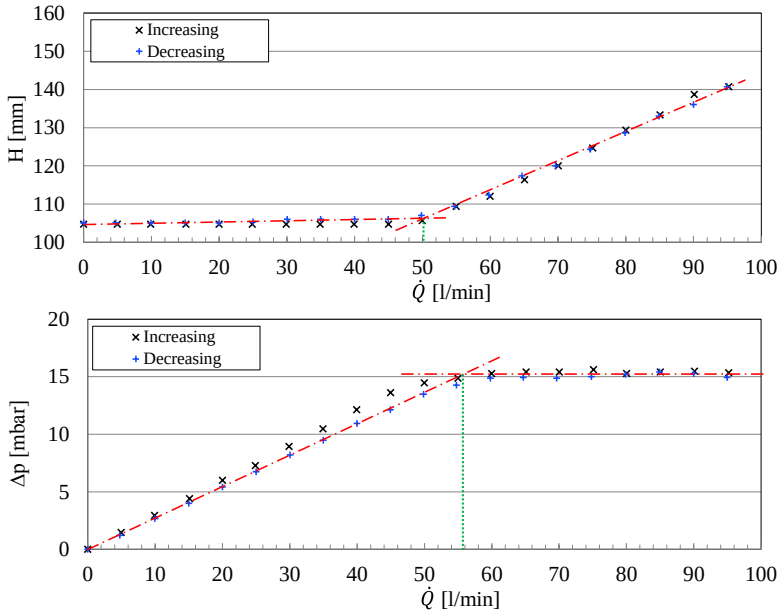

Figure 5.7: Determination of the MFV: top) the intersection of the fitted lines over the bed height and the volumetric flow rate: bottom) the intersection of the fitted lines over the pressure drop and the volumetric flow rate.

As explained in the previous section, the air velocity at the point where the height of bed starts to increase or the pressure drop gets constant is the MFV of the set-up. The MFV can be extracted through the intersection of the fitted horizontal and diagonal line over $H - \dot{Q}$ or $\Delta p - \dot{Q}$ graphs. The MFV obtained by these two methods is shown in Figure 5.7 for a bed height of 100 mm.

In Table 5.2 was shown that the pressure drop and the bed height are two measured values which can be used in the determination of the MFV. As seen in Figure 5.7, the MFV obtained form $H - \dot{Q}$ or $\Delta p - \dot{Q}$ graphs are about 50 l/min and 56 l/min, respectively. The MFV that was determined from the pressure drop and the bed height graphs for the other heights of the bed are presented in Table 5.6.

Table 5.6: A comparison between the MFV derived by pressure drop and bed height.

Initial bed height (mm)	u_{mf} (l/min)	
	Pressure drop	Bed height
100	56.0	50.0
150	55.1	49.8
200	55.0	50.2
250	55.0	49.9

It was indicated that the MFV at different height of sand has an identical value which confirms with the theory of fluidization. On the other side, the measured pressure drops are more reliable than the measured bed height because a pressure transducer was employed in the measurement of pressure drop. Accordingly, the results of the pressure drop is considered as a reference value in this study.

5.3.2 The flow regime of fluidized bed

Figure 5.8 illustrates the bubble shape inside the fluidized bed for different height of sand (100, 150, 200, and 250 mm). As seen, the bubbling flow regime is the dominant regime of particle flow inside the fluidized bed at $\dot{Q} = 80\, l/min$ for all height of the bed. The experimental results indicated that the shape of bubbles are two-dimensional in the y-direction at all height of the bed at $\dot{Q} = 80\, l/min$. The same results was also observed at the other rates of airflow.

5.3.3 The coefficient of sliding friction between the sand and the Plexiglass wall

The sliding angle measured in the laboratory was 17.6°, consequently $\mu_{s,pw}$ is equal to $tan\, 17.6° = 0.32$ [11]. This parameter will be utilized in section 5.4.6 to determine $\mu_{r,pw}$.

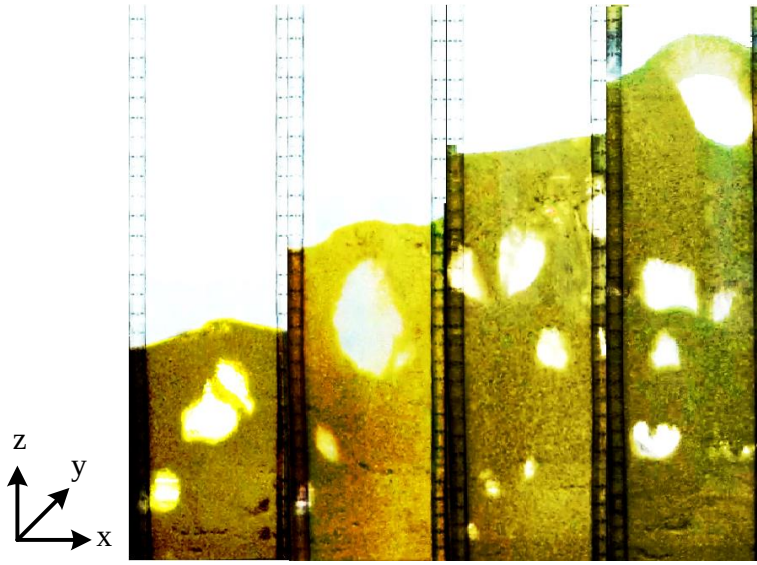

Figure 5.8: Experimental shape of sand bubble inside the fluidized bed at different initial height of sand (100, 150, 200, and 250 mm) at $\dot{Q} = 80\,l/min$.

5.4 CFD-DEM results

In this section, the validated model of the previous chapter is re-evaluated through comparing the simulation results with experimental data.

5.4.1 Grid dependency analysis

It has been reported in previous studies that the airflow can be considered as two-dimensional in the CFD simulations in the cases that the bed length is larger than its width ($L > 5W$) [12, 13]. In this study, the bed length is about 13 times the bed width and it can be assumed that a fluid flow is two-dimensional inside the fluidized bed vessel.

The experimental pressure drop at the airflow rate of $30\,l/min$ is equal to $8.2\,mbar$ with the uncertainty of $\pm 0.3\,mbar$ [6]. This airflow rate was used to evaluate the effect of CFD cell size on the accuracy of CFD simulation. For this purpose, a uniform CFD grid was used in the x and z directions and then the grid dependency analysis was conducted to determine the optimum number of CFD cells in the x and z directions. Table 5.7 shows the size and number of CFD cells in the CFD domain.

Table 5.7: Determination of the optimum size of the CFD cells in the CFD domain at $\dot{Q}$=30 l/min.

ID	$\Delta x = \Delta z\,(mm)$	$D_p/\Delta x$	$N_x \times N_y \times N_z$	Pressure drop $(mbar)$
1	20.0	0.03	$10 \times 1 \times 18$	5.12
2	10.0	0.06	$20 \times 1 \times 35$	6.72
3	6.7	0.09	$30 \times 1 \times 52$	7.51
4	5.0	0.12	$40 \times 1 \times 70$	8.10
5	4.0	0.15	$50 \times 1 \times 88$	8.15
6	3.3	0.18	$60 \times 1 \times 106$	8.16

As seen in Table 5.7, there is hardly any difference between the pressure drop of all three last cases (ID: 4, 5, and 6) which means $D_p/\Delta x = 0.12$ is the optimum case and utilization of the fine CFD grid does not have any effect on the accuracy of the results. Figure 5.9 shows that the obtained results of cases 4, 5, and 6 are in a good agreement with the experimental results while the computational effort of case 4 is less than the other two cases. Accordingly, the CFD grid size of case 4 will be employed in the subsequent simulations of the fluidized bed.

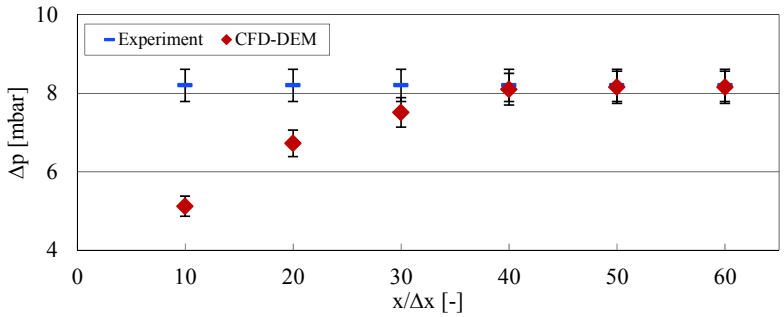

Figure 5.9: Grid dependency analysis with the uniform grids in the x and z direction.

The number of CFD cells in the y-direction was changed in case 4 from $N_y = 1$ to $N_y = 5$ to check the effect of utilization of three-dimensional grid on the accuracy of the CFD-DEM results. The simulation results indicated that the pressure drop is 8.10 and 8.12 $mbar$ for $N_y = 1$ and $N_y = 5$, respectively. Consequently, utilization of two-dimensional CFD grid is a reasonable and realistic assumption and case 4 represents the optimum number of the CFD grid and will be employed in the next simulations of this study.

5.4.2 The penetration effect

The amount of pressure drop is not identical for the same airflow rate during the increasing and decreasing the rate of airflow inside a fluidized bed. The main reason that the pressure drop in the increasing process is slightly higher than the decreasing process is because of the penetration of the sand particles during the filling process.

The void fraction between particles decreases because of penetration so that the pressure drop increases during the increasing process. Figure 5.10 illustrates the difference between the pressure drop in the increasing and decreasing processes at different volumetric flow rate of air in the fluidized vessel. The vessel is filled with the Poly-Sized Particles (PSP) until the bed height of 100 mm and the boundary conditions of the CFD and DEM models were set to the wall boundary condition.

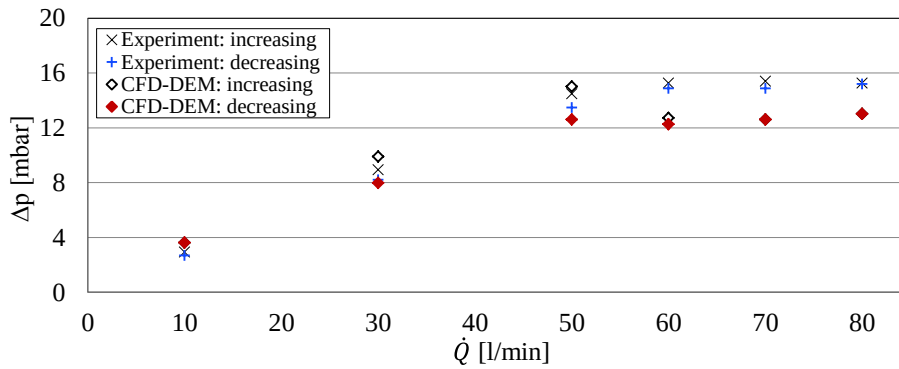

Figure 5.10: The variation of the pressure drop versus volume airflow rate during.

This phenomenon was also seen in the CFD-DEM modelling of the fluidized bed for different airflow rate. Hence, the pressure drop of the decreasing process is used in this study to calibrate the CFD-DEM model and to avoid the effect of material penetration during the parametric study.

5.4.3 Drag force models

The accuracy of three well-known drag force models, namely, Di Felice, Gidaspow, and Koch-Hill drag models, were evaluated in Section 3.3.1 for a dilute regime of particle flow. Also, it was observed in 4.4.4 that the Gidaspow drag force is an accurate and reliable drag model for modelling the dense regime of particle flow. In this section, the accuracy and reliability of the Gidaspow drag model was re-evaluated for a fixed bed and bubbling regime at the airflow rates of 30 l/min (before the MFV) and 80 l/min (beyond the MFV) where the rate of momentum exchange between the fluid and particle phases is significant.

The fluidized bed was filled until the bed height of 100 mm with the PSP and the wall boundary condition was implemented in the CFD and DEM models. Also, the coefficients of friction between the walls and particles was set to zero. The simulation results are presented in Table 5.8 for two different states of the fluidized bed.

Table 5.8: The prediction of the pressure drop at the airflow rates of 30 l/min and 80 l/min by different drag force models.

	Experiments		Drag force model					
			Di Felice		Gidaspow		Koch-Hill	
Air flow (l/min)	30	80	30	80	30	80	30	80
Pressure drop ($mbar$)	8.2	15.2	9.3	13.6	8.0	13.8	9.9	13.8
Percent error(%)	N.A.	N.A.	-13.4	10.5	2.4	9.2	-20.7	9.2

As seen in Table 5.8, all drag models predicted a pressure drop less than the experimental value because the coefficient of rolling friction between particles and wall is deactivated in the DEM model. On the other side, the Gidaspow model predicted the pressure drop with the percent error of 2.4% at 30 l/min while the predicted pressure drops based on the Di Felice and Koch-Hill models were bigger than the experimental value with the percent errors of -13.4% and -20.7%, respectively.

With regard to points raised, it was concluded that the Gidaspow model is a reliable drag force model for situations before and after the MFV and will be employed in the subsequent simulations of this study.

5.4.4 The effect of particle size

A number of researches [12–18] used Mono-Sized Particles (MSP) instead of considering the granulometry of particles in modelling the fluidized bed. In this part, a comparison was conducted to determine the effect of utilizing the MSP in the simulation on the pressure drop and the other macroscopic properties of the fluidized bed.

Figure 5.11 shows the variation of the pressure drop based on the airflow rate in the vessel which was filled by the MSP and PSP. The granulometry of sand particles in the PSP case is according to Table 4.1.

The MFV of MSP and PSP was determined equal to 50 l/min and 60 l/min, respectively. The difference between the MFV is interpreted by the fact that the size of voids between particles in the MSP case is more than the PSP case so that the pressure drop in the MSP case would be less than the PSP case. Also, the pressure drop of both cases decreases slightly after the MFV point which is in agreement with the theory of the fluidization.

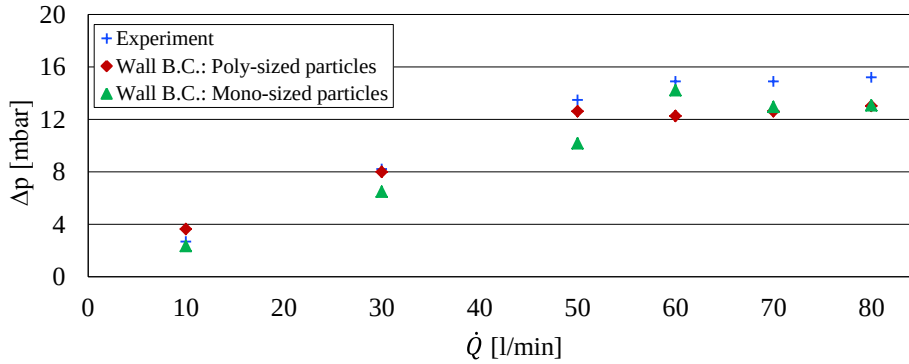

Figure 5.11: The effect of utilization of MSP or PSP on the determined pressure drop in the vessel

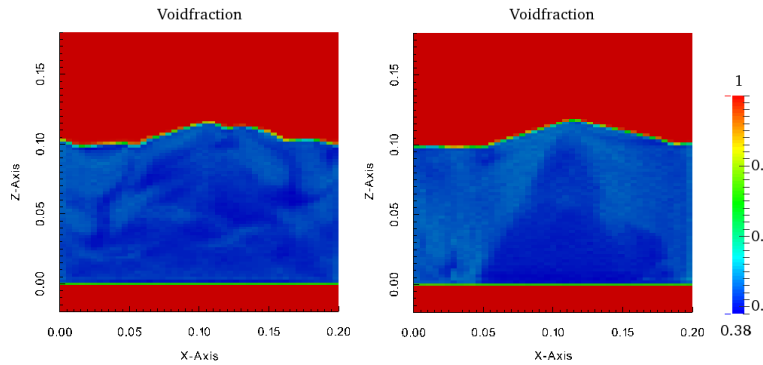

(a) The void fraction distribution within vessel

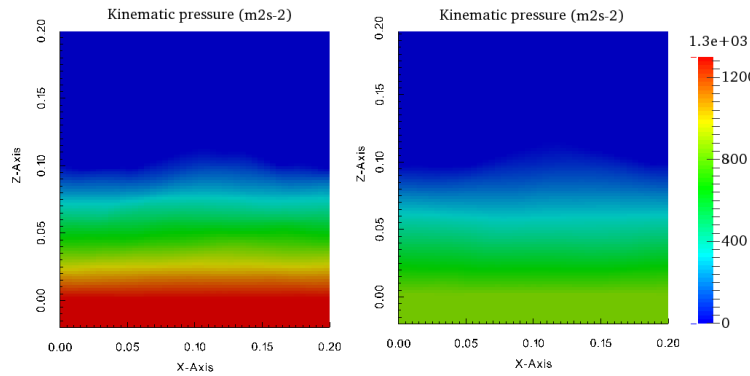

(b) The domain of pressure drop within vessel

Figure 5.12: A comparison between the simulation results at $\dot{Q}$=50 l/min. left: PSP, right: MSP.

The contours of void fraction and pressure drop within the fluidized bed for the

MSP and PSP cases are shown in Figure 5.12. It is seen that there is not any bubble in both cases while the pressure drop within PSP case is significantly larger than the MSP case.

Figure 5.13 shows that the velocity of particles in the MSP case is almost zero while the velocity of particles in the PSP is considerable which indicates particles are very close to the experimental MFV, $55\,l/min$.

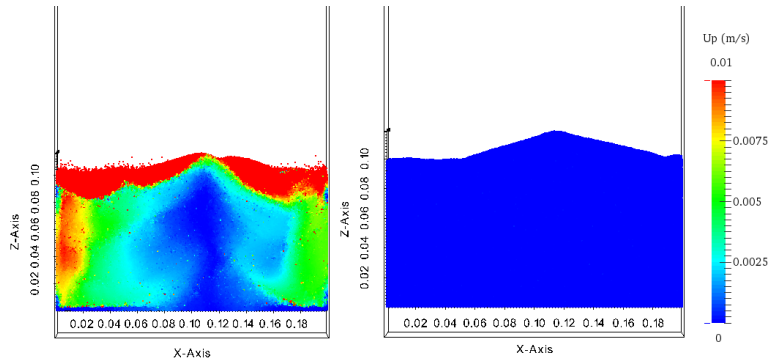

Figure 5.13: A comparison between the velocity of particles in PSP and MSP cases at $\dot{Q} = 50\,l/min$. This figure was extracted from the DEM results.

The other important factor that was considered in evaluating the effect of material granulometry was the bubble shape at airflow rates beyond the MFV. Figure 5.14 shows a comparison between the experimental result and the CFD-DEM results for the vessel filled with the PSP and MSP.

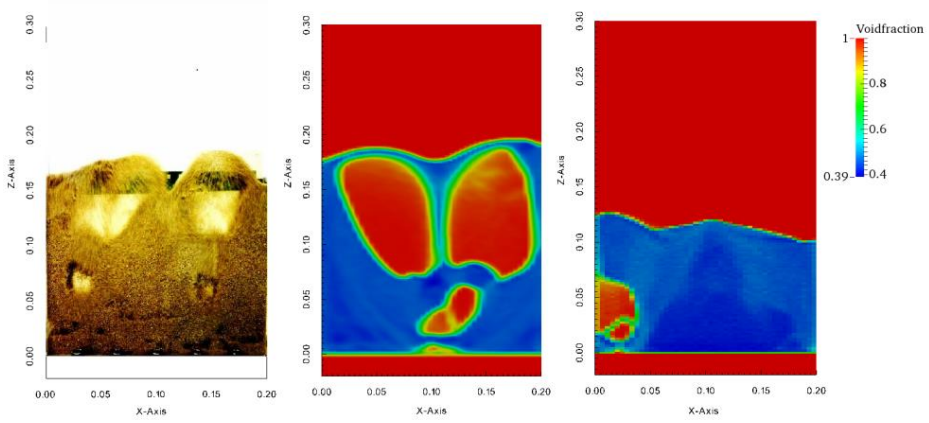

Figure 5.14: The effect of particle granulometry on the shape and size of bubbles within fluidized bed at $\dot{Q} = 80\ l/min$. Left: experiments, centre: PSP, right: MSP.

As seen in the experimental results, a number of bubbles with a various size formed at the airflow rate of 80 l/min. The CFD-DEM results show that the result

of PSP case is qualitatively similar to the experimental result while only one bubble formed in MSP case during the simulation time.

As a result, utilization of MSP materials instead of PSP materials in the fluidized bed simulations can lead to different quantitative and qualitative results. In this study, the granulometry of particles is considered in modelling the fluidized bed.

5.4.5 Periodic and wall boundary conditions

The Periodic Boundary Condition (PBC) was already employed with a number of researchers [12, 19, 20] instead of Wall Boundary Condition (WBC) to reduce the computational time of DEM simulations. In this study, the experimental results illustrated that the front and back walls do not have a considerable effect on the shape of bubble inside the fluidized bed (see Figure 5.8). Hence, it immediately comes to mind that the computational time of the DEM-CFD simulations can be reduced by utilizing a fraction of the vessel width to reduce the number of particles in DEM simulation.

In Chapter 4 was concluded that the computational time of DEM simulation can be reduced through replacing the WBC with PBC so that the width of domain reduces up to $W/D_p = 4$. In this study, the $W/D_p = 6$ was used to have more particles in the y-direction where the PBC was implemented instead of the front and back walls. The variation of pressure drop versus the rate of airflow for both DEM boundary conditions is presented in Table 5.9.

Table 5.9: The influence of DEM boundary condition on the accuracy of CFD-DEM results.

		Wall B.C.		Periodic B.C.	
$\dot{Q}$	Δp_{exp}	Δp	Percent	Δp	Percent
(l/min)	$(mbar)$	$(mbar)$	error (%)	$(mbar)$	error (%)
10	2.7	3.6	-35.6	3.2	-21.1
30	8.2	8.0	2.7	8.1	1.0
50	13.5	12.6	6.4	14.4	6.9
60	14.9	12.2	17.6	12.9	13.2
70	14.9	12.6	15.2	13.2	11.5
80	15.2	13.0	14.5	13.4	11.8

As seen, the results of PBC are closer to the experimental data (Δp_{exp}) than the results of WBC. It can be due to the deactivation of the coefficient of rolling friction in WBC so that there is not any rolling force between particles and walls which decreases the pressure drop in WBC. The other reason can be that the void fraction in WBC close to the walls is slightly bigger than the other places in the domain while with PBC this effect is not present. This effect decreases the fluid void fraction in the CFD cells adjacent to PBC compared to the CFD cells close to the wall in WBC. Accordingly, the average pressure drop with PBC is slightly more than WBC in the fluidized simulations.

The other limitation of PBC is related to the impossibility of adjusting the coefficients of friction in the periodic boundaries. This is of importance in the cases that considering the wall effect in the simulation is unavoidable. Hence, the effect of PBC on the simulation results should be carefully determined in each case study. In this study, the WBC were utilized in all simulations and in the next section, the coefficients of friction will be activated in the DEM model to study the wall effect on the simulation results.

5.4.6 Particle-wall friction coefficient

The coefficients of friction between the sand particles were determined equal to $\mu_{r,pp} = 0.3$ and $\mu_{s,pp} = 0.49$ in Chapter 4. Also, the coefficient of sliding friction between the sand particles and Plexiglass wall, $\mu_{s,pw} = 0.32$, was experimentally measured in section 5.3.3. In this part, the coefficient of rolling friction between particles and domain was activated in the DEM model and $\mu_{r,pw}$ were determined through the numerical technique.

For this purpose, five sets of $\mu_{r,pw}$ were chosen to be used in the DEM simulation. Table 5.10 shows the variation of $\mu_{r,pw}$ and $\mu_{s,pw}$ between the sand particles and wall and its significant effect on the pressure drop at the airflow rate of 80 l/min. The experimental uncertainty of the measured pressure drop (15.2 $mbar$) at airflow rate of 80 l/min is $\pm 0.3\,mbar$ [6]. Accordingly, the CFD-DEM results that are in the range of $15.2 \pm 0.3\,mbar$ can be considered as reliable.

Table 5.10: Different sets of $\mu_{r,pw}$ and $\mu_{s,pw}$ between the sand particles and the Plexiglass wall at $\dot{Q} = 80\ l/min$.

ID	1	2	3	4
$\mu_{s,pw}$	0.32	0.32	0.32	0.32
$\mu_{r,pw}$	0.10	0.20	0.30	0.40
Δp (mbar)	16.26	15.74	15.36	16.4
Percent error (%)	-7.0	-3.6	-1.0	-8.2

As seen in Table 5.10, the accuracy of results improved when $\mu_{r,pw}$ increased from 0.10 to 0.30 and with a further increase in $\mu_{r,pw}$, the accuracy of the predicted pressure drop decreased. As a result, the accurate pressure drop can be determined with $\mu_{r,pw} = 0.30$ and $\mu_{s,pw} = 0.32$ at the airflow rate of 80 l/min with the percent error of -1.0%.

The influence of the particle-wall friction coefficients on the accuracy of the CFD-DEM simulation is shown in Figure 5.15 and the experimental error bars on the plot are equal to $\pm 0.3\,mbar$. The average value of the pressure drop was measures at different times of a simulation and it was indicated that the uncertainty of the simulation results is less than $\pm 0.1\,mbar$. Accordingly, it is concluded that the CFD-DEM results are accurate enough in the whole range of the airflow in accordance with the determined values for $\mu_{r,pw} = 0.3$ and $\mu_{s,pw} = 0.32$.

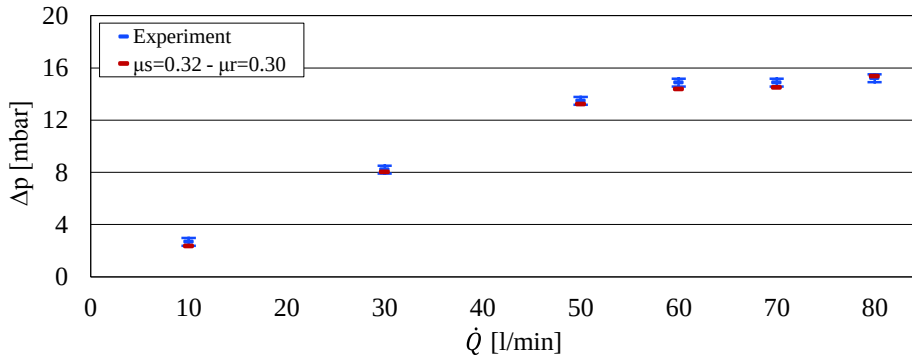

Figure 5.15: The variation of the pressure drop at different airflow rates according to $\mu_{r,pw} = 0.30$ and $\mu_{s,pw} = 0.32$.

5.4.7 Determining the Coefficient of Restitution

The other microscopic properties of particles is the Coefficient of Restitution (CoR) that should be determined for the quartz sand. Wang et al. [21] modelled a fluidized bed of quartz sand with the TFM method and they used CoR of 0.9 in the simulations. This value was also employed in Chapter 4 and the previous simulations of this chapter.

In this section, the CoR was determined through modelling the fluidized bed in the volumetric flow rate of 50 l/min for three sets of CoR between the sand particles. The CoR was changed in the range of 0.1, 0.5, and 0.9 and the pressure drop inside the fluidized bed was compared with the experimental results. Table 5.11 shows the variation of the pressure drop versus the CoR.

Table 5.11: The effect of the CoR (e) on the pressure drop in the fluidized bed set-up.

Case study	e	Δp $(mbar)$	Percent error (%)
Experiment	...	13.5	...
	0.10	12.9	4.3
CFD-DEM	0.50	13.0	3.4
	0.90	13.2	1.4

It is seen that the pressure drop increases with increasing CoR in the CFD-DEM model. It can be interpreted by the fact that for high values of CoR (elastic behaviour), the size of bubbles in case of formation is very small. The bubble formation can start as soon as the CoR is set to values below 1.0 which lead to creation of small bubbles within the vessel [22]. In this study, the pressure drop was measured at airflow rate of 50 l/min which is really close to the MFV and the particle bed is ready to move from the packed bed mode into the fluidization mode. Hence, any decrease in CoR will lead to formation of very tiny bubbles in the sand bed so that the fluid void fraction increases and the pressure drop decreases.

On the other side, the uncertainty of the experimental pressure drop is $\pm 0.3\,mbar$ [6] which represents a negligible effect of CoR on the pressure drop at airflow rate of 50 l/min. However, it was observed that the CoR of 0.9 has better agreement with the experimental results and also, it is in agreement with the proposed CoR by Wang [21] for quartz sand.

5.5 Conclusions

The fluidized bed set-up was experimentally and numerically studied in this chapter and the results of this study were concluded as follows:

1. Grid dependency analysis indicated that the uniform CFD cells smaller than $5\,mm$ do not have significant effect on the accuracy of CFD-DEM results. Hence, a dense regime of particle-fluid flow can be accurately modelled at the particle diameter to the CFD cell size ratio of $D_p/\Delta x = 0.12$. In addition, it was indicated that the two-dimensional CFD grid can be employed instead of three-dimensional grid in the CFD simulations.

2. It was observed that the Gidaspow drag force model is the reliable and accurate drag force model to be employed in modelling the fluidized bed of sand particles.

3. The sand particles were penetrated during the filling process of vessel with sand particles and this effect was observed in both experimental and CFD-DEM results. In this study, the airflow rate increased beyond the MFV and then it slowly reduced to zero in order to neutralize this effect. It was seen that the penetration has a significant effect before the MFV and its effect disappears for velocities beyond the MFV due to the mixing process.

4. It was seen that utilization of the MSP instead of the PSP in modelling the fluidized bed of sand will result the different values for the MFV. In addition, with the MSP, the shape and size of bubbles were not in agreement with the experimental results.

5. The coefficients of rolling and sliding friction between the Plexiglass wall and sand particles were numerically and experimentally determined and are equal to 0.30 and 0.32, respectively. Utilization of these values in the CFD-DEM model led to significant improvement in the accuracy of the determined pressure drop for all the values of airflow rate.

6. It was seen that the front and back walls of the fluidized bed can be replaced with the periodic boundary condition instead of the wall boundary condition in the DEM simulation to enhance the computational effort of the DEM model. However, the effect of PBC on the simulation results should be carefully determined in each case study.

7. Three sets of the CoR between the sand particles (0.1, 0.5, and 0.9) was simulated with at the airflow rate of 50 l/min. The results obtained with CoR = 0.9 are in good agreement with the experimental data with the percent error of 2.1%.

8. As a final result, it is concluded that the CFD-DEM model is successfully validated and its parameters and sub-models are correctly selected. Accordingly, it is

possible to employ the validated model of this chapter in simulating a dense regime of particle-fluid flow such as modelling the dust liberation at the transfer point of conveyors.

Bibliography

[1] J. Zhu, B. Leckner, Y. Cheng, and J. Grace, "Fluidized Beds," sep 2005, pp. 5–1–5–93.

[2] E. van Zessen, J. Tramper, A. Rinzema, and H. Beeftink, "Fluidized-bed and packed-bed characteristics of gel beads," *Chemical Engineering Journal*, vol. 115, no. 1-2, pp. 103–111, dec 2005.

[3] W. C. Yang, *Handbook of Fluidization and Fluid-Particle Systems*, ser. Chemical Industries. Taylor & Francis, 2003.

[4] E. Ortega-Rivas, *Unit Operations of Particulate Solids: Theory and Practice*. Taylor & Francis, 2011.

[5] D. Geldart, "Types of gas fluidization," *Powder Technology*, vol. 7, no. 5, pp. 285–292, may 1973.

[6] S. Kraijema, "Experimental Study on Fluidization Characteristics of an Air-Sand Bed inside a Rectangular Fluidized Bed," Delft University of Technology, Delft, Tech. Rep., 2014.

[7] J. Ruud van Ommen, "Flow Regimes in Fluidized Beds," Chemical Reaction Engineering Laboratory, Delft, Tech. Rep., 2003.

[8] M. Rhodes, *Introduction to Particle Technology*. Wiley, 2008.

[9] J. P. Holman, *Heat transfer*, ser. Mechanical engineering series. McGraw-Hill, 1989.

[10] A. H. Cheng and D. T. Cheng, "Heritage and early history of the boundary element method," *Engineering Analysis with Boundary Elements*, vol. 29, no. 3, pp. 268–302, mar 2005.

[11] P. Ashayer, *Application of Rigid Body Impact Mechanics and Discrete Element Modeling to Rockfall Simulation*, ser. Canadian theses. University of Toronto (Canada), 2007.

[12] Y. Feng and A. Yu, "Effect of Model Formulation of Discrete Particle Simulation on the Gas Fluidisation Behaviour," *Third International Conference on CFD in the Mineral*, 2003.

[13] C. R. Müller, S. A. Scott, D. J. Holland, B. C. Clarke, A. J. Sederman, J. S. Dennis, and L. F. Gladden, "Validation of a discrete element model using magnetic resonance measurements," *Particuology*, vol. 7, no. 4, pp. 297–306, aug 2009.

[14] T. Li, R. Garg, J. Galvin, and S. Pannala, "Open-source MFIX-DEM software for gas-solids flows: Part II Validation studies," *Powder Technology*, vol. 220, pp. 138–150, apr 2012.

[15] G. Bokkers, M. van Sint Annaland, M. Goldschmidt, O. Olaofe, M. van der Hoef, and J. Kuipers, "Development of a multi-fluid model for poly-disperse dense gas-solid fluidised beds, Part II: Segregation in binary particle mixtures," *Chemical Engineering Science*, vol. 64, no. 20, pp. 4237–4246, oct 2009.

[16] M. van Sint Annaland, G. Bokkers, M. Goldschmidt, O. Olaofe, M. van der Hoef, and J. Kuipers, "Development of a multi-fluid model for poly-disperse dense gas-solid fluidised beds, Part I: Model derivation and numerical implementation," *Chemical Engineering Science*, vol. 64, no. 20, pp. 4222–4236, oct 2009.

[17] H. Liu, D. K. Tafti, and T. Li, "Hybrid parallelism in MFIX CFD-DEM using OpenMP," *Powder Technology*, vol. 259, pp. 22–29, jun 2014.

[18] A. Sharma, S. Wang, V. Pareek, H. Yang, and D. Zhang, "Multi-fluid reactive modeling of fluidized bed pyrolysis process," *Chemical Engineering Science*, vol. 123, pp. 311–321, feb 2015.

[19] S. Yang, K. Luo, M. Fang, and J. Fan, "LES-DEM investigation of the solid transportation mechanism in a 3-D bubbling fluidized bed. Part II: Solid dispersion and circulation properties," *Powder Technology*, vol. 256, pp. 395–403, apr 2014.

[20] S. Radl and S. Sundaresan, "Coarse-Grid Simulations Using Parcels: An Advanced Drag Model based on Filtered CFD-DEM Data," 2013.

[21] Y. Wang, Z. Zou, H. Li, and Q. Zhu, "A new drag model for TFM simulation of gas-solid bubbling fluidized beds with Geldart-B particles," *Particuology*, sep 2013.

[22] C. Loha, H. Chattopadhyay, and P. K. Chatterjee, "Effect of coefficient of restitution in Euler-Euler CFD simulation of fluidized-bed hydrodynamics," *Particuology*, vol. 15, pp. 170–177, aug 2014.

Chapter

6

Modelling Dust Liberation at the Transfer Point

In Chapter 5, the validity of the CFD-DEM model was assessed for a dense regime of particle flow with a high rate of momentum exchange between the airflow and sand particles. In addition, the CoR between particles and the $\mu_{s,pw}$ and $\mu_{r,pw}$ were determined through experiments and simulations.

The objective of this chapter is to identify the factors that should be considered in the design of the transfer point to reduce dust liberation from a belt conveyor. Hence, a series of experiments is conducted to determine the discharge trajectory of the sand particles at different velocities of the belt conveyor. Furthermore, two different impact plates are utilized at the transfer point to investigate the effect of inclination angle of the impact plate on the trajectory of the sand. Then, the experimental results are used as benchmarks to determine the coefficients of rolling and sliding friction between the belt and sand particles $\mu_{r,pb}$. These values are used in the CFD-DEM model of Chapter 5 to simulated the dust liberation at the transfer point. The CFD-DEM model is finally used as a design tool to investigate the effect of some factors on the rate of dust liberation at the transfer point of a belt conveyor.

In section 6.1, a literature review will be done to briefly survey the conducted studies in the past decade related to dust liberation modelling techniques at the transfer point of belt conveyors. Basic principles of dust liberation at the transfer point of belt conveyors will be presented in section 6.2. Then, the experimental set-up

and numerical settings will be described in section 6.3. Experimental outcomes and CFD-DEM results will be presented in sections 6.4 and 6.5, respectively. Finally, the dust liberation at the transfer point of a belt conveyor will be simulated and studied with the CFD-DEM model in section 6.6.

6.1 A review of the dust liberation modelling techniques

During the past decades, researchers have taken advantage of a multitude of techniques and methodologies such as analytical methods, experimental studies, and numerical tools to study the dust liberation phenomena. In this study, the experimental and numerical studies that are concerned with the dust liberation modelling at the bulk terminals and the material handling equipment have been reviewed.

Storing dry granular material in the open storage yards is one of the major sources of dust liberation in the environment. Computational Fluid Dynamics (CFD) has largely been implemented in previous studies to investigate the effect of the airflow on the dune erosion and to predict the rate of dust liberation from a stockpile [1–3]. A number of studies [4, 5] used a combination between analytical models and CFD method to analyse the effect of airflow around the piles on the rate of dust liberation. In these studies, the airflow around the storage piles was simulated by the CFD method and then its results were utilized in the analytical formula to determine the so-called emission factor [6]. A series of studies [7–12] used experimental data along with the CFD method to investigate the role of saltation and creep modules on the deformation, erosion, and dust liberation rates of a sandpile.

The Eulerian-Lagrangian approach of the CFX tool is another popular method for modelling the dust liberation where fine particles do not have a significant effect on the airflow. Diego et al. [13] modelled the dust liberation around the storage pile in CFX 10.0 software by utilizing the Eulerian-Lagrangian approach. In the CFX, the particles were considered as the volume-less points in the computational domain of the Eulerian-Lagrangian approach and the hypothetical particles were carried with the airflow without any effect on the fluid phase. In this method, the rate of dust liberation from the CFD cells depends on various parameters such as the emission factor, friction velocity, threshold friction velocity, and particle size.

Modelling the particle phase with Lagrangian techniques in the stockpiles is not very cost effective because a huge number of particles is involved in the simulation. Hence, the Eulerian-Lagrangian techniques are usually utilized in modelling the granular material handling equipments such as the belt conveyor because a smaller amount of material needs to be modelled in this kind of equipment in comparison with stockpiles. The transfer chute of belt conveyors has a high potential in generating dust which has been modelled by different numerical methods to minimize blockages and spillage of materials [14–18]. The transfer chute is used in many industries to facilitate bulk material transfer from one conveyor belt to another or for redirecting

flow from a delivery point into a process or into equipment [19].

Researchers [20, 21] performed a series of simulations with the CFD method to model the airflow around a belt conveyor. The dust lift-off model was calibrated with experimental data to incorporate in the CFD method to determine the rate of dust liberation from the materials on a belt conveyor. Also, Kessler et al. [22] conducted experiments and DEM simulations to optimize a number of design parameters of the transfer chute. In addition, the DEM modelling was utilized as a tool to trouble-shoot and optimize the design of a transfer chute for transporting wet and sticky ores [17, 23].

Chen et al. [24, 25] evaluated the rate of dust liberation for six configurations of the transfer chute using experimental data and CFD simulation. A two-phase three-dimensional Eulerian-Eulerian approach was undertaken to qualitatively assess the performance of the transfer chutes. Also, the influence of parameters such as the particle-particle restitution coefficient and the particle-wall slip condition was investigated utilizing the TFM approach [26]. The TFM model was used to assess the effect of viscosity, drag force, and turbulence models on the rate of dust liberation at the transfer chute of a belt conveyor [27]. Also, the profiles of the air velocity obtained from TFM model were compared with the experimental data extracted from the Particle Image Velocimetry (PIV). The bulk material used in the above tests was screened iron ore in which 60% of particles were in the range of 4.0-4.75 mm.

A coupling between the DEM and CFD along with an empirical model for the dust lift-off model was undertaken to determine the dust liberation at a transfer chute [28]. Derakhshani et al. [29] compared the discharge trajectory of mono-sized coarse particles obtained with an analytical solution, DEM method, and CFD-DEM coupling technique at the transfer point of a belt conveyor. A qualitative comparison between the discharge trajectory of the materials was conducted to evaluate the air effect on the discharge trajectory. It was observed that a realistic trajectory of the materials can be seen through coupling the DEM with the CFD to include the effect of air in simulations.

As seen, different numerical techniques were incorporated with empirical or analytical solutions to study dust liberation from the bulk material handling systems. However, as explained in Chapter 2, more detailed information about the particle phase and its interaction with the equipment can be obtained with CFD-DEM coupling. The CFD-DEM model makes it possible to investigate the effect of some factors such as properties of particles and belt conveyor, the speed of a belt conveyor, and the speed and direction of airflow around a belt conveyor on the rate of dust liberation. These data of importance because provides engineers with the insight to design a belt conveyor system with the lowest rate of dust liberation.

6.2 Basic principles of the dust liberation

The transportation velocity of materials, the size and density of materials, the properties of the surrounding air are a number of important factors that influence the rate of dust liberation from the bulk material handling systems [30, 31]. These factors also are the reasons of the material segregation at the transfer point of a belt conveyor [23]. In the other word, it can be said that the dust liberation is a kind of material segregation in a way that the fine particles are segregated from others.

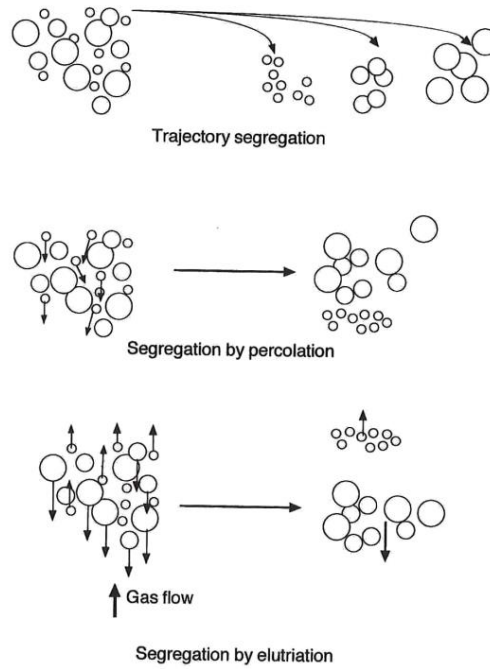

Figure 6.1: Mechanisms of particle segregation [32].

Particles tend to segregate during the handling process such as moving, pouring, and conveying even where they were originally mixed by some means [33]. A significant difference in the particle size is the most important factor that intensifies the segregation of material while the density is comparatively of importance where the densities of materials and surrounding fluid are significantly different, such as in the sedimentation of sand particles within air at the transfer point of a belt conveyor [33]. Figure 6.1 shows three mechanisms that can lead to the particle segregation, namely, trajectory segregation, percolation of fine particles, and elutriation segregation [32].

The vibration of a surface has a direct effect on the rate of particle segregation [14, 34–36]. In this study, it is assumed that the belt conveyor is not vibrated and therefore the effect of vibration on the material segregation and dust liberation will not be studied. Also, the percolation of fine particles can occur during stirring,

shaking, vibration or when materials are poured into a heap [16, 34, 37, 38] so that the fine particles fill the gaps between the coarse particles and move from up to down. Considering the aim of this research which is modelling the dust liberation at the transfer point of a belt conveyor and the absence of any vibration in the belt conveyor system, this type of segregation does not have an influence on the material segregation in this study. Two remaining mechanisms, trajectory and elutriation segregations, are briefly discussed in the following.

1. Trajectory segregation

If a small particle is projected horizontally with an initial velocity into a fluid, it can horizontally travel a certain distance (Δx_h). The horizontal distance depends on the properties of the particle and fluid, the regime of fluid flow, and its initial velocity as was explained in Chapter 3. It is extracted from the governing equation of particle movement within a fluid that a particle with diameter of $2D_p$ travels four times larger than a particle with diameter of D_p in a Stokes flow regime ($\Delta x_h \propto {D_p}^2$). The difference between Δx_h is due to difference in the exerted drag force on the coarse and fine particles. Consequently, coarse particles can travel further away from the transfer point of a belt conveyor compared to the fine particles and this is one of the reasons for particle segregation and dust liberation at the transfer point.

2. Elutriation segregation

The elutriation segregation occurs in the case that the velocity of airflow is not equal to the terminal velocities of particles with different physical properties [32]. Part of the segregation at the transfer point of a belt conveyor is because of the elutriation segregation which is due to the different exerted drag force on the particles with different size. Actually, the entrained air in the discharge trajectory of a belt conveyor can segregate the fine particles from the material stream and carry them out into the surroundings [39] as dust (see Figure 6.1).

The carry-back effect is the other factor that can be added to the segregation mechanisms at the transfer point of a belt conveyor. Fine particles are wrapped around the belt conveyor even after the discharge point [23] which is because of the strong viscose effect close to the surface of belt conveyor. The wrapping effect increases the discharge angle of the fine particles compared to the coarse particles so that fine particles are concentrated at the lower bound of discharge trajectory.

The trajectory and elutriation segregation as well as the viscous effect will be studied in this chapter. Also, the effect of some other factors such as the properties of the belt conveyor and particles on the dust liberation will be parametrically investigated.

6.3 Experimental set-up and numerical settings

In this section, the conveyor set-up along with its dimensions and the experimental plan are explained. Also, the settings and parameters of the CFD-DEM model employed in the simulations of this chapter are presented in detail.

6.3.1 The belt conveyor set-up

Figure 6.2 shows a picture of the conveyor set-up and the sand feeder. A black-white grid plane with the scale of 1 mm was used to determine the discharge trajectory of the sand particles.

(a) (b)

Figure 6.2: A picture of the experimental set-up a) the belt conveyor and the driving motor b) the sand feeder.

The schematic layout of the conveyor set-up, sand feeder, and impact plate is illustrated in Figure 6.3 and the corresponding dimensions of this figure are presented in Table 6.1.

Table 6.1: The geometric size of the belt conveyor and the other component.

Parameter	l	l_{ip}	l_{c-h}	w_b	w_{ip}	h_1	R_r	t_b
Size (mm)	1100	150	58.5	450	11	20	39	3

Where, w_b and t_b are the width and thickness of the belt conveyor and w_{ip} is the width of impact plate. The position of the sand feeder l_1 needs to be determined experimentally in a way that the inserted sand has sufficient time to settle on the belt conveyor before arriving at the head pulley.

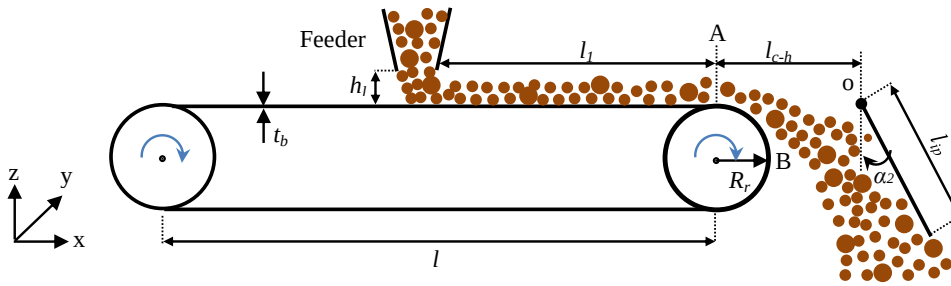

Figure 6.3: A schematic picture of the belt conveyor, sand feeder, and impact plate together with the position and dimension of each components.

The belt conveyor set-up has a driver by a motor with the power of $0.55\,kW$. The belt speed can be adjusted in the range of $0.0\,m/s$ to $0.8\,m/s$ with a variable-frequency drive controller that is seen in Figure 6.4. Voltcraft speedometer (DT-30LK) seen in this figure is used to determine the speed of belt conveyor during the experiments.

(a) (b)

Figure 6.4: Controlling and measuring the speed of belt conveyor: a) Variable-frequency drive controller, b) Voltcraft speedometer.

The experiments are filmed with a Sony Alpha ILCE-5000 camera which is set to 50 frames per second with video resolution of 1920×1080. It should be noted that the photos taken by the camera are affected by the perspective effect between points 'A' and 'B' of Figure 6.3. Therefore, the experimental results at intervals after point 'B' are used in this study to assess the accuracy of simulation results.

6.3.2 The experimental plan

A series of experiments will be conducted in this research to investigate the accuracy of the CFD-DEM model. The procedure of preparing the experimental set-up and the plan of performing the experiments are presented in this section.

1. Determination of $\mu_{s,pb}$

The same procedure used for determining the $\mu_{s,pw}$ in section 5.3.3 will be utilized in this chapter to measure the $\mu_{s,pb}$.

2. Position of sand feeder

The distance of sand feeder l_1 from point 'A' should be large enough so that the inserted particles have sufficient time to reach the speed of belt conveyor and settle on the belt before the transfer point (see Figure 6.3). Hence, l_1 will be increased to the extent that all particles reach to the speed of belt conveyor.

On the other side, the number of particles in a simulation increases by increasing l_1 so that it can lead to an increase in the computational time. Accordingly, the minimum length of l_1 will experimentally be determined and it will be utilized in the simulations of this study. In addition, the distance that particles travel to reach the belt speed will be used in the determination of the coefficient of rolling friction between sand particles and belt $\mu_{r,pb}$ in a way that will be explained in section 6.3.3.

3. Mass flow rate of feeder

The thickness of the discharge trajectory depends on various factors such as the speed of a belt conveyor, particle size and density, properties of the surrounding fluid, and the direction of the airflow around the conveyor [23].

The mass flow rate of sand particles from the feeder will experimentally be adjusted through setting the output diameter of the feeder and the mass flow rate will be measured several times to ensure the consistency of the calibration.

4. Speed and inclination angle of a belt conveyor

The discharge trajectory of sand particles at the transfer point of a belt conveyor depends on the inclination angle of the belt α_1, initial velocity of particles, and the driving and damping forces which is known as the projectile motion [40].

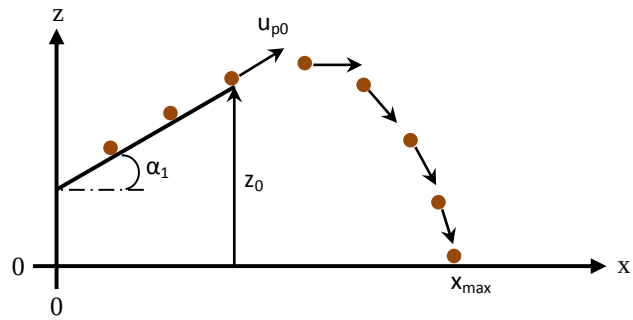

Figure 6.5: Variation of the horizontal displacement of sand particles versus the inclination angle of the belt.

Without considering the effect of damping drag forces from surrounding air, the maximum horizontal displacement of a particle is calculated as follows.

$$x_{max} = u_{p_0} cos(\alpha_1) \frac{u_{p_0} sin(\alpha_1) + \sqrt{(u_{p_0} sin(\alpha_1))^2 + 2gz_0)}}{g} \tag{6.1}$$

In this research, the discharge trajectory of sand particles will be measured at the belt speeds of 0.2, 0.4, 0.6, and 0.8 m/s to assess the effect of belt speed on the discharge trajectory of sand particles. Also, considering the limitation in changing the inclination angle of conveyor set-up, two inclination angles of $\alpha_1 = 3.5°$ and $\alpha_1 = 7.0°$ will be used to investigate the effect of α_1 on the discharge trajectory of sand particles at the transfer point. These experimental results will be used in the accuracy assessment of the CFD-DEM model.

5. Implementation of impact plate

The impact plate is part of a transfer arrangement and usually needs the most maintenance. A non-optimized design of impact plates can lead to various problems such as the impact plate wear and damages, spillage of material, degradation of material, material hang-ups, blockage of the transfer point, noise emission, and high

maintenance cost [23].

Five different scenarios that may happen for materials colliding with an impact plate are continuous stick, continuous slip, slip-stick, slip-reversal, jam-stick [41]. Considering the fact that the sand particles are incohesive and spherical and the impact plate and particles are rigid bodies, it can be concluded that the slip-reversal scenario will happen at the contact point of the sand particles with the impact plate. It means particles may slightly slip at the contact point before separation from the impact plate.

In this research, a rectangular impact plate will be used to investigate the effect of the impact plate on the discharge trajectory of sand particles. The impact plate is installed in front of conveyor and it can rotate around point 'o' for α_2 degrees (Figure 6.3). The point 'o' is located in the same vertical level of the belt conveyor where l_{c-h} is the distance between points 'A' and 'o'.

The horizontal position of the impact plate with inclination angle of 16.0° is adjusted in a way to have similar discharge trajectory with the vertical impact plate before the contact point. Accordingly, the rebounding trajectories after the collision with the impact plates will be comparable for both cases. Also, the inclination angle of 16.0° makes it possible to capture the slip-reversal scenario at the contact point.

6.3.3 The CFD-DEM settings and simulation plan

As discussed earlier, an unavoidable limitation of the CFD-DEM technique is its computational expense. Considering the goal of this research, that is modelling the dust liberation at the transfer point of a belt conveyor, a fraction of the experimental set-up including the sand feeder and the transfer point will be modelled instead of the whole domain to reduce the numerical computational effort.

1. The CFD-DEM settings and domain size

A part of the experimental set-up (see Figure 6.3) that will be simulated in this study is shown in Figure 6.6.

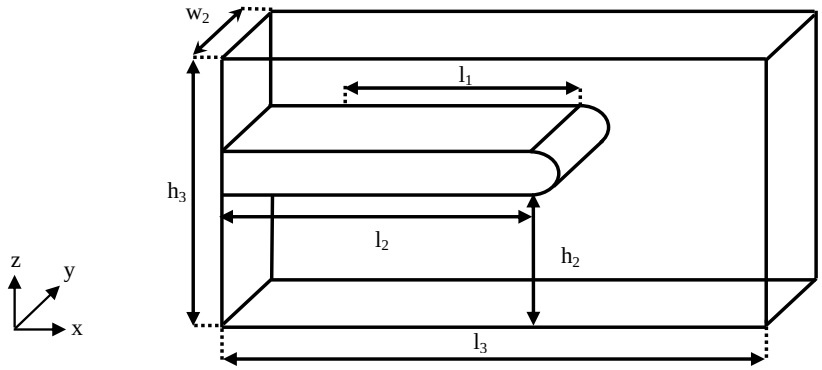

Figure 6.6: The schematic layout of a fraction of the experimental set-up and the domain size of the CFD-DEM model.

The no-slip wall boundary condition at the walls of the CFD domain along with the Neumann and Dirichlet boundary conditions [42] on the other boundaries of the CFD model will be used in modelling the transfer point. The flow regime in the CFD model is set on the laminar model, because the stagnant air has surrounded the conveyor. The boundary conditions of the CFD model are presented in Table 6.2.

Table 6.2: The boundary conditions of the CFD fields in accordance with Figure 6.6.

The position of the CFD wall	Boundary field		
	p	u_f	ksl, ρ_f, u_p, ϵ_f
Left	totalPressure	zeroGradient	zeroGradient
Right	totalPressure	zeroGradient	zeroGradient
Top	zeroGradient	fixedValue	zeroGradient
Bottom	zeroGradient	fixedValue	zeroGradient
Conveyor	zeroGradient	fixedValue	zeroGradient
Impact plate	zeroGradient	fixedValue	zeroGradient
Front and Back	slip	slip	slip

The sub-models and parameters of the CFD-DEM model that were determined in the previous chapters are given in Tables 6.3.

Table 6.3: The sub-models and parameters of the CFD-DEM model.

Force model	Voidage model	Coupling interval	Δt_{DEM} (sec)	Δt_{CFD} (sec)	$\Delta x, \Delta y, \Delta z$ (mm)	e_{pp}	e_{pb}
Gidaspow	Divided	10000	1.0e-7	1.0e-3	1.25	0.9	0.5

The Hertz-Mindlin contact model is employed in the DEM model and the rolling friction model is set to 'epsd2' which was proposed by Iwashita [43] and its theoretical background was described in Chapter 4.

2. The numerical plan

The CFD-DEM model needs to be prepared for modelling the discharge trajectory of a belt conveyor and it will be used to study different conditions based on the experimental data in the first part of this numerical study. The second part of this study is dedicated to the parametric study to investigate the effect of some design factors on the dust liberation.

Table 6.4 shows the numerical plan for evaluating the CFD-DEM model in the first part of numerical study. According to Hastie [23], the effect of the particle shape can be represented by the coefficient of rolling friction in the DEM simulation. He suggested to use a fraction of the coefficient of sliding friction between the particles and the belt conveyor $\mu_{s,pb}$ as the coefficient of rolling friction between particles and belt conveyor $\mu_{r,pb}$. Therefore, $\mu_{s,pb}$ will be measured in section 6.4.1 through the experimental investigations and then $\mu_{r,pb}$ will be determined trough the CFD-DEM simulations in section 6.5.2.

Table 6.4: The numerical plan for preparation and evaluation of the CFD-DEM model.

Case study	u_b (m/s)	$\dot{m}_p$ (kg/s)	α_1 $(degree)$	α_2 $(degree)$	PSD (μm)
Determination of $\mu_{r,pb}$	0.8	0.001	0	N.A.	Table 4.1
DEM vs. CFD-DEM	0.8	0.006	0	N.A.	300 600
Belt speed	0.2, 0.4, 0.6, 0.8	0.006	0	N.A.	Table 4.1
Inclined conveyor	0.8	0.006	3.5 7.0	N.A.	Table 4.1
Impact plate	0.8	0.006	0	0.0 16.0	Table 4.1

The other coefficients of friction between the sand particles and components of the conveyor are listed in Table 6.5.

Table 6.5: The coefficients of rolling and sliding friction between sand particles and particles-components.

Parameter	$\mu_{s,pp}$	$\mu_{r,pp}$	$\mu_{s,ph}$	$\mu_{r,ph}$	$\mu_{s,pb}$	$\mu_{r,pb}$
Value	0.49	0.30	0.32	0.30	measured	determined

The other issue that will be investigated in this study is about the difference between the discharge trajectories predicted by DEM and CFD-DEM models. Afterward, the accuracy of the CFD-DEM model will be assessed at the different speeds and inclination angles of the belt conveyor. In addition, the simulation results are compared with the experimental observations in the case that an impact plate is implemented in front of discharge trajectory of sand particles.

In the second part, the dust liberation is parametrically studied with the CFD-DEM model. Table 6.6 shows the variation range of some design factors that will be used in the parametric study. The bold font in Table 6.6 indicates the base values that are used in the CFD-DEM simulations.

Table 6.6: The variation of design factors in paramedic study of dust liberation at the transfer point of a belt conveyor.

Parameter	D_p (μm)	u_a (m/s)	ρ_p (kg/m^3)	e_{pp}	e_{pb}
Variation range	300	-0.5	1500	0.1	0.1
	600	**0.0**	**2650**	**0.9**	**0.5**
	PSD	0.5	3000		0.9

As explained in Chapter 1, the particles are categorized in to three groups based on their size. It is seen that the particles with diameter between $1\,\mu m$ to $100\,\mu m$ are

in the group of the settling atmospheric dust which can suspend in the air for long times. Hence, a small quantity of fine particles with diameter $10\,\mu m$ is added into the sand particles with the PSD of Table 4.1.

This modification in the PSD facilitates the parametric study in modelling the liberation of very fine particles from the transfer point. Table 6.7 shows the modified PSD of the sand particles based on the mass fraction and numerical percent after adding particles with diameter $10\,\mu m$.

Table 6.7: The particle size distribution of sand particles after adding a small quantity of the fine particles with diameter of $10\,\mu m$

D_p (μm)	Mass fraction (%)	Percent based on the number of particles (%)
10	0.000005	0.55
300	6.000006	24.43
420	18.000018	26.70
500	25.999921	22.87
600	50.000050	25.45

6.4 Experimental results

In this section, the coefficient of sliding friction between the sand particles and the belt conveyor was measured and then the discharge trajectory of sand particles at the transfer point was determined at different speeds and inclination angles of the belt conveyor. The experimental results of this section will be utilized in the next section to determine the coefficient of rolling friction between sand particles and the belt conveyor and to assess the accuracy of the simulation results.

6.4.1 Determination of $\mu_{s,pb}$

The coefficient of sliding friction between sand particles and belt conveyor $\mu_{s,pb}$ was measured separately, by building a sand pack of uniform thickness on the belt conveyor and then tilting it until sand particles slid off.

Figure 6.7: The shape of quartz sand grains.

As seen in Figure 6.7, the sand particles have irregular shape so that they cannot roll on the surface by tilting the belt. The experimental observation confirmed that

sand particles purely slid on the belt at the sliding angle of 28.8°. This value will be utilized in section 6.5 to determine $\mu_{r,pb}$ and also in modelling the discharge trajectories of sand particles at different conditions.

6.4.2 The position of the feeder

The experimental observation indicated that sand particles will get stable on the belt at a distance of 40 mm after the position of feeder at the belt speed of 0.8 m/s. Hence, the sand feeder was placed at $l_1 = 50\,mm$ in the experimental set-up and numerical model to ensure the stability of sand particles on the belt. Figure 6.8 shows a close-up view of the sand feeder, belt conveyor, and sand particles.

Figure 6.8: Position of the sand feeder on the belt conveyor set-up.

6.4.3 Measuring the mass flow rate of feeder

In this study, the mass flow rates of 0.001 kg/s and 0.006 kg/s will be utilized in the experiments and simulations. These mass flow rates were measured five times for both feeders and the experimental investigations indicated that the uncertainty of the mass flow rate at both $\dot{m}_p$ of 0.001 kg/s and 0.006 kg/s is around $\pm 0.0002\,kg/s$.

The experimental results obtained at $\dot{m}_p$ 0.001 kg/s and u_b 0.8 m/s are used to determine $\mu_{r,pb}$. The reason is that at the mass flow rate of 0.001 kg/s only one layer of sand particles sits on the belt conveyor which is a proper state to determine the rolling friction between sand particles and belt. On the other side, the dust liberation modelling at the transfer point is the goal of this research. For that, the mass flow rate of 0.006 kg/s will be utilized in the simulations to involve more particles in the simulation and to illustrate states closer to reality.

6.4.4 The discharge trajectory of the sand particles

The discharge trajectories of sand particles were compared at the belt speed of 0.8 m/s for two mass flow rates of 0.001 kg/s and 0.006 kg/s. As seen in Figure 6.9, the profile of the upper trajectories of both mass flow rates are similar to each other while there is a difference between the lower trajectories which is due to different reasons.

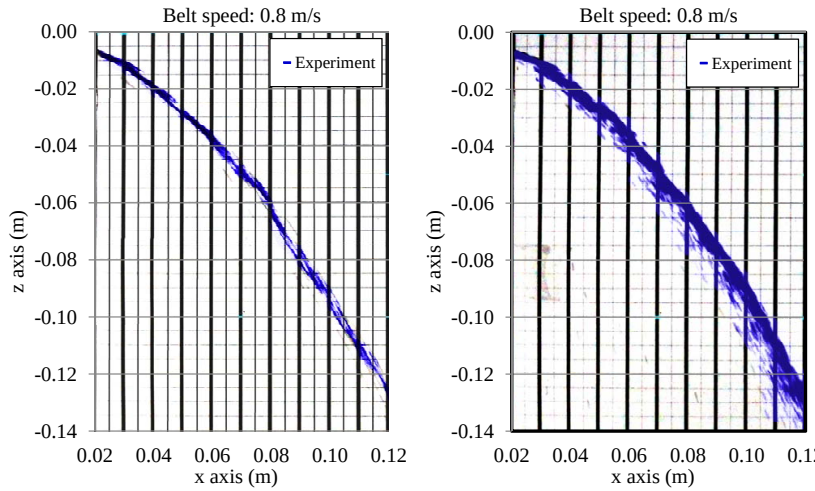

Figure 6.9: The effect of mass flow rate on the discharge trajectory of sand particles at $u_b = 0.8\,m/s$. Left: $\dot{m}_p = 0.001\,kg/s$, right: $\dot{m}_p = 0.006\,kg/s$.

Regarding the upper trajectory, the maximum horizontal distance that particles travel depends on the initial velocity of particles which is same at both mass flow rates which led to the same upper trajectories. On the other side, segregation of sand particles and the wrapping effect increased due to the increase in the rate of mass flow so that the width of discharge trajectory (a distance between the upper and lower trajectories at the same height) at $\dot{m} = 0.006\,kg/s$ is larger than at $\dot{m} = 0.001\,kg/s$. These effects will be investigated in detail with the numerical model.

In another part of the experiments, the discharge trajectories at the belt speeds of 0.2, 0.4, 0.6, and 0.8 m/s were measured to investigate the effect of belt speed on the trajectories of the materials. Figure 6.10 shows the discharge trajectories at different speeds of the belt for the mass flow rate of $0.006\,kg/s$.

As expected, the particles travel further distance in the x-direction with the increase in the belt speed from 0.2 m/s to 0.8 m/s. Another thing is related to the width of discharge trajectories at different speeds of the belt. At low speeds of the belt, materials wrap around the belt at the transfer point and leave the surface of the belt at large wrap angles. It will lead to an increase in the width of discharge trajectory of materials. As seen in Figure 6.10, the width of discharge trajectories decreased at high speeds of the belt.

Some particles were separated from the left side of trajectory at the belt speed of 0.8 m/s which increased a little the width of the trajectory compared to 0.6 m/s. It maybe due to the segregation effect that is cause by the drag force at the high speed of belt which will be investigated with the CFD-DEM model in the next sections.

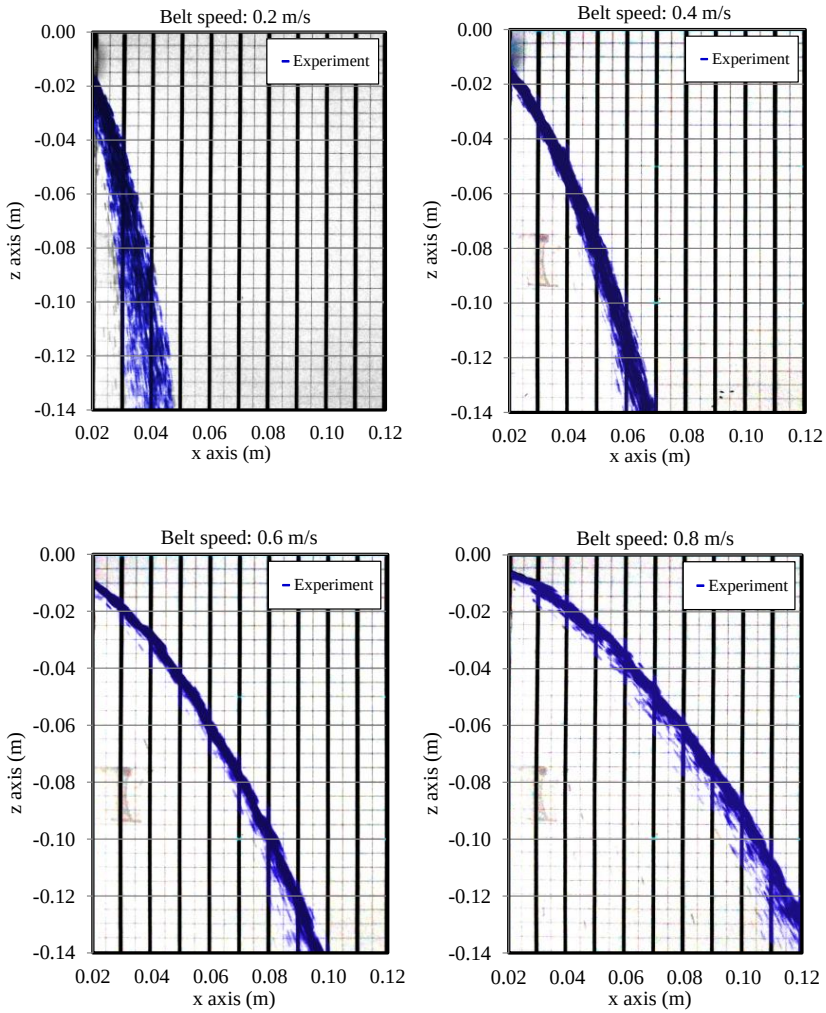

Figure 6.10: The discharge trajectory of sand particles at the transfer point at four different speeds of the belt conveyor.

6.4.5 Inclined conveyor

The trajectory of sand particles was also measured at two inclination angles of the conveyor at belt speed of $0.8\,m/s$. Figure 6.11 shows the effect of inclination angle on the discharge trajectories of sand.

It was observed that the sand particles on a belt conveyor with higher inclination angle travel further, which is in agreement with the theory of the projectile motion [40]. These experimental results will be utilized in section 6.5 in assessing the accuracy of the CFD-DEM model.

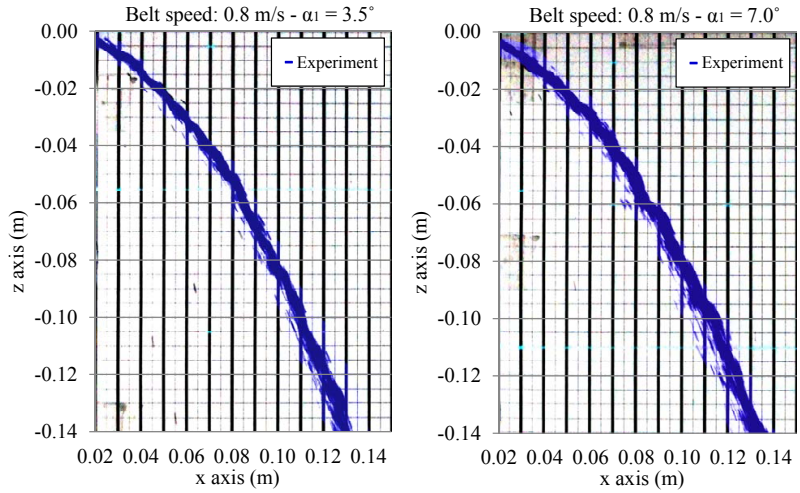

Figure 6.11: The discharge trajectory of sand particles for different inclination angles of the conveyor at the belt speed of $0.8\,m/s$.

6.4.6 Utilization of impact plate

The discharge trajectories of sand particles that were in collision with an impact plate with two different inclination angles were determined in this part. Figure 6.12 shows the discharge trajectories for the inclination angles of $\alpha_2 = 0.0°$ and $\alpha_2 = 16.0°$ at the belt speed of $0.8\,m/s$.

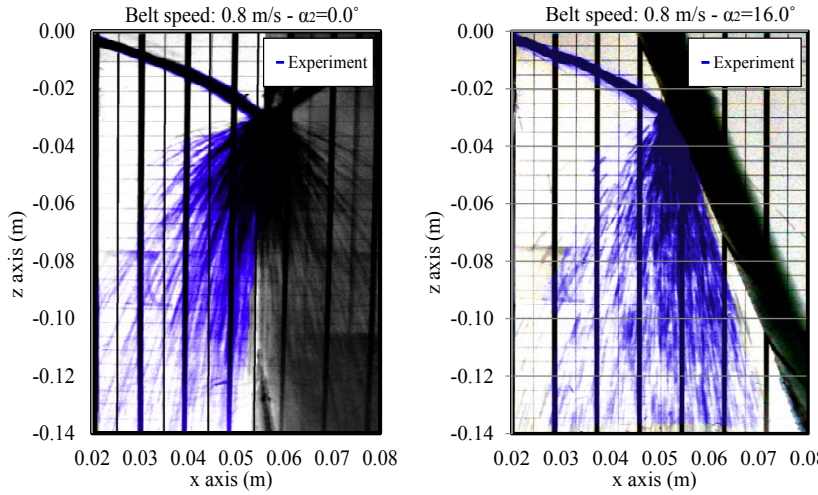

Figure 6.12: The discharge trajectory of sand particles during a collision with an impact plate at the belt speed of $0.8\,m/s$. Left: $\alpha_2 = 0.0°$, right: $\alpha_2 = 16.0°$

As expected, the discharge trajectories are the same for both inclination angles before the contact point. On the other side, the different trajectories after the contact point are due to the different contact angles between the particles and plates which explained in section 6.3.2. The rebounding process is clearly seen when α_2 increases from 0.0° to 16.0°. This experimental results will be utilized later to assess the validity of the CFD-DEM model.

6.5 CFD-DEM results

In this section, the validated CFD-DEM model of Chapter 5 is used to determine $\mu_{r,pb}$ based on the experimental results of the previous section. Also, the accuracy of the CFD-DEM model is assessed at different conditions of the conveyor set-up. At the end, a parametric study is conducted to identify the factors that should be considered in the design of the transfer point of a belt conveyor.

6.5.1 Determination of the CFD domain size

In the previous section, it was observed that the height and length of the discharge trajectory of sand particles at the maximum speed of belt conveyor ($0.8\,m/s$) is in the order of $140\,mm$ from point 'A'. Hence, l_3 and h_3 are selected in a way to ensure the discharge trajectory will be captured in the simulations with full details (see Figure 6.6). The dimensions of the CFD and DEM domains are selected according to the values presented in Table 6.8.

Table 6.8: The geometric and domain size of the CFD-DEM model.

Parameter	l_1	l_2	l_3	h_2	h_3	w_2
Size (mm)	50	80	250	150	200	11

6.5.2 Determination of $\mu_{r,pb}$

The sliding angle between the sand particles sand belt were determined 28.8° which represents the coefficient of sliding friction of $tan\,28.8° = 0.55$ [44]. This coefficient together with the coefficients of friction presented in Table 6.5 are used in this section to determine the rolling friction between the sand particles and belt conveyor $\mu_{r,pb}$. Hence, the CFD-DEM simulations were conducted at different $\mu_{r,pb}$ (0.1, 0.2, 0.3, 0.4, 0.5, and 0.6) to assess the effect of $\mu_{r,pb}$ on the speed of particles and the profile of discharging trajectory.

According to the experimental observation, the distances that it takes for the particles to reach the speed of belt and settle on the belt is about four centimetres after the position of the feeder ($x = 7\,cm$) which is 1 cm before point 'A'. Hence, this distance is also measured in the simulations at the different $\mu_{r,pb}$ to determine $\mu_{r,pb}$ based on the length of this distance. The speed of particles on the belt is shown in Figure 6.13.

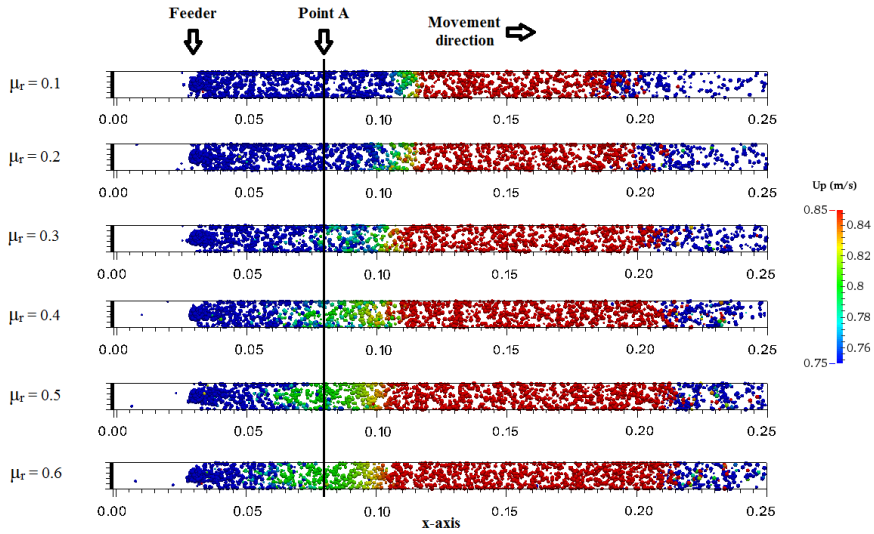

Figure 6.13: Top view of the belt conveyor that was used to determine $\mu_{r,pb}$ based on the speed of particles at $x = 7\,cm$, $u_b = 0.8\,m/s$.

Figure 6.13 indicated that the preliminary determinations of $\mu_{r,pb}$ is 0.5 and 0.6 because particles reach the belt speed at $x = 7\,cm$ for both values (green colour: $u_p = 0.8\,m/s$). At this stage, the discharge trajectories of the CFD-DEM model obtained at the mentioned range of $\mu_{r,pb}$ were compared with the experimental data to assess the effect of $\mu_{r,pb}$ on the discharge trajectory of particles.

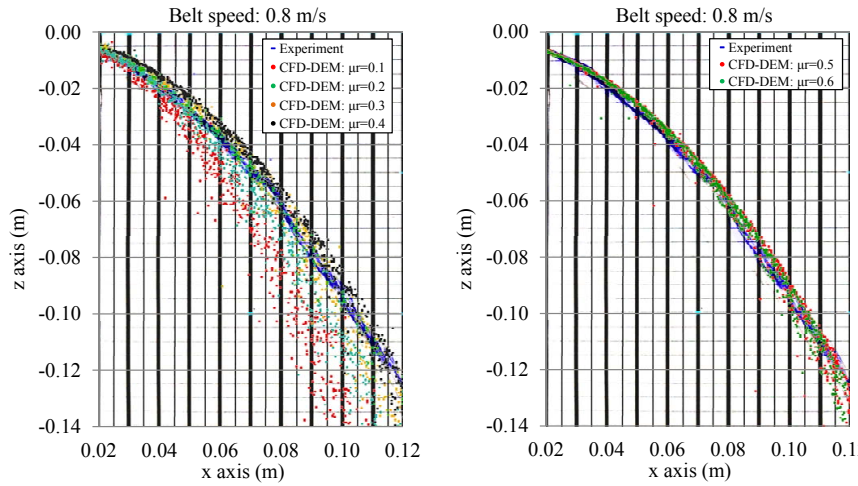

Figure 6.14: A comparison between the discharge trajectories of sand particles at $\mu_{r,pb}$ of 0.1, 0.2, 0.3, 0.4, 0.5, and 0.6.

As can be seen in Figure 6.14, the simulation results obtained based on $\mu_{r,pb}$ of

0.5 and 0.6 are identical and are in good agreement with the experimental results. It means that particles reach the belt speed at $\mu_{r,pb} = 0.5$ and the rotational movement of particles gets zero at $x = 7\,cm$ so that a further increase in $\mu_{r,pb}$ will have not any effect on the rotational movement of particles. Hence, the $\mu_{r,pb}$ of 0.5 will be considered as the coefficient of rolling friction between sand particles and belt conveyor and it will be employed in the subsequent simulations.

6.5.3 Comparison between DEM and CFD-DEM results

The discharge trajectories of the DEM and CFD-DEM models were compared at the belt speed of $0.8\,m/s$ and $\dot{m}_p = 0.001\,kg/s$.

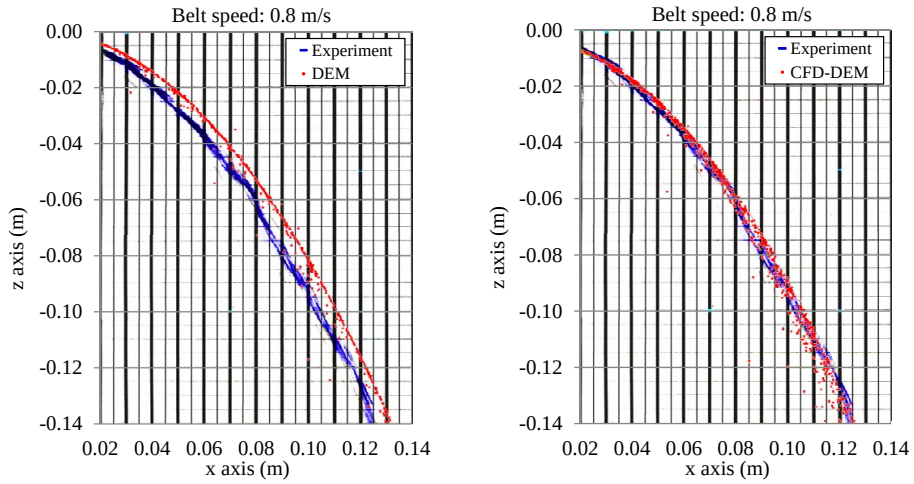

Figure 6.15: A comparison between the discharge trajectory modelled with the DEM and CFD-DEM methods at $u_b = 0.8\,m/s$ and $\dot{m}_p = 0.001\,kg/s$.

As can be seen in Figure 6.15, the result of the CFD-DEM model fits very well with the experimental trajectory while the trajectory of the DEM model is located on the right side of experimental data.

This difference is due to the consideration of the air in the CFD-DEM model. The sand particles were not affected by the drag force arising from the air in the DEM model while the drag force was included in the CFD-DEM model. The drag force reduces the kinetic energy of sand particles so that the particles in the CFD-DEM simulation travel a shorter distance compared to the particles in the DEM simulation. This indicates that the CFD-DEM method should be utilized in modelling the discharge trajectory of sand particles to have accurate results.

6.5.4 The speed of belt conveyor

The discharge trajectories at four speeds of belt conveyor and mass flow rate of $0.006\,kg/s$ were modelled with the CFD-DEM method. The CFD-DEM results are

compared with the experimental investigations at the belt speeds of 0.2, 0.4, 0.6, and 0.8 m/s in Figures 6.16 and 6.17.

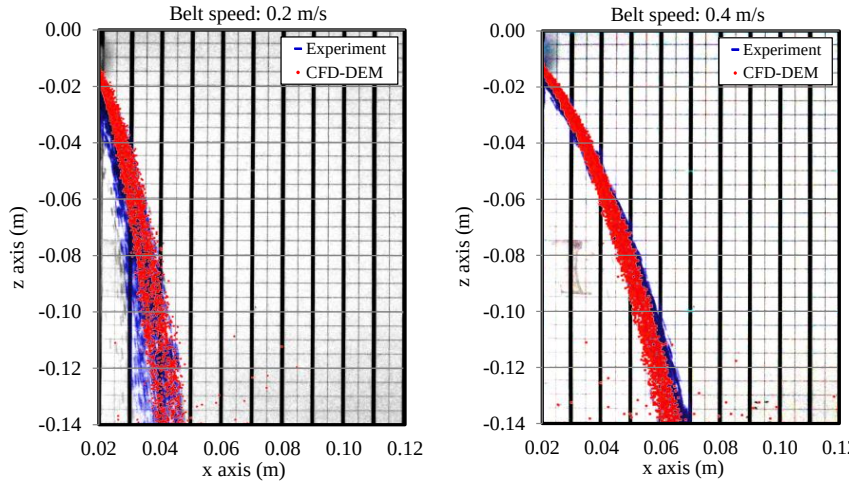

Figure 6.16: A comparison between the experimental and numerical discharge trajectory of sand particles at the belt speeds of 0.2 m/s and 0.4 m/s.

As can be seen in Figures 6.16 and 6.17, the simulation results are in good agreement with the experimental trajectories at all range of belt speed. The discharge trajectories as well as the width of trajectories are very well fitted into the experiments.

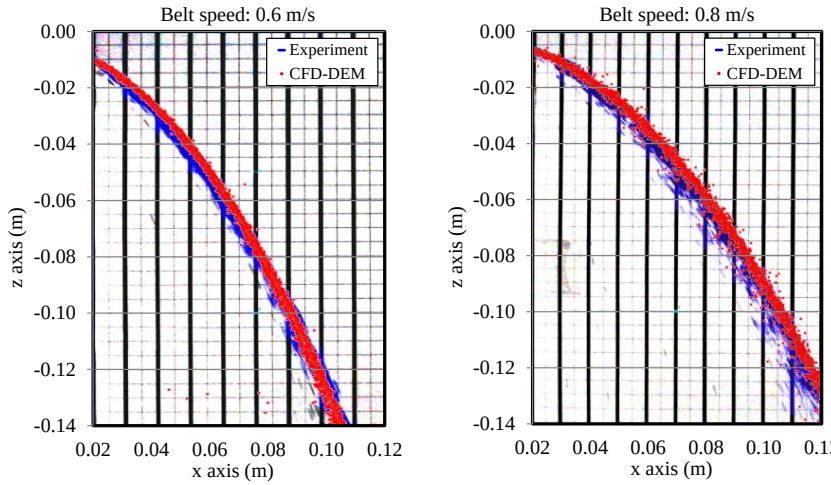

Figure 6.17: A comparison between the experimental and numerical discharge trajectory of sand particles at the belt speeds of 0.6 m/s and 0.8 m/s.

The simulation results of particles speed at different speeds of the belt conveyor is shown in Figure 6.18 from the top view. It is indicated that all particles have

reached the belt speed at the transfer point before leaving the conveyor.

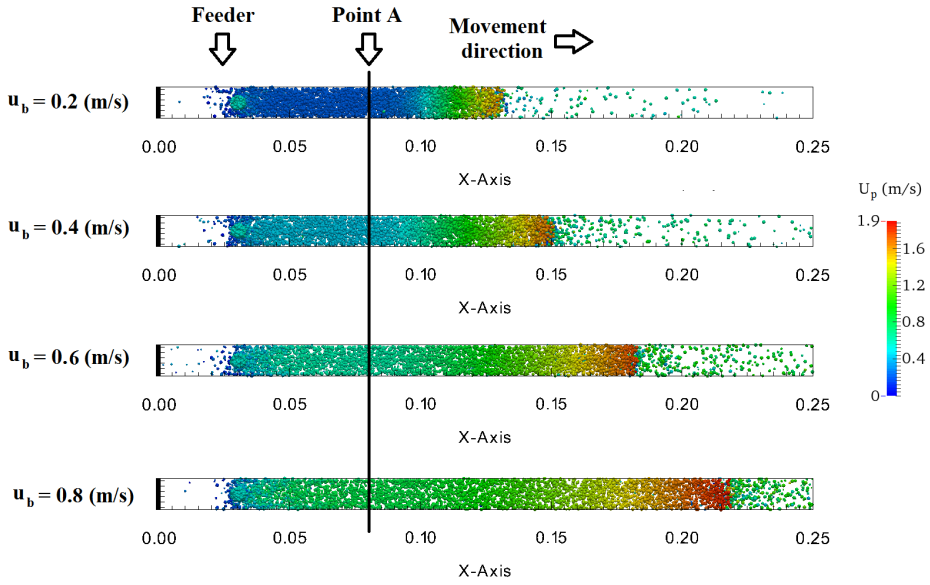

Figure 6.18: A top view from the speed of particles at different speeds of belt conveyor.

The simulation result also confirms the accuracy of $\mu_{r,pb} = 0.5$ at the different speeds of belt conveyor and the mass flow rate of $0.006\,kg/s$. Accordingly, parameters and sub-models of the CFD-DEM model that are specified in Table 6.3 together with the $\mu_{r,pb} = 0.5$ are reliable and they will be utilized in the subsequent simulations of this chapter.

6.5.5 Inclined belt conveyor

The discharge trajectory of particles was modelled for two inclination angles of the belt conveyor, $\alpha_1 = 3.5°$ and $\alpha_1 = 7.0°$ at $u_b = 0.8\,m/s$ and $\dot{m} = 0.006\,kg/s$. The simulation results are presented in Figure 6.19.

The CFD-DEM results are in good agreement with the experimental data for both inclination angles. As explained in section 6.3.2, an increase in the horizontal travel distance of the material should be seen by increasing the inclination angle from $\alpha_1 = 0.0°$ to $\alpha_1 = 7.0°$.

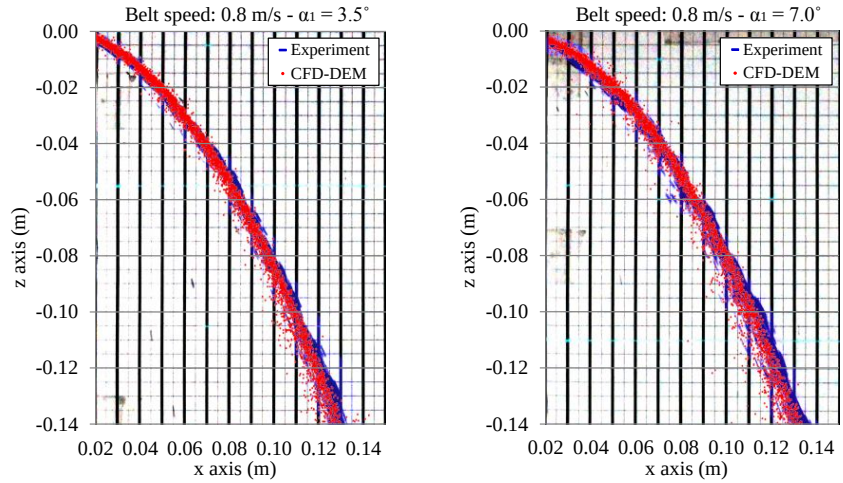

Figure 6.19: Simulation and experimental results of the discharge trajectory for the inclination angles of $\alpha_1 = 3.5°$ and $\alpha_1 = 3.5°$ at $u_b = 0.8\,m/s$.

6.5.6 Utilizing the impact plates

Two impact plates that were experimentally investigated in section 6.4 were simulated here with the CFD-DEM model. Figure 6.20 shows the simulation results of two impact plates with inclination angles of $\alpha_2 = 0.0°$ and $\alpha_2 = 16.0°$.

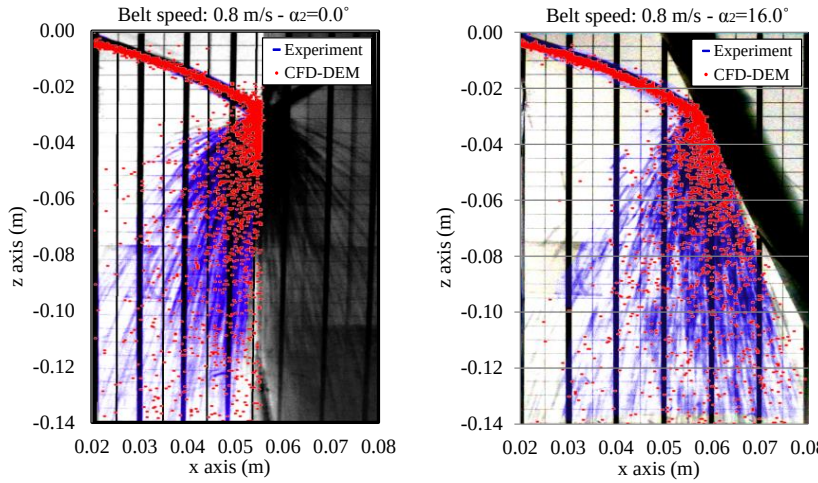

Figure 6.20: The effect of inclination angle of the impact plate on the discharge trajectory at the belt speed of 0.8 m/s. Left: $\alpha_2 = 0.0°$, right: $\alpha_2 = 16.0°$.

The negligible difference between the discharge trajectories for distances less than $0.03\,m$ is because of the position of the camera and the perspective effect of the taken pictures. It should be noted that the travel time and distance of particles

are not sufficiently large to see the effect of drag force on the discharge trajectories before the collision of particles with the impact plates. The rebounding process is also simulated very well at $\alpha_2 = 16.0°$ with the CFD-DEM model while it is seen that some particles are sliding downwards on the impact plate at $\alpha_2 = 0.0°$.

All parameters and sub-models of the CFD-DEM model were re-evaluated in this section based on the experimental data and the required properties of the sand particles and equipment were accurately determined in the previous parts of this research. In the other words, it is concluded that the CFD-DEM model is ready to be utilized in the parametric studies of the next section.

6.6 Dust liberation modelling

The trajectory segregation, elutriation segregation, carry-back effect, the properties of the belt conveyor and particles are the factors that discussed in section 6.2 and in this section are numerically investigated with the CFD-DEM model. These factors are of importance because they influence the dust liberation at the transfer point and consequently they should be considered in the design of the transfer point of a belt conveyor.

6.6.1 The particle size effect

Particle Size Distribution (PSD) is one of the reasons of the material segregation in the discharge trajectories.

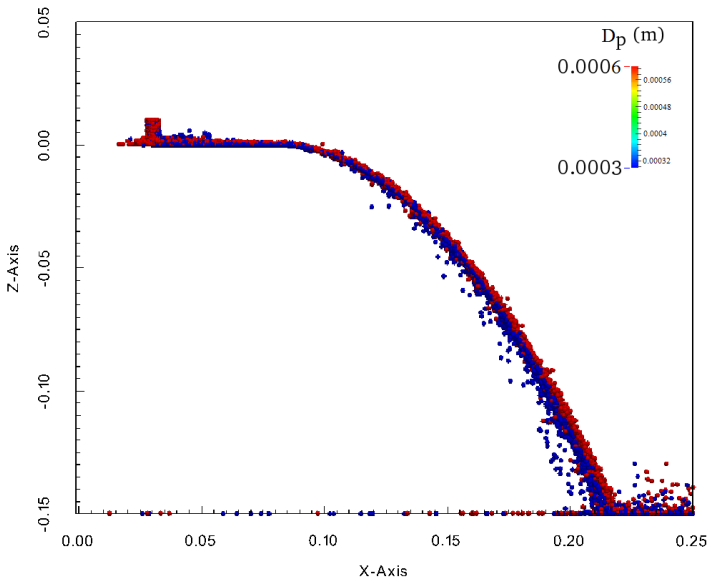

Figure 6.21: A comparison between the discharge trajectories at two different sizes of $D_p = 300\,\mu m$ and $D_p = 600\,\mu m$ at $u_b = 0.8\,m/s$.

In this part, the trajectories of two mono-sized particles, $D_p = 300\,\mu m$ and $D_p = 600\,\mu m$, were individually simulated at $u_b = 0.8\,m/s$ and $\alpha_1 = 0.0°$.

Figure 6.21 shows the discharge trajectories of both simulations in a single plot to illustrate the different between the results. It should be noted that the particle size has been increased in the figures of this section to help identify the position of the particles. As explained in section 6.2, the coarse particles travel further compared to the fine particles. Hence, the discharge trajectory of particles with diameter $D_p = 300\,\mu m$ is on the left side of the discharge trajectory of particles with diameter $D_p = 600\,\mu m$.

6.6.2 The effect of particle density

A parametric study was conducted to investigate the effect of particle density on the discharge trajectory of materials. Figure 6.22 shows that the discharge trajectory of particles with low density ($1500\,kg/m^3$) is wider than the discharge trajectory of particles with density of $3000\,kg/m^3$. Also, particle with the high density travel further compared to the particle with low density which can be due to the different terminal velocity of particle with different densities. Indeed, the terminal velocity of particle with low density is smaller than particle with high density. This difference increases the trajectory segregation for particles with low density. In the other words, the exerted drag force is independent of the particle density so that the discharge trajectory of lighter particles is further to the left compared to the trajectory of particles with the density of $3000\,kg/m^3$.

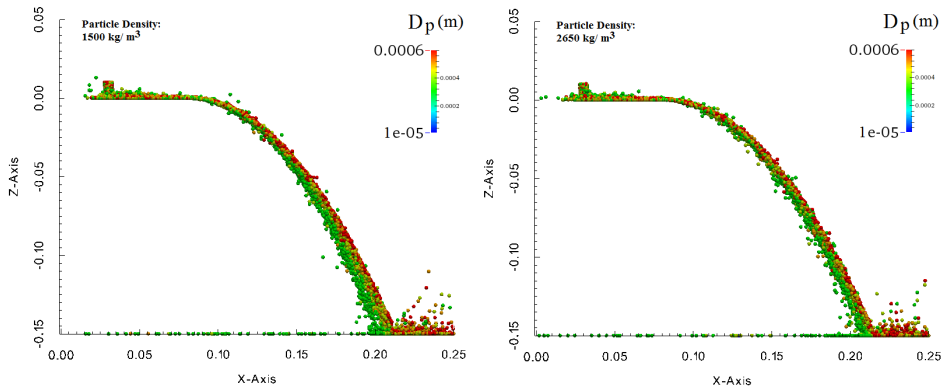

Figure 6.22: A comparison between the discharge trajectory of materials with different densities.

6.6.3 The effect of belt speed

The drag force has a direct relation with the relative velocity between the particles and airflow $\mathbf{u}_{fp}$ and it can be changed based on the speed of belt conveyor. Hence, the speed of belt conveyor is an important factor that influences the dust liberation

at the transfer point. In this part, the discharge trajectories for the belt speeds of 0.2 m/s and 0.8 m/s were simulated with the CFD-DEM model.

Figure 6.23 shows that sand particles were slightly segregated in both speeds of belt. However, the concentration of small particles in the left side of discharge trajectory at $\mathbf{u}_b = 0.8\,m/s$ is more than $\mathbf{u}_b = 0.2\,m/s$. This difference is due to the fact that the initial speed of particles in the conveyor with the belt speed of $0.8\ m/s$ is four times bigger than the other case which exerted more drag force on the particles with the belt speed of $0.8\ m/s$. On the other side, more drag force is exerted on the small particles compared to the coarse particles which increases the segregation effect at the transfer point for the belt conveyors with high speed.

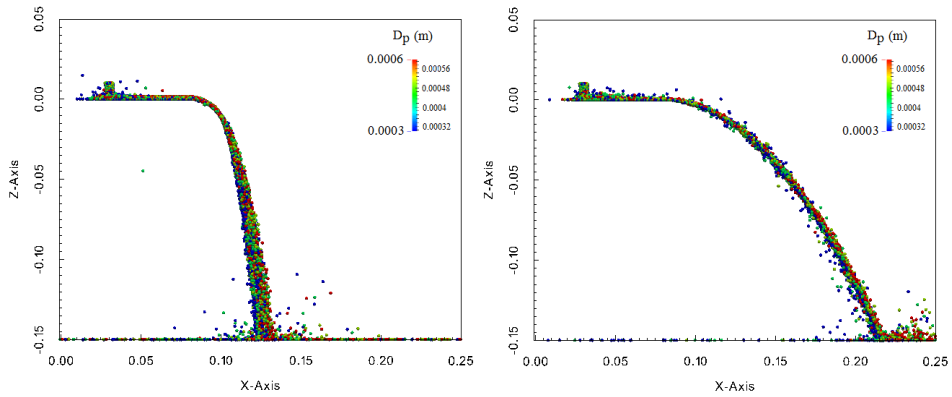

Figure 6.23: The CFD-DEM modelling of the particle segregation in the presence of air at $u_b = 0.2\,m/s$ and $u_b = 0.8\,m/s$.

6.6.4 The effect of airflow speed

The speed and direction of the surrounding air is the other factor that was studied in this part. In fact, the airflow can intensify the segregation effect which results in an increase the rate of dust liberation at the transfer point. For this purpose, the boundary condition of the CFD model was modified in a way that the upper boundary condition of the CFD model has a speed of $0.5\ m/s$ in the positive or negative directions of the x-axis.

Figure 6.24 shows how the surrounding air is induced into the discharge trajectory of the sand particles. The trajectory segregation is not significant because the horizontal component of the drag force is not big enough to push the small particle into the left side of the discharge trajectory. In the other word, the speed of the induced air into the discharge trajectory of sand particles is not strong enough to exert a sufficient drag force on the small particles and separate them from each other. In addition, the size distribution of sand particles is such that the exerted drag force can not significantly influence their movement.

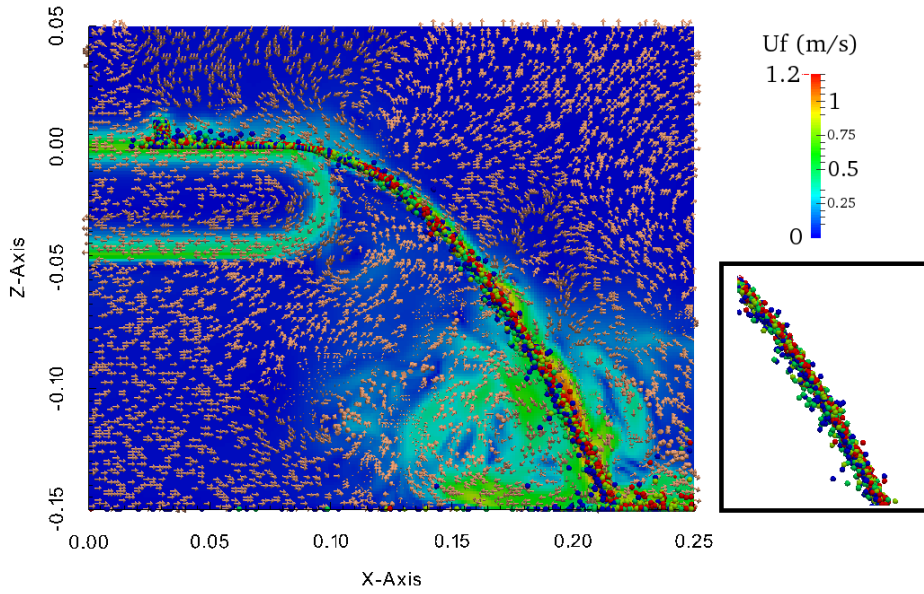

Figure 6.24: Demonstration of the airflow field around the conveyor set-up at t=0.7 s when the initial velocity of surrounding air is zero.

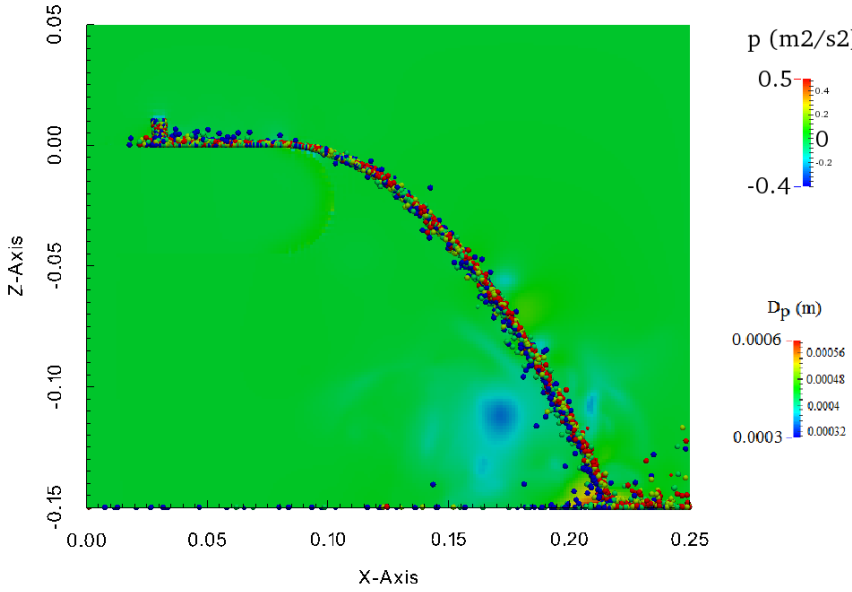

Figure 6.25: The gradient of the pressure domain around the conveyor set-up when the initial air velocity was zero.

As seen in Figure 6.24, some small eddies were created around the discharge

trajectory in the case that the initial speed of the surrounding air was zero. The location of the eddies inside the CFD domain can be determined based on the value of local pressure shown in Figure 6.25. There are a number of dark blue areas ($p = -0.4\,m^2/s^2$) which show the location of the eddies in the domain. Also, this issue can be extended into the next simulations of this study so that any eddy in the CFD simulation indicates the low pressure region in the CFD domain.

At this point, the upper boundary of the CFD domain was moved with a constant speed of 0.5 m/s in the positive direction of the x-axis. Figure 6.26 shows how the small eddies close to the discharge trajectory disappeared when the speed of the airflow on the top boundary of the domain increased to $u_a = 0.5\,m/s$. It is also seen that particles with different sizes have been mixed with each other due to the direction of airflow. As explained in section 6.2, the airflow in the same direction of the belt speed reduces the trajectory segregation because the horizontal component of the drag force decreases in this direction.

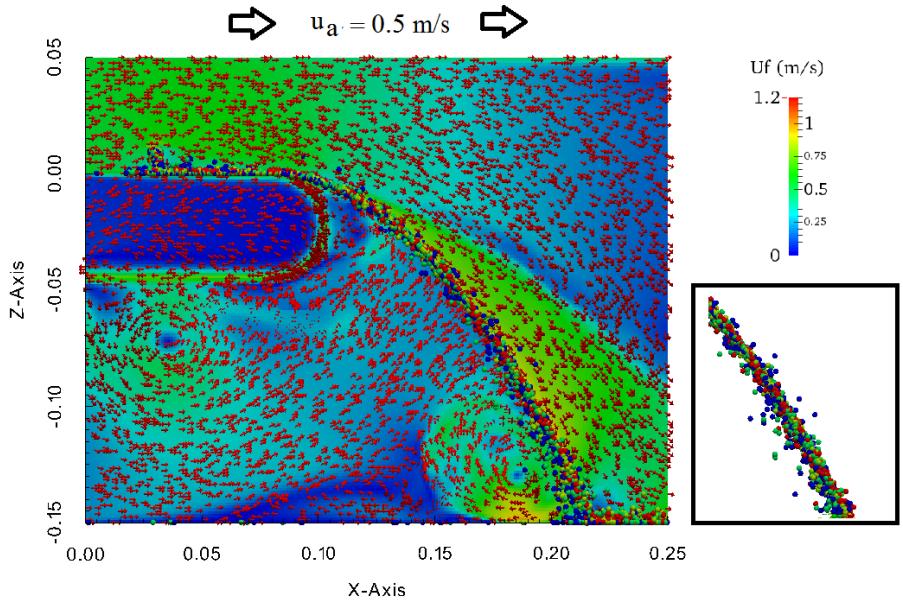

Figure 6.26: The velocity field of airflow around the conveyor when the speed of the airflow is $u_a = 0.5\,m/s$ at the top boundary condition.

Also, the direction of the airflow was changed into the negative direction of the x-axis to investigate its effect on the segregation of sand particles. Figure 6.27 shows how sand particles were clearly segregated at the transfer point due to the trajectory segregation. In addition, the discharge trajectory of sand particles was shifted slightly into the left by the airflow.

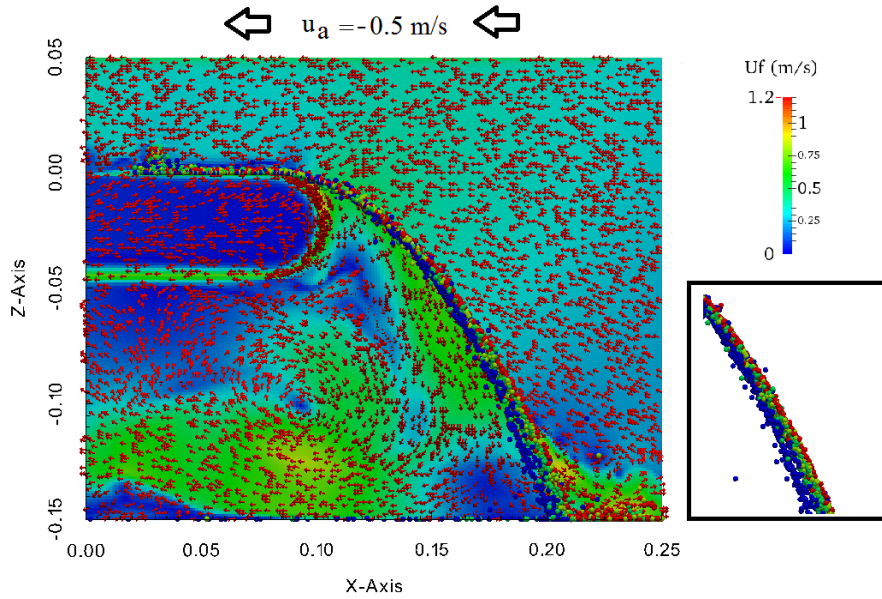

Figure 6.27: The effect of the airflow direction on the segregation of sand particles.

It is shown that the airflow in the negative direction of the x-axis intensified the particle segregation whereas the airflow in the positive direction of the x-axis had an inverse consequence on the particle segregation. This is in agreement with the basic principles of material segregation explained in section 6.2.

6.6.5 Investigating the viscous effect

A small quantity of fine particles with diameter of $10\,\mu m$ was added to the sand particle to study dust liberation at the transfer point and its dispersion around the belt conveyor (see Table 6.7). Hence, the dust liberation phenomenon around the belt conveyor was studied for the situation that the airflow has the speed of 0.5 m/s.

It was observed that a number of particles with diameter of $10\,\mu m$ were separated from the discharge trajectory and left the domain along with the return side of the belt conveyor. The reason for this issue is that the viscous force is a dominant force at the boundary layer of the belt conveyor and fine particles ($10\,\mu m$) are under a higher drag force ($f_d \propto {}^1/_{{D_p}^2}$) compared to the other sizes of sand particles ($f_d \propto {}^1/_{D_p}$).

The particle Reynold numbers at diameter of $10\,\mu m$ and $300\,\mu m$ are 0.54 and 15.1, respectively. In accordance with the particle Reynolds number, the terminal velocities of particles that were determined with equations 3.11 and 3.9 are equal to $0.008\,m/s$ and $1.8\,m/s$. It is seen that terminal velocity of $10\,\mu m$ particles is very small compared to the speed of conveyor and surrounding air which means the sedimentation time is very long for these particles and they will also be carried by the airflow in the whole domain. In other words, the viscous force exerted by the air

on these particles is the dominant force and they follow the airflow in the domain.

On the other hand, the gravitational force on the particles with diameter $300\,\mu m$ is relatively bigger than the viscous force and consequently, these particles can not be suspended in the surrounding air and these particles will settle in shorter time than $10\,\mu m$ particles.

In the previous section, it was explained that the airflow with the speed of $0.5\,m/s$ reduces the trajectory segregation which is seen in the Figures 6.28 and 6.29. These figures also show how particles with a diameter of $10\,\mu m$ were liberated from the discharge trajectory due to the viscous effect. These particles were carried with the return side of the belt conveyor and they trapped into the big eddy below the belt conveyor.

Also, there is another eddy on the left side of the discharge trajectory without particles. This can be seen from the fact that the fine particles are liberated from the discharge trajectory before they arrive to this region which is clearly seen in the right side of the discharge trajectory of Figure 6.28. Also, the direction of the airflow on the top side of this eddy is in a way that guides the fine particles into the main trajectory before they move toward this eddy.

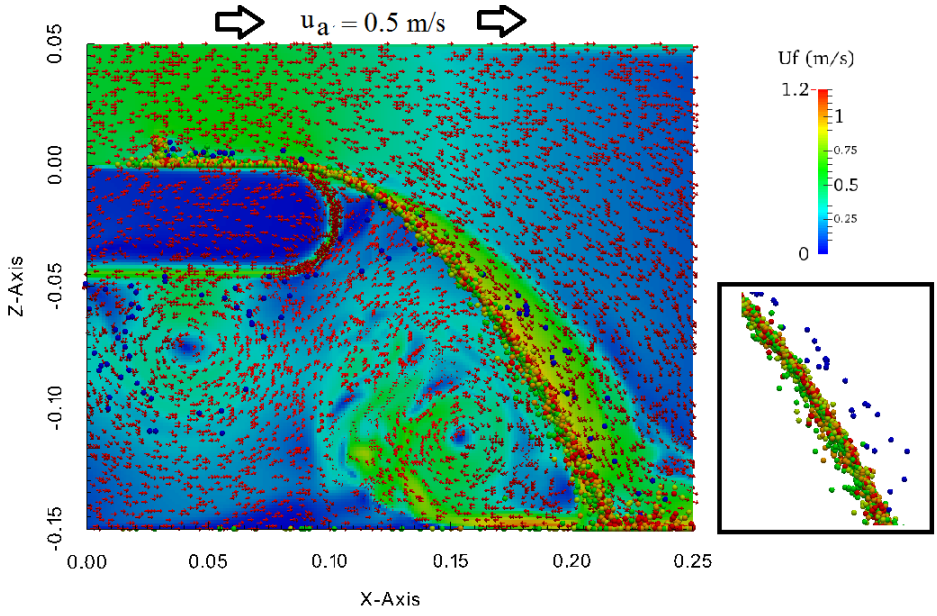

Figure 6.28: The velocity vector filed of the airflow around the conveyor for the $u_a = 0.5\,m/s$ at t=4 *sec*.

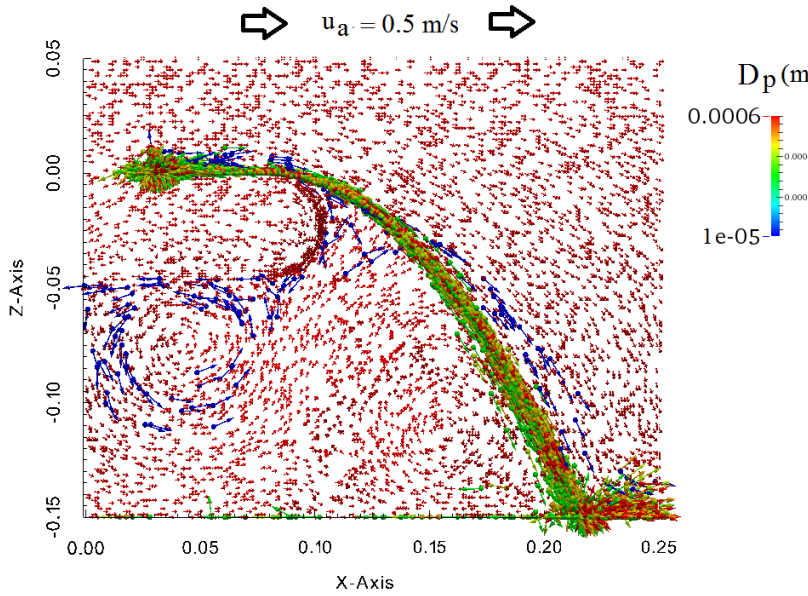

Figure 6.29: The liberation and dispersion of dust from the discharge trajectory for the $u_a = 0.5\,m/s$ at t=4 *sec*.

At this point, the direction of the airflow was changed into the negative direction of the x-axis with constant speed of $-0.5\,m/s$ at the top boundary. As can be seen in the Figures 6.30 and 6.31, the concentration of the dust is significantly increased in comparison with the previous case ($u_a = 0.5\,m/s$). Indeed, the airflow separates the fine particles from the discharge trajectory and carries them into the left side of trajectory. In other words, the trajectory segregation and the viscous effect intensify the rate of dust liberation from the discharge trajectory when the airflow moves in the opposite direction of the belt speed.

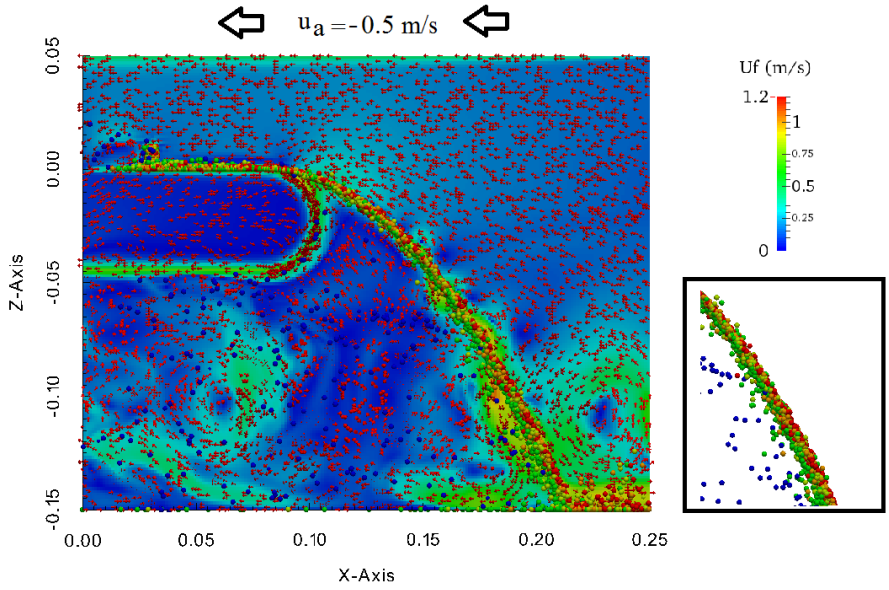

Figure 6.30: The velocity vector filed of the airflow around the conveyor for $u_a = -0.5\,m/s$ at t=4 *sec.*

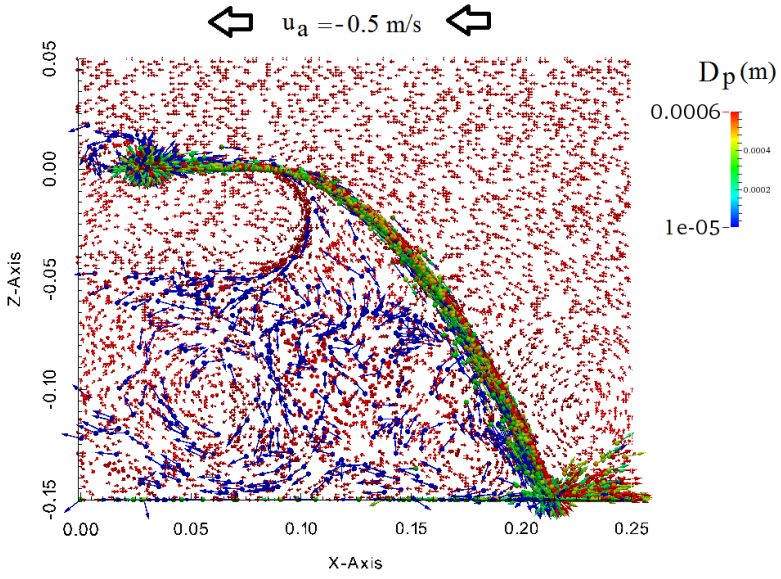

Figure 6.31: The distribution of the dust around the conveyor for $u_a = -0.5\,m/s$ at t=4 *sec.*

6.6.6 The effect of coefficients of restitution

The coefficients of restitution between the particles and also particle-belt was changed according to Table 6.6. Figures 6.32 and 6.33 show the effect of coefficients of restitution on the rate of dust liberation and the profile of discharge trajectory.

As seen in Figure 6.32 , the discharge trajectory of both e_{pp} are almost similar while more particles were liberated from $e_{pp} = 0.90$ compared to $e_{pp} = 0.10$. It can be interpreted by the fact that at high e_{pp}, small particles have more energy to be separated from the other particles. The same thing happened when e_{pb} increase from 0.10 to 0.90 (see Figure 6.33). Consequently, the coefficients of restitution do not have a significant effect on the discharge trajectory while they can increase the rate of dust liberation at the transfer point of a belt conveyor.

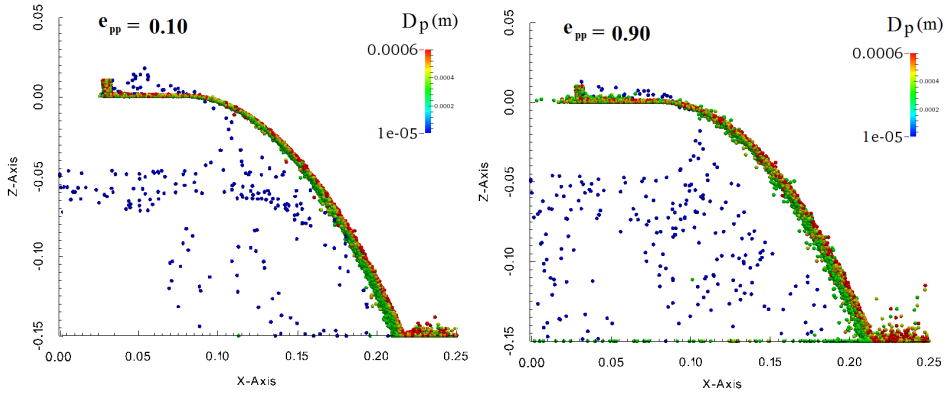

Figure 6.32: The effect of e_{pp} on the profile of discharge trajectory and dust liberation from the belt conveyor at t=4 *sec*.

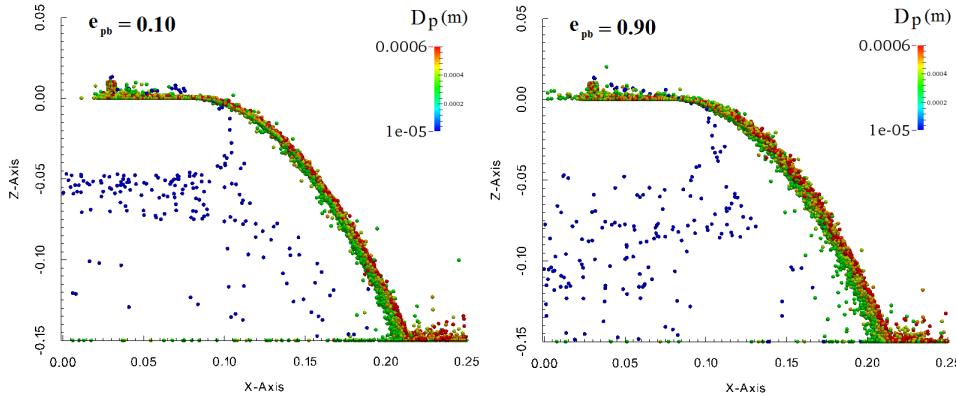

Figure 6.33: The effect of e_{pb} on the profile of discharge trajectory and dust liberation from the belt conveyor at t=4 *sec*.

According to the numerical investigation of this chapter, it was indicated that

the material properties of the belt as well as particles are of importance and affect the design of a transfer point. Also, the viscous effect play an important role in the separation of fine particles from the discharge trajectory of a belt conveyor which should be added into the design factors of the transfer point. The direction and speed of the airflow will intensify the trajectory segregation and it is important when a transfer point is located in the open terminal without any cover or wind protection equipment. Therefore, recognition of the position of low pressure regions is a key factor in determining the location of the dust removal systems. The density and size of material obviously are important factors and their effect on the dust liberation was shown in this chapter.

As final result, it is concluded that the physical properties of materials and belt conveyor, the effect of surrounding air, and the working conditions of the belt conveyor are the important factors that should be considered in the design of the transfer chute of a belt conveyor. The CFD-DEM model that was utilized in this study is successfully validated at the different conditions and it can be used in the future studies to optimize the design of a belt conveyor along with its equipment.

6.7 Conclusions

The discharge trajectory of sand particles was experimentally and numerically studied and the effective factors that should be considered in the design of a transfer point were investigated. On the basis of the results of this study, the following can be concluded:

1. The validated CFD-DEM model is reliable and accurate and can be used in modelling the discharge trajectory of sand particles at different states of the belt conveyor. In addition, it can be used as a design tool in studying the dust liberation at the transfer point of the belt conveyor.

2. It was shown that the CFD-DEM model is able to accurately determine the trajectory of sand particles that collided with the impact plates with different inclination angles. In addition, the discharge trajectory of materials at the different inclination angles of the belt conveyor was accurately determined by the model.

3. It was indicated that the dust can be liberated from the main trajectory due to the different factors such as the trajectory segregation, elutriation segregation, and the viscous effect close to the belt conveyor. Also, the properties of the belt and material can intensify the rate of dust liberation at the transfer point of a belt conveyor. Consequently, the material properties as well as the mentioned factors were considered as the design factors in this study.

4. The relation between the particle size and the discharge trajectory was investigated in this study. It was observed that the drag force has an inverse relation with the square of the particle diameter ($f_d \propto {}^1/_{{D_p}^2}$) in the Stokes regimes and $f_d \propto {}^1/_{D_p}$ in the Newton's region. The simulation results illustrated this effect in a way that the small particles were located at the left side of discharge trajectory when the speed of belt conveyor was in the positive direction of x-axis.

5. Particles with sizes less than $10\,\mu m$ are carried with the belt conveyor because the viscous force is the dominant factor at Stokes region ($Re_p < 0.5$). Due to the strong viscous effect at the boundary layer of the belt, the fine particles stuck to the belt even after all other particles left the belt at the transfer point. Accordingly, the viscous effect is the other important factor which affects the rate of dust liberation at the transfer point of a belt conveyor.

6. The speed and direction of the airflow have a considerable effect on the rate of dust liberation. The airflow with opposite direction from the belt speed will increase the trajectory segregation which leads to an increase in the rate of dust liberation at the transfer points.

7. Particles with low density are under a larger influence of the drag force compared to the high density particles. It was shown by the simulation that particles with lower density travel less than the high density materials.

8. The coefficients of restitution, e_{pp} and e_{pb}, do not have a significant effect on the profile of discharge trajectory while they can increase the rate of dust liberation at the transfer point of a belt conveyor.

9. The success of the CFD-DEM model was shown again based on the experimental data at the different conditions. This model can be used in the future studies to optimize the design of a belt conveyor along with its equipment for reducing the rate of dust liberation.

Bibliography

[1] C. Turpin and J. L. Harion, "Numerical modeling of flow structures over various flat-topped stockpiles height: Implications on dust emissions," *Atmospheric Environment*, vol. 43, no. 35, pp. 5579–5587, nov 2009.

[2] B. Blocken, "50 years of Computational Wind Engineering: Past, present and future," *Journal of Wind Engineering and Industrial Aerodynamics*, vol. 129, pp. 69–102, jun 2014.

[3] K. Ashrafi, M. Kalhor, M. Shafie-Pour, and V. Esfahanian, "Numerical simulation of aerodynamic suspension of particles during wind erosion," *Environmental Earth Sciences*, vol. 74, no. 2, pp. 1569–1578, feb 2015.

[4] T. Badr and J.-L. Harion, "Effect of aggregate storage piles configuration on dust emissions," *Atmospheric Environment*, vol. 41, no. 2, pp. 360–368, jan 2007.

[5] J. Toraño, R. Rodriguez, I. Diego, J. Rivas, and A. Pelegry, "Influence of the pile shape on wind erosion CFD emission simulation," *Applied Mathematical Modelling*, vol. 31, no. 11, pp. 2487–2502, nov 2007.

[6] J. Xuan, "Turbulence factors for threshold velocity and emission rate of atmospheric mineral dust," *Atmospheric Environment*, vol. 38, no. 12, pp. 1777–1783, apr 2004.

[7] B. Furieri, J. L. Harion, M. Milliez, S. Russeil, and J. M. Santos, "Numerical modelling of aeolian erosion over a surface with non-uniformly distributed roughness elements," *Earth Surface Processes and Landforms*, vol. 39, no. 2, pp. 156–166, feb 2014.

[8] A. D. Ferreira and R. A. Oliveira, "Wind erosion of sand placed inside a rectangular box," *Journal of Wind Engineering and Industrial Aerodynamics*, vol. 97, no. 1, pp. 1–10, jan 2009.

[9] A. D. Ferreira, A. B. Farimani, and A. C. M. Sousa, "Numerical and experimental analysis of wind erosion on a sinusoidal pile," *Environmental Fluid Mechanics*, vol. 11, no. 2, pp. 167–181, apr 2010.

[10] R. Faria, A. D. Ferreira, J. L. Sismeiro, J. C. Mendes, and A. C. M. Sousa, "Wind tunnel and computational study of the stoss slope effect on the aeolian erosion of transverse sand dunes," *Aeolian Research*, vol. 3, no. 3, pp. 303–314, dec 2011.

[11] A. B. Farimani, A. D. Ferreira, and A. C. M. Sousa, "Computational modeling of the wind erosion on a sinusoidal pile using a moving boundary method," *Geomorphology*, vol. 130, no. 3-4, pp. 299–311, jul 2011.

[12] B. Furieri, J. M. Santos, S. Russeil, and J.-L. Harion, "Aeolian erosion of storage piles yards: contribution of the surrounding areas," *Environmental Fluid Mechanics*, vol. 14, no. 1, pp. 51–67, jun 2013.

[13] I. Diego, A. Pelegry, S. Torno, J. Toraño, and M. Menendez, "Simultaneous CFD evaluation of wind flow and dust emission in open storage piles," *Applied Mathematical Modelling*, vol. 33, no. 7, pp. 3197–3207, jul 2009.

[14] T. Allen, *Powder Sampling and Particle Size Determination.* Elsevier Science, 2003.

[15] D. B. Hastie, P. W. Wypych, and P. C. Arnold, "Influences on the Prediction of Conveyor Trajectory Profiles," *Particulate Science and Technology*, vol. 28, no. 2, pp. 132–145, mar 2010.

[16] J. Zhang, Z. Hu, W. Ge, Y. Zhang, T. Li, and J. Li, "Application of the Discrete Approach to the Simulation of Size Segregation in Granular Chute Flow," *Industrial & Engineering Chemistry Research*, vol. 43, no. 18, pp. 5521–5528, sep 2004.

[17] A. Grima, T. Fraser, D. Hastie, and P. Wypych, "Discrete element modelling: trouble-shooting and optimisation tool for chute design," pp. 1 – 26, 2011.

[18] A. Roberts, "Chute Performance and Design for Rapid Flow Conditions," *Chemical Engineering & Technology*, vol. 26, no. 2, pp. 163–170, feb 2003.

[19] C. W. Benjamin, S. T. Huque, P. Donecker, and J. J. Rozentals, *The Transfer Chute Design Manual: For Conveyor Belt Systems.* Conveyor Transfer Design Pty. Limited, 2010.

[20] P. McIlvenna and R. Mossad, "Two dimensional transfer chute analysis using a continuum method," dec 2003.

[21] P. Witt, K. Carey, and T. Nguyen, "Prediction of dust loss from conveyors using computational fluid dynamics modelling," *Applied Mathematical Modelling*, vol. 26, no. 2, pp. 297–309, feb 2002.

[22] F. Kessler and M. Prenner, "DEMâĂŞSimulation of Conveyor Transfer Chutes," *FME Transactions*, 2009.

[23] D. Hastie and P. Wypych, "Experimental validation of particle flow through conveyor transfer hoods via continuum and discrete element methods," *Mechanics of Materials*, vol. 42, no. 4, pp. 383–394, apr 2010.

[24] X. Chen, C. Wheeler, T. Donohue, and A. Roberts, "Investigation of Belt Conveyor Transfer Chute Configurations to Reduce Dust Generation Using CFD Modeling," *Applied Mechanics and Materials*, vol. 26-28, pp. 1126–1131, jun 2010.

[25] X. L. Chen, C. A. Wheeler, T. J. T. J. Donohue, R. McLean, and A. A. W. a. W. Roberts, "Evaluation of dust emissions from conveyor transfer chutes using experimental and CFD simulation," *International Journal of Mineral Processing*, vol. 110-111, pp. 101–108, jul 2012.

[26] C. Wheeler and X. Chen, "Computational Fluid Dynamics (CFD) modelling of transfer chutes: a study of the influence of model parameters," *Chemical Engineering Science*, vol. 95, pp. 194–202, may 2013.

[27] X. Chen and C. Wheeler, "Computational Fluid Dynamics (CFD) modelling of transfer chutes: Assessment of viscosity, drag and turbulence models," *International Journal of Multiphase Flow*, vol. 69, pp. 42–53, mar 2015.

[28] A. Katterfeld, T. J. Donohue, and C. A. Wheeler, "Simulation based dust predication of transfer chutes," 2010.

[29] S. M. Derakhshani, D. L. Schott, and G. Lodewijks, "Modeling Dust Liberation at the Belt Conveyor Transfer Point With CFD and DEM," in *11th International Congress on Bulk Materials Storage, Handling and Transportation*, no. July, Newcastle, Australia, 2013.

[30] O. D. Neikov, I. B. Murashova, N. A. Yefimov, S. Naboychenko, I. B. Mourachova, V. G. Gopienko, I. V. Frishberg, and D. V. Lotsko, *Handbook of Non-Ferrous Metal Powders: Technologies and Applications*, ser. Handbook of Non-ferrous Metal Powders: Technologies and Applications. Elsevier Science, 2009.

[31] J. M. N. T. Gray, P. Gajjar, and P. Kokelaar, "Particle-size segregation in dense granular avalanches," *Comptes Rendus Physique*, vol. 16, no. 1, pp. 73–85, jan 2015.

[32] M. J. Rhodes, *Principles of powder technology.* New York, NY (USA); John Wiley and Sons Inc., 1990.

[33] M. Rhodes, *Introduction to Particle Technology.* Wiley, 2008.

[34] M. Combarros Garcia, H. Feise, S. Strege, and A. Kwade, "Segregation in heaps and silos: Comparison between experiment, simulation and continuum model," *Powder Technology*, oct 2015.

[35] C. Lin, Y. Yen, and J. Miller, "Plant-site evaluations of the OPSA system for on-line particle size measurement from moving belt conveyors," *Minerals Engineering*, vol. 13, no. 8-9, pp. 897–909, aug 2000.

[36] T. Allen, *Particle size measurement*, ser. Powder Technology Series. Springer US, 2013.

[37] J. M. N. T. Gray, J. Goddard, P. Giovine, and J. T. Jenkins, "Particle size segregation in granular avalanches: A brief review of recent progress," in *IUTAM-ISIMM Symposium on Mathematical Modeling and Physical Instances of Granular Flows*, vol. 1227, no. 1. AIP Publishing, may 2010, pp. 343–362.

[38] Y. Fan, P. B. Umbanhowar, J. M. Ottino, and R. M. Lueptow, "Kinematics of monodisperse and bidisperse granular flows in quasi-two-dimensional bounded heaps," *Proceedings of the Royal Society A: Mathematical, Physical and Engineering Sciences*, vol. 469, no. 2157, pp. 20 130 235–20 130 235, jul 2013.

[39] R. Ansart, A. D. Ryck, and J. A. Dodds, "Dust emission in powder handling: Free falling particle plume characterisation," *Chemical Engineering Journal*, vol. 152, no. 2-3, pp. 415–420, oct 2009.

[40] R. H. Naylor, "Galileo's Theory of Projectile Motion on JSTOR," *Isis*, vol. 71, no. 4, pp. 550–570, 1980.

[41] W. J. Stronge, *Impact Mechanics*. Cambridge University Press, 2004.

[42] A. H. Cheng and D. T. Cheng, "Heritage and early history of the boundary element method," *Engineering Analysis with Boundary Elements*, vol. 29, no. 3, pp. 268–302, mar 2005.

[43] K. Iwashita and M. Oda, "Rolling Resistance at Contacts in Simulation of Shear Band Development by DEM," *Journal of Engineering Mechanics*, vol. 124, no. 3, pp. 285–292, mar 1998.

[44] P. Ashayer, *Application of Rigid Body Impact Mechanics and Discrete Element Modeling to Rockfall Simulation*, ser. Canadian theses. University of Toronto (Canada), 2007.

CHAPTER

7

Conclusions and Recommendations

This thesis focused on the modelling of dust liberation at the transfer point of a belt conveyor, wherein the factors that affect in the design of a transfer point have particularly been studied. As a concluding chapter, firstly, the main conclusions of this thesis are presented and the related research questions answered. Secondly, some recommendations are proposed to bring the outcomes of this research closer to the industrial applications.

7.1 Conclusions

Three main research questions of this thesis were formulated in Chapter 1 to support the process of studying dust liberation at the transfer point of a belt conveyor. In order to investigate this phenomenon, the numerical method that can be employed as a tool in studying the dust liberation in bulk material handling systems was selected in Chapter 2. Chapter 3, 4 and 5 focused on the calibration, verification, and validation of the selected numerical method for the application of dust liberation modelling. Chapter 6 investigated the factors that should be considered in the design of the transfer point of a belt conveyor.

The main research questions of this thesis are answered as follows:

"1. What numerical method can be employed as a tool in studying the dust liberation in bulk material handling systems?"

The most popular numerical approaches that were widely used in modelling the dust liberation in bulk material handling systems were reviewed to find an answer for the first research question of this thesis. The parameters that influence the rate of dust liberation from bulk material handling systems, for instance from a belt conveyor system, are the physical properties of particles, the inter-particle interactions, and the particle-equipment collisions. These parameters, as well as the computational cost of the numerical technique, were regarded as the most important criteria in the selection of numerical method in this study.

The unresolved CFD model was employed to simulate the fluid phase while more detailed information about the particle phase such as position and velocity of particles were determined with the DEM model. A number of advantages of the CFD-DEM coupling method compared to the other numerical methods are the lower computational effort than the other coupled methods, the ability to determine the microscopic properties of the materials, modelling the inter-particles and particle-equipment collisions, improving the accuracy of airflow field simulation and having further details about the particle phase.

Consequently, the CFD-DEM coupling method was selected as the proper technique for modelling the dust liberation at the transfer point of a belt conveyor.

"2. How to assess the validation of the selected numerical method for the application of dust liberation modelling?"

Different case studies such as the Single Particle Sedimentation (SPS), the hourglass, and the fluidized bed were experimentally and numerically investigated to investigate the validity of the CFD-DEM model for a dense regime of particle flow at a low and high rate of momentum exchange between the particle and fluid phases.

2.1 The SPS: According to the grid dependency analysis, the maximum ratio of the particle diameter to the CFD cell size ($D_p/\Delta x$) was determined equal to 0.5. This ratio along with the divided voidage model should be used where the ratio of the domain width to the particle diameter W/D_p is larger than 10. The grid dependency analysis indicated that the big particle voidage model together with $D_p/\Delta x = 4$ can be utilized for $W/D_p > 5$ in the CFD-DEM model where the divided voidage is not applicable. The numerical benchmarks indicated that the CFD-DEM results obtained with the Gidaspow drag force model are more accurate than the other drag force models. Also, the coupling interval of 100 times the DEM time step led to sufficiently fast simulation and accurate enough results in the SPS modelling.

Consequently, the CFD-DEM model can accurately determine the terminal velocity of a settling particle in a dilute regime of particle flow at a low rate of momentum exchange between the particle and fluid phases.

2.2 The hourglass: The hourglass was modelled to determine the microscopic

properties ($\mu_{r,pp}$ and $\mu_{s,pp}$) and macroscopic properties (Angle of Repose and discharging time of sand from the hourglass) of quartz sand. The uncertainty of $\pm 1.1^\circ$ and $\pm 0.1\,sec$ was observed for the AoR and discharging time in the experimental measurements.

It was experimentally observed that the AoR and discharging time in the hourglass test with 25 g of sand and neck diameter of 5 mm are 41.6° and $6.6\,s$, respectively. The DEM was employed to determine the $\mu_{r,pp}$ and $\mu_{s,pp}$ between the sand particles without considering the effect of air on the macroscopic properties. The simulation results indicated that the DEM results are in agreement with the experimental results in the cases that the $\mu_{r,pp}$ and $\mu_{s,pp}$ are equal to 0.30 and 0.52 in the DEM model. Also, the hourglass was modelled with CFD-DEM model in a way that the effect of air on the calibration process was considered. It was observed that the $\mu_{r,pp}$ and $\mu_{s,pp}$ of 0.3 and 0.49 will match the experimental values of the AoR and discharging time.

Through modelling a rectangular container of sand particles, it was indicated that a slice of the whole domain with the width (W) of 32 times the particle diameter (D_p) represents the behaviour of the middle plane in the real domain where the wall boundary condition is applied on the front and rare walls in the DEM simulation. Moreover, similar results were obtained when the periodic boundary condition with the W/D_p of 4 was used in the DEM model while the computational time of the DEM simulation reduced significantly.

Consequently, the CFD-DEM model with its sub-models and parameters are also applicable in modelling a dense regime of particle flow when the rate of momentum exchange between the particle and fluid phases was low.

2.3 The fluidized bed: The CFD-DEM model was assessed through modelling a fluidized bed of sand particles at different airflow rates. Grid dependency analysis indicated that utilization of uniform CFD cell smaller than $5\,mm$ does not have a significant effect on the accuracy of CFD-DEM results. In addition, it was shown that the two-dimensional CFD grid can be employed instead of three-dimensional grid in the CFD simulations. Also, the coefficients of rolling and sliding friction between the Plexiglass wall and sand particles were numerically and experimentally determined to be 0.30 and 0.32, respectively and the Coefficient of Restitution (CoR) between the sand particles was found equal to $e_{pp} = 0.9$.

It was seen that the penetration has a significant effect before the MFV and its effect disappears for velocities beyond the MFV due to the mixing process. It was observed that utilization of the MSP instead of the PSP in modelling the fluidized bed of sand will result in a different value for the MFV. Also, the front and back walls of the fluidized bed can be replaced with the periodic boundary condition instead of the wall boundary condition in the DEM model to enhance the computational effort of the DEM model.

Consequently, the CFD-DEM model along with its parameters and sub-models can be used in simulating a dense regime of particle flow with a low or high rate of

momentum exchange between the particle and fluid phases such as modelling the dust liberation at the transfer point of belt conveyors.

"3. Which factors should be considered in the design of the transfer point of a conveyor?"

The CFD-DEM model was successfully evaluated based on the experimental data at the different conditions. This model can be used in the future studies to optimize the design of a belt conveyor along with its equipment for reducing the rate of dust liberation. It was shown that the CFD-DEM model is able to accurately determine the trajectory of sand particles that collided with the impact plates with different inclination angles. In addition, the discharge trajectory of materials at the different inclination angles of the belt conveyor and different speeds of the belt was accurately determined by the model. It was shown that the speed and direction of the airflow has a considerable effect on the rate of dust liberation. In other words, the airflow with opposite direction from the belt speed will increase the trajectory segregation which leads to an increase in the rate of dust liberation at the transfer points.

It was observed that the properties of the belt and material can intensify the rate of dust liberation at the transfer point of a belt conveyor. Consequently, the material properties as well as the particle properties should be considered in the design of a transfer point. Therefore, the relation between the particle size and the discharge trajectory was investigated. It was seen that the drag force has an inverse relation with the square of the particle diameter ($f_d \propto {}^1/_{{D_p}^2}$) in the Stokes regimes and $f_d \propto {}^1/_{D_p}$ in the Newton's region. The simulation results illustrated this effect in a way that the small particles was located at the left side of discharge trajectory when the speed of belt conveyor was in the positive direction of x-axis. Particles with sizes less than $10\,\mu m$ are carried with the belt conveyor because the viscous force is the dominant factor at Stokes region ($Re_p < 0.5$). Due to the strong viscous effect at the boundary layer of the belt, the fine particles stuck into the belt even after all other particles left the belt at the transfer point. Therefore, recognition of the position of low pressure regions is a key factor in determining the location of the dust removal systems. Accordingly, the viscous effect is the other important factor which affects on the rate of dust liberation at the transfer point of a belt conveyor.

Particles with low density are more under the influence of the drag force compared to the particles with high density. This issue is due to the difference between the terminal velocities of with different densities. It was shown by the simulation that particles with lower density travel less than the high density materials. The other factor that was investigated is the coefficients of restitution, e_{pp} and e_{pb}. It was seen that the coefficients of restitution do not have a significant effect on the profile of discharge trajectory while they can increase the rate of dust liberation at the transfer point of a belt conveyor.

Finally, it was concluded that the physical properties of materials and belt conveyor, the effect of surrounding air, and the working conditions of the belt conveyor are the important factors that affect the design of the transfer point of a

belt conveyor.

7.2 Recommendations for future research

It is recommended to further investigate the following subjects to bring the outcomes of this research closer to the industrial applications where dust liberation play an important role.

1. Modelling a real-size transfer point will provide more detail information about the effects of conveyor components on the airflow pattern around a belt conveyor. In addition, this makes it possible to investigate the effect of airflow in the various directions around a belt conveyor.

2. The vibration of a belt conveyor system can lead to the pre-segregation of material. This issue can intensify the dust liberation from a belt conveyor.

3. Studying the effect of utilizing a closed chamber around a belt conveyor set-up and investigating the effect of its design on the pressure distribution inside the chamber.

4. Assessing the effect of a transfer chute and its configuration (impact plate, hood, spoon, and scraper) on the rate of dust liberation and dispersion in the environment.

5. Fine materials can carry with the return belt and disperse in the surrounding environment. The belt material as well as the shape of the belt surface are two important factors that affect the dust liberation and these factors can be considered in the future researches.

6. Dust liberation from cohesive materials and investigating the reliability of the cohesive models in the DEM model are interesting subjects for future studies.

7. Modelling the pressure domain around a belt conveyor for determining the best place for the dust removal systems.

Appendix

A

Experimental Data of the Fluidized Bed Test

Table A.1: Laboratory conditions and measured experimental data (3 times) of the empty fluidized bed.

Date	3-Oct-2014	Range	0 to 100 [%]	0 to 100 [l/min]
Air temperature	18°C	Increments	5 l/min	
Sand mass	0 g	Output	Pressure drop	
Input	Airflow	Range	0 to 10 [V]	0 to 200 [mbar]

Measurement 1			Measurement 2			Measurement 3		
Air flow [l/min]	Voltage [V]	Pressure [mbar]	Air flow [l/min]	Voltage [V]	Pressure [mbar]	Air flow [l/min]	Voltage [V]	Pressure [mbar]
0	0	0	0.00	0.00	0.00	0.00	0.00	0.00
4.9	0.13	2.6	4.80	0.13	2.60	4.90	0.13	2.60
9.9	0.27	5.4	9.90	0.26	5.20	9.90	0.26	5.20
15	0.4	8	14.90	0.40	8.00	14.90	0.40	8.00
20.1	0.53	10.6	20.00	0.53	10.60	19.90	0.53	10.60
25.1	0.67	13.4	25.00	0.67	13.40	25.00	0.67	13.40
30.1	0.8	16	30.10	0.80	16.00	29.90	0.80	16.00
35.2	0.94	18.8	35.10	0.94	18.80	35.00	0.94	18.80
40.2	1.08	21.6	40.10	1.08	21.60	39.90	1.08	21.60
45.2	1.23	24.6	45.10	1.22	24.40	45.10	1.23	24.60
50.2	1.37	27.4	50.00	1.36	27.20	50.00	1.37	27.40
55.1	1.52	30.4	55.00	1.52	30.40	55.10	1.52	30.40
60.1	1.67	33.4	60.00	1.67	33.40	60.00	1.67	33.40
65.1	1.83	36.6	65.00	1.83	36.60	65.00	1.83	36.60
70.3	2	40	70.00	1.99	39.80	69.90	1.99	39.80
75	2.16	43.2	75.10	2.16	43.20	75.00	2.16	43.20
80.1	2.33	46.6	80.10	2.34	46.80	79.90	2.33	46.60
84.9	2.51	50.2	85.10	2.52	50.40	85.10	2.52	50.40
90.2	2.71	54.2	90.00	2.71	54.20	90.10	2.70	54.00
95.3	2.92	58.4	95.30	2.91	58.20	95.30	2.92	58.40
100.1	3.11	62.2	100.20	3.12	62.40	100.20	3.12	62.40

Table A.2: Average of the measured data (Table A.1) within an empty fluidized bed.

Air flow $[l/min]$	Air velocity $[m/min]$	Pressure $[mbar]$	Standard Devision $[mbar]$
0.00	0.00	0.00	0.00
4.87	1.62	2.60	0.00
9.90	3.30	5.27	0.09
14.93	4.98	8.00	0.00
20.00	6.67	10.60	0.00
25.03	8.34	13.40	0.00
30.03	10.01	16.00	0.00
35.10	11.70	18.80	0.00
40.07	13.36	21.60	0.00
45.13	15.04	24.53	0.09
50.07	16.69	27.33	0.09
55.07	18.36	30.40	0.00
60.03	20.01	33.40	0.00
65.03	21.68	36.60	0.00
70.07	23.36	39.87	0.09
75.03	25.01	43.20	0.00
80.03	26.68	46.67	0.09
85.03	28.34	50.33	0.09
90.10	30.03	54.13	0.09
95.30	31.77	58.33	0.09
100.17	33.39	62.33	0.09

Table A.3: Laboratory conditions and measured experimental data (3 times) of the fluidized bed at the bed height of 100 mm.

Date	3-Oct-2014	Range	0 to 100 [%]	0 to 100 [l/min]
Air temperature	18°C	Increments	5 l/min	
Sand mass	480.88 g	Output	Pressure drop	
Input	Airflow	Range	0 to 10 [V]	0 to 200 [mbar]

Measurement 1			Measurement 2			Measurement 3		
Air flow [l/min]	Voltage [V]	Pressure [mbar]	Air flow [l/min]	Voltage [V]	Pressure [mbar]	Air flow [l/min]	Voltage [V]	Pressure [mbar]
0.00	0.00	0.00	0.00	0.00	0.00	0.00	0.00	0.00
4.90	0.20	4.00	4.90	0.20	4.00	5.10	0.21	4.20
9.90	0.41	8.20	10.00	0.41	8.20	9.90	0.41	8.20
15.10	0.63	12.60	15.10	0.61	12.20	15.20	0.62	12.40
19.90	0.84	16.80	20.00	0.82	16.40	20.10	0.83	16.60
24.90	1.05	21.00	24.90	1.02	20.40	24.90	1.03	20.60
29.90	1.27	25.40	29.90	1.23	24.60	29.90	1.24	24.80
34.90	1.49	29.80	35.00	1.45	29.00	34.90	1.45	29.00
39.90	1.72	34.40	40.00	1.67	33.40	39.90	1.67	33.40
45.00	1.95	39.00	45.00	1.88	37.60	45.00	1.89	37.80
50.20	2.12	42.40	49.90	2.07	41.40	49.90	2.08	41.60
55.00	2.28	45.60	55.00	2.25	45.00	55.00	2.26	45.20
60.00	2.44	48.80	60.00	2.43	48.60	60.00	2.43	48.60
65.00	2.60	52.00	65.10	2.60	52.00	65.20	2.60	52.00
70.00	2.76	55.20	70.00	2.76	55.20	70.10	2.77	55.40
75.10	2.94	58.80	75.20	2.93	58.60	75.10	2.95	59.00
80.00	3.09	61.80	80.10	3.10	62.00	80.00	3.10	62.00
84.90	3.28	65.60	85.30	3.30	66.00	85.00	3.28	65.60
90.20	3.48	69.60	90.20	3.48	69.60	90.00	3.48	69.60
95.30	3.68	73.60	95.30	3.68	73.60	95.00	3.69	73.80
100.10	3.83	76.60	100.10	3.85	77.00	100.30	3.88	77.60
94.70	3.65	73.00	95.10	3.66	73.20	95.10	3.68	73.60
89.90	3.45	69.00	90.00	3.48	69.60	90.10	3.48	69.60
85.00	3.27	65.40	84.80	3.29	65.80	85.00	3.30	66.00
80.00	3.11	62.20	79.80	3.10	62.00	79.90	3.07	61.40
74.90	2.93	58.60	74.80	2.90	58.00	74.70	2.90	58.00
69.80	2.71	54.20	69.50	2.73	54.60	69.70	2.77	55.40
64.70	2.55	51.00	64.70	2.58	51.60	64.70	2.60	52.00
59.80	2.41	48.20	59.70	2.40	48.00	59.90	2.43	48.60
54.80	2.23	44.60	54.90	2.24	44.80	54.60	2.23	44.60
49.80	2.06	41.20	49.90	2.02	40.40	49.90	2.03	40.60
44.80	1.82	36.40	45.00	1.84	36.80	45.10	1.84	36.80
39.70	1.61	32.20	40.10	1.63	32.60	40.20	1.64	32.80
34.80	1.39	27.80	35.00	1.42	28.40	35.20	1.43	28.60
30.10	1.24	24.80	30.00	1.20	24.00	30.10	1.19	23.80
24.90	1.00	20.00	25.00	1.01	20.20	25.10	1.01	20.20
20.10	0.78	15.60	19.90	0.80	16.00	20.00	0.82	16.40
15.00	0.60	12.00	15.00	0.60	12.00	15.00	0.60	12.00
10.00	0.39	7.80	10.00	0.38	7.60	9.90	0.42	8.40
4.70	0.19	3.80	4.90	0.18	3.60	4.70	0.20	4.00
0.00	0.00	0.00	0.00	0.00	0.00	0.00	0.00	0.00

Table A.4: Average of the measured data (Table A.3) at the bed height of 100 mm.

Air flow $[l/min]$	Air velocity $[m/min]$	Pressure $[mbar]$	Corrected pressure $[mbar]$	Standard Devision $[mbar]$
0.00	0.00	0.00	0.00	0.00
4.97	1.66	4.07	1.47	0.09
9.93	3.31	8.20	2.93	0.00
15.13	5.04	12.40	4.40	0.16
20.00	6.67	16.60	6.00	0.16
24.90	8.30	20.67	7.27	0.25
29.90	9.97	24.93	8.93	0.34
34.93	11.64	29.27	10.47	0.38
39.93	13.31	33.73	12.13	0.47
45.00	15.00	38.13	13.60	0.62
50.00	16.67	41.80	14.47	0.43
55.00	18.33	45.27	14.87	0.25
60.00	20.00	48.67	15.27	0.09
65.10	21.70	52.00	15.40	0.00
70.03	23.34	55.27	15.40	0.09
75.13	25.04	58.80	15.60	0.16
80.03	26.68	61.93	15.27	0.09
85.07	28.36	65.73	15.40	0.19
90.13	30.04	69.60	15.47	0.00
95.20	31.73	73.67	15.33	0.09
100.17	33.39	77.07	14.73	0.41
94.97	31.66	73.27	14.93	0.25
90.00	30.00	69.40	15.27	0.28
84.93	28.31	65.73	15.40	0.25
79.90	26.63	61.87	15.20	0.34
74.80	24.93	58.20	15.00	0.28
69.67	23.22	54.73	14.87	0.50
64.70	21.57	51.53	14.93	0.41
59.80	19.93	48.27	14.87	0.25
54.77	18.26	44.67	14.27	0.09
49.87	16.62	40.73	13.40	0.34
44.97	14.99	36.67	12.13	0.19
40.00	13.33	32.53	10.93	0.25
35.00	11.67	28.27	9.47	0.34
30.07	10.02	24.20	8.20	0.43
25.00	8.33	20.13	6.73	0.09
20.00	6.67	16.00	5.40	0.33
15.00	5.00	12.00	4.00	0.00
9.97	3.32	7.93	2.67	0.34
4.77	1.59	3.80	1.20	0.16
0.00	0.00	0.00	0.00	0.00

Table A.5: Laboratory conditions and measured experimental data (3 times) of the fluidized bed at the bed height of 150 mm.

Date	3-Oct-2014	Range	0 to 100 [%]	0 to 100 [l/min]
Air temperatureerature	18°C	Increments	5 l/min	
Sand mass	663.603 g	Output	Pressure drop	
Input	Airflow	Range	0 to 10 [V]	0 to 200 [mbar]

Measurement 1			Measurement 2			Measurement 3		
Air flow [l/min]	Voltage [V]	Pressure [mbar]	Air flow [l/min]	Voltage [V]	Pressure [mbar]	Air flow [l/min]	Voltage [V]	Pressure [mbar]
0.00	0.00	0.00	0.00	0.00	0.00	0.00	0.00	0.00
4.80	0.23	4.60	5.10	0.24	4.80	5.10	0.24	4.80
10.00	0.48	9.60	10.10	0.47	9.40	9.90	0.47	9.40
15.00	0.72	14.40	15.10	0.71	14.20	15.20	0.72	14.40
19.90	0.96	19.20	19.90	0.94	18.80	20.00	0.95	19.00
24.90	1.21	24.20	24.90	1.19	23.80	25.10	1.20	24.00
29.90	1.46	29.20	29.90	1.43	28.60	30.00	1.44	28.80
35.00	1.71	34.20	35.10	1.68	33.60	35.10	1.69	33.80
39.90	1.97	39.40	39.90	1.92	38.40	40.00	1.93	38.60
45.00	2.23	44.60	45.00	2.17	43.40	45.10	2.18	43.60
49.90	2.48	49.60	50.10	2.38	47.60	50.00	2.39	47.80
55.00	2.60	52.00	55.10	2.58	51.60	55.10	2.58	51.60
60.10	2.88	57.60	59.90	2.76	55.20	59.90	2.76	55.20
65.20	2.96	59.20	65.30	2.94	58.80	65.10	2.97	59.40
70.40	3.12	62.40	70.00	3.11	62.20	70.30	3.12	62.40
75.10	3.27	65.40	75.10	3.26	65.20	75.00	3.27	65.40
80.10	3.44	68.80	80.00	3.45	69.00	80.00	3.46	69.20
85.20	3.65	73.00	84.90	3.65	73.00	85.00	3.65	73.00
90.20	3.82	76.40	90.00	3.85	77.00	90.00	3.84	76.80
95.00	4.05	81.00	95.10	4.02	80.40	95.20	4.02	80.40
100.10	4.22	84.40	100.20	4.25	85.00	100.20	4.30	86.00
95.00	4.02	80.40	95.00	4.03	80.60	95.10	4.03	80.60
90.00	3.79	75.80	89.80	3.83	76.60	90.00	3.83	76.60
84.90	3.64	72.80	84.90	3.65	73.00	84.90	3.66	73.20
79.90	3.48	69.60	79.80	3.46	69.20	79.80	3.48	69.60
75.10	3.29	65.80	74.90	3.27	65.40	74.70	3.30	66.00
70.00	3.09	61.80	70.10	3.09	61.80	69.60	3.10	62.00
65.00	2.92	58.40	65.10	2.93	58.60	64.60	2.93	58.60
60.10	2.75	55.00	60.20	2.76	55.20	59.80	2.76	55.20
55.20	2.57	51.40	55.00	2.57	51.40	55.10	2.59	51.80
50.10	2.34	46.80	50.10	2.35	47.00	50.00	2.35	47.00
45.10	2.10	42.00	45.10	2.11	42.20	45.20	2.12	42.40
40.00	1.86	37.20	40.10	1.87	37.40	40.10	1.88	37.60
35.10	1.62	32.40	35.20	1.64	32.80	35.20	1.65	33.00
30.10	1.39	27.80	30.10	1.40	28.00	30.00	1.41	28.20
25.00	1.16	23.20	25.10	1.16	23.20	25.10	1.18	23.60
20.00	0.92	18.40	20.00	0.93	18.60	20.00	0.94	18.80
14.90	0.69	13.80	14.90	0.69	13.80	15.00	0.70	14.00
9.80	0.45	9.00	10.00	0.46	9.20	9.90	0.46	9.20
5.00	0.23	4.60	4.80	0.22	4.40	5.00	0.23	4.60
0.00	0.00	0.00	0.00	0.00	0.00	0.00	0.00	0.00

Table A.6: Average of the measured data (Table A.5) at the bed height of 150 mm.

Air flow $[l/min]$	Air velocity $[m/min]$	Pressure $[mbar]$	Corrected pressure $[mbar]$	Standard Devision $[mbar]$
0.00	0.00	0.00	0.00	0.00
5.00	1.67	4.73	2.13	0.09
10.00	3.33	9.47	4.20	0.09
15.10	5.03	14.33	6.33	0.09
19.93	6.64	19.00	8.40	0.16
24.97	8.32	24.00	10.60	0.16
29.93	9.98	28.87	12.87	0.25
35.07	11.69	33.87	15.07	0.25
39.93	13.31	38.80	17.20	0.43
45.03	15.01	43.87	19.33	0.52
50.00	16.67	48.33	21.00	0.90
55.07	18.36	51.73	21.33	0.19
59.97	19.99	56.00	22.60	1.13
65.20	21.73	59.13	22.53	0.25
70.23	23.41	62.33	22.47	0.09
75.07	25.02	65.33	22.13	0.09
80.03	26.68	69.00	22.33	0.16
85.03	28.34	73.00	22.67	0.00
90.07	30.02	76.73	22.60	0.25
95.10	31.70	80.60	22.27	0.28
100.17	33.39	85.13	22.80	0.66
95.03	31.68	80.53	22.20	0.09
89.93	29.98	76.33	22.20	0.38
84.90	28.30	73.00	22.67	0.16
79.83	26.61	69.47	22.80	0.19
74.90	24.97	65.73	22.53	0.25
69.90	23.30	61.87	22.00	0.09
64.90	21.63	58.53	21.93	0.09
60.03	20.01	55.13	21.73	0.09
55.10	18.37	51.53	21.13	0.19
50.07	16.69	46.93	19.60	0.09
45.13	15.04	42.20	17.67	0.16
40.07	13.36	37.40	15.80	0.16
35.17	11.72	32.73	13.93	0.25
30.07	10.02	28.00	12.00	0.16
25.07	8.36	23.33	9.93	0.19
20.00	6.67	18.60	8.00	0.16
14.93	4.98	13.87	5.87	0.09
9.90	3.30	9.13	3.87	0.09
4.93	1.64	4.53	1.93	0.09
0.00	0.00	0.00	0.00	0.00

Table A.7: Laboratory conditions and measured experimental data (3 times) of the fluidized bed at the bed height of 200 mm.

Date	9-Oct-2014	Range	0 to 100 [%]	0 to 100 [l/min]
Air temperatureerature	22°C	Increments	5 l/min	
Sand mass	885.88 g	Output	Pressure drop	
Input	Airflow	Range	0 to 10 [V]	0 to 200 [mbar]

Measurement 1			Measurement 2			Measurement 3		
Air flow [l/min]	Voltage [V]	Pressure [mbar]	Air flow [l/min]	Voltage [V]	Pressure [mbar]	Air flow [l/min]	Voltage [V]	Pressure [mbar]
0.00	0.00	0.00	0.00	0.00	0.00	0.00	0.00	0.00
5.10	0.30	6.00	5.00	0.28	5.60	5.00	0.28	5.60
10.10	0.60	12.00	9.80	0.55	11.00	10.00	0.56	11.20
15.10	0.89	17.80	14.90	0.83	16.60	15.00	0.83	16.60
20.10	1.18	23.60	19.80	1.11	22.20	19.80	1.11	22.20
24.80	1.46	29.20	25.00	1.41	28.20	25.00	1.40	28.00
29.80	1.76	35.20	29.80	1.68	33.60	29.90	1.68	33.60
34.90	2.07	41.40	34.90	1.97	39.40	35.00	1.97	39.40
39.90	2.38	47.60	40.00	2.28	45.60	40.00	2.27	45.40
44.90	2.66	53.20	44.90	2.54	50.80	44.90	2.55	51.00
49.90	2.84	56.80	49.90	2.75	55.00	49.90	2.77	55.40
54.90	3.01	60.20	55.00	2.98	59.60	55.00	2.98	59.60
59.90	3.19	63.80	59.90	3.16	63.20	59.90	3.17	63.40
64.90	3.36	67.20	65.10	3.35	67.00	65.20	3.37	67.40
69.80	3.52	70.40	70.10	3.52	70.40	69.90	3.55	71.00
74.90	3.68	73.60	75.00	3.68	73.60	75.10	3.68	73.60
79.90	3.87	77.40	80.00	3.88	77.60	80.00	3.89	77.80
85.00	4.01	80.20	85.20	4.05	81.00	84.90	4.05	81.00
89.80	4.25	85.00	90.30	4.30	86.00	89.80	4.25	85.00
94.90	4.45	89.00	95.20	4.45	89.00	95.00	4.50	90.00
100.10	4.70	94.00	100.00	4.70	94.00	99.90	4.70	94.00
94.90	4.45	89.00	95.00	4.48	89.60	94.90	4.48	89.60
89.90	4.25	85.00	90.00	4.30	86.00	90.10	4.28	85.60
85.00	4.08	81.60	85.20	4.10	82.00	85.10	4.09	81.80
80.20	3.85	77.00	80.10	3.88	77.60	80.00	3.88	77.60
75.00	3.68	73.60	75.00	3.68	73.60	75.00	3.70	74.00
70.00	3.50	70.00	70.00	3.50	70.00	69.90	3.53	70.60
65.00	3.32	66.40	65.00	3.34	66.80	64.70	3.34	66.80
60.00	3.16	63.20	59.90	3.15	63.00	60.00	3.15	63.00
55.10	2.96	59.20	54.80	2.96	59.20	55.10	2.95	59.00
50.10	2.71	54.20	49.80	2.69	53.80	50.10	2.72	54.40
45.00	2.44	48.80	44.80	2.43	48.60	45.10	2.45	49.00
40.00	2.17	43.40	39.80	2.15	43.00	40.10	2.17	43.40
35.00	1.90	38.00	34.80	1.89	37.80	35.10	1.90	38.00
29.90	1.63	32.60	29.80	1.62	32.40	30.10	1.64	32.80
25.00	1.36	27.20	25.10	1.36	27.20	25.00	1.36	27.20
20.00	1.09	21.80	20.10	1.09	21.80	20.00	1.09	21.80
14.90	0.81	16.20	15.10	0.81	16.20	15.00	0.81	16.20
9.90	0.53	10.60	10.30	0.55	11.00	9.90	0.53	10.60
5.00	0.27	5.40	5.20	0.28	5.60	5.00	0.26	5.20
0.00	0.00	0.00	0.00	0.00	0.00	0.00	0.00	0.00

Table A.8: Average of the measured data (Table A.7) at the bed height of 200 mm.

Air flow $[l/min]$	Air velocity $[m/min]$	Pressure $[mbar]$	Corrected pressure $[mbar]$	Standard Devision $[mbar]$
0.00	0.00	0.00	0.00	0.00
5.03	1.68	5.73	3.13	0.19
9.97	3.32	11.40	6.13	0.43
15.00	5.00	17.00	9.00	0.57
19.90	6.63	22.67	12.07	0.66
24.93	8.31	28.47	15.07	0.52
29.83	9.94	34.13	18.13	0.75
34.93	11.64	40.07	21.27	0.94
39.97	13.32	46.20	24.60	0.99
44.90	14.97	51.67	27.13	1.09
49.90	16.63	55.73	28.40	0.77
54.97	18.32	59.80	29.40	0.28
59.90	19.97	63.47	30.07	0.25
65.07	21.69	67.20	30.60	0.16
69.93	23.31	70.60	30.73	0.28
75.00	25.00	73.60	30.40	0.00
79.97	26.66	77.60	30.93	0.16
85.03	28.34	80.73	30.40	0.38
89.97	29.99	85.33	31.20	0.47
95.03	31.68	89.33	31.00	0.47
100.00	33.33	94.00	31.67	0.00
94.93	31.64	89.40	31.07	0.28
90.00	30.00	85.53	31.40	0.41
85.10	28.37	81.80	31.47	0.16
80.10	26.70	77.40	30.73	0.28
75.00	25.00	73.73	30.53	0.19
69.97	23.32	70.20	30.33	0.28
64.90	21.63	66.67	30.07	0.19
59.97	19.99	63.07	29.67	0.09
55.00	18.33	59.13	28.73	0.09
50.00	16.67	54.13	26.80	0.25
44.97	14.99	48.80	24.27	0.16
39.97	13.32	43.27	21.67	0.19
34.97	11.66	37.93	19.13	0.09
29.93	9.98	32.60	16.60	0.16
25.03	8.34	27.20	13.80	0.00
20.03	6.68	21.80	11.20	0.00
15.00	5.00	16.20	8.20	0.00
10.03	3.34	10.73	5.47	0.19
5.07	1.69	5.40	2.80	0.16
0.00	0.00	0.00	0.00	0.00

Table A.9: Laboratory conditions and measured experimental data (3 times) of the fluidized bed at the bed height of 250 mm.

Date	9-Oct-2014	Range	0 to 100 [%]	0 to 100 [l/min]	
Air temperatureerature	18°C	Increments	5 l/min		
Sand mass	1071.632 g	Output	Pressure drop		
Input	Airflow	Range	0 to 10 [V]	0 to 200 [mbar]	

Measurement 1			Measurement 2			Measurement 3		
Air flow [l/min]	Voltage [V]	Pressure [mbar]	Air flow [l/min]	Voltage [V]	Pressure [mbar]	Air flow [l/min]	Voltage [V]	Pressure [mbar]
0.00	0.00	0.00	0.00	0.00	0.00	0.00	0.00	0.00
4.70	0.30	6.00	4.80	0.28	5.60	4.80	0.28	5.60
10.20	0.65	13.00	9.80	0.60	12.00	9.80	0.58	11.60
15.10	0.98	19.60	15.00	0.93	18.60	15.00	0.91	18.20
20.10	1.31	26.20	19.90	1.25	25.00	19.90	1.22	24.40
25.20	1.65	33.00	24.90	1.57	31.40	24.90	1.54	30.80
30.00	1.97	39.40	29.80	1.89	37.80	29.90	1.86	37.20
35.00	2.32	46.40	34.90	2.22	44.40	35.00	2.18	43.60
39.90	2.65	53.00	39.80	2.54	50.80	40.00	2.51	50.20
44.80	2.94	58.80	44.90	2.83	56.60	45.00	2.81	56.20
49.90	3.13	62.60	49.80	3.04	60.80	50.00	3.04	60.80
55.00	3.32	66.40	55.00	3.26	65.20	55.10	3.27	65.40
60.10	3.48	69.60	59.80	3.45	69.00	60.10	3.46	69.20
65.00	3.65	73.00	64.90	3.64	72.80	65.20	3.64	72.80
70.00	3.83	76.60	69.90	3.85	77.00	70.00	3.82	76.40
75.10	4.02	80.40	75.20	3.98	79.60	75.00	4.00	80.00
80.10	4.20	84.00	80.00	4.28	85.60	80.00	4.25	85.00
85.20	4.40	88.00	85.10	4.41	88.20	85.00	4.38	87.60
90.20	4.62	92.40	90.30	4.58	91.60	90.10	4.60	92.00
95.20	4.85	97.00	95.00	4.85	97.00	95.10	4.88	97.60
100.40	4.98	99.60	100.00	5.05	101.00	100.00	5.10	102.00
95.00	4.80	96.00	94.90	4.85	97.00	95.10	4.80	96.00
90.00	4.56	91.20	89.90	4.62	92.40	90.00	4.58	91.60
85.00	4.40	88.00	85.00	4.37	87.40	85.00	4.40	88.00
80.00	4.20	84.00	79.90	4.28	85.60	80.00	4.18	83.60
74.90	4.05	81.00	75.00	3.98	79.60	75.00	4.00	80.00
69.90	3.78	75.60	69.90	3.80	76.00	69.90	3.77	75.40
64.80	3.66	73.20	64.80	3.64	72.80	64.80	3.63	72.60
59.70	3.44	68.80	60.00	3.44	68.80	59.90	3.43	68.60
54.90	3.24	64.80	54.80	3.23	64.60	55.00	3.23	64.60
50.00	3.01	60.20	49.70	2.98	59.60	50.00	2.97	59.40
45.00	2.70	54.00	44.80	2.67	53.40	44.90	2.66	53.20
40.00	2.40	48.00	39.70	2.36	47.20	39.80	2.35	47.00
35.10	2.10	42.00	34.80	2.07	41.40	34.90	2.07	41.40
30.00	1.81	36.20	29.80	1.78	35.60	29.60	1.76	35.20
25.00	1.51	30.20	24.70	1.47	29.40	24.80	1.47	29.40
20.00	1.20	24.00	19.80	1.18	23.60	19.80	1.17	23.40
14.80	0.89	17.80	14.90	0.88	17.60	14.80	0.87	17.40
9.70	0.57	11.40	11.90	0.70	14.00	9.70	0.56	11.20
4.70	0.26	5.20	5.00	0.28	5.60	4.70	0.26	5.20
0.00	0.00	0.00	0.00	0.00	0.00	0.00	0.00	0.00

Table A.10: Average of the measured data (Table A.9) at the bed height of 250 mm.

Air flow $[l/min]$	Air velocity $[m/min]$	Pressure $[mbar]$	Corrected pressure $[mbar]$	Standard Devision $[mbar]$
0.00	0.00	0.00	0.00	0.00
4.77	1.59	5.73	3.13	0.19
9.93	3.31	12.20	6.93	0.59
15.03	5.01	18.80	10.80	0.59
19.97	6.66	25.20	14.60	0.75
25.00	8.33	31.73	18.33	0.93
29.90	9.97	38.13	22.13	0.93
34.97	11.66	44.80	26.00	1.18
39.90	13.30	51.33	29.73	1.20
44.90	14.97	57.20	32.67	1.14
49.90	16.63	61.40	34.07	0.85
55.03	18.34	65.67	35.27	0.52
60.00	20.00	69.27	35.87	0.25
65.03	21.68	72.87	36.27	0.09
69.97	23.32	76.67	36.80	0.25
75.10	25.03	80.00	36.80	0.33
80.03	26.68	84.87	38.20	0.66
85.10	28.37	87.93	37.60	0.25
90.20	30.07	92.00	37.87	0.33
95.10	31.70	97.20	38.87	0.28
100.13	33.38	100.87	38.53	0.98
95.00	31.67	96.33	38.00	0.47
89.97	29.99	91.73	37.60	0.50
85.00	28.33	87.80	37.47	0.28
79.97	26.66	84.40	37.73	0.86
74.97	24.99	80.20	37.00	0.59
69.90	23.30	75.67	35.80	0.25
64.80	21.60	72.87	36.27	0.25
59.87	19.96	68.73	35.33	0.09
54.90	18.30	64.67	34.27	0.09
49.90	16.63	59.73	32.40	0.34
44.90	14.97	53.53	29.00	0.34
39.83	13.28	47.40	25.80	0.43
34.93	11.64	41.60	22.80	0.28
29.80	9.93	35.67	19.67	0.41
24.83	8.28	29.67	16.27	0.38
19.87	6.62	23.67	13.07	0.25
14.83	4.94	17.60	9.60	0.16
10.43	3.48	12.20	6.93	1.28
4.80	1.60	5.33	2.73	0.19
0.00	0.00	0.00	0.00	0.00

List of abbreviations

The following abbreviations are used in this thesis:

AoR Angle of Repose . . . 48
CoR Coefficient of Restitution . . . 5
CFD Computational Fluid Dynamics . . . 4
DEM Discrete Element Method . . . 4
DNS Direct Numerical Simulation . . . 11
FDM Finite Difference Method . . . 10
FEM Finite Element Method . . . 10
FVM Finite Volume Method . . . 10
IBM Immersed Boundary Method . . . 11
LBM Lattice Boltzmann Method . . . 11
MAPE Maximum Allowable Percent Error . . . 57
MFV Minimum Fluidization Velocity . . . 70
MSP Mono-Sized Particles . . . 83
PBC Periodic Boundary Condition . . . 86
PSD Particle Size Distribution . . . 48
PSP Poly-Sized Particles . . . 82
SPH Smoothed-Particle Hydrodynamics . . . 12
SPS Single Particle Sedimentation . . . 4
TFM Two-Fluid Model . . . 11
WBC Wall Boundary Condition . . . 86

Glossary

Below follows a list of the most frequently used symbols and notations in this thesis. For the sake of clarity, vectors are in bold font and scalars are in normal font.

Symbol	Description
Latin non capitals	
$\mathbf{a}$	Particle acceleration
e	Coefficient of restitution
$\boldsymbol{f}_{pp,i}$	Particle-particle contact force
$\boldsymbol{f}_{pf,i}$	Fluid-particle interaction force
$\boldsymbol{f}_{pp,i}$	Inter-particle collision force
$\boldsymbol{f}_{d,i}$	Drag force
$\boldsymbol{f}_{\bigtriangledown p,i}$	Pressure gradient force
$\boldsymbol{f}_{\bigtriangledown.\tau,i}$	Viscous force
$\boldsymbol{f}_{vm,i}$	Virtual mass force
$\boldsymbol{f}_{B}$	Basset force
$\boldsymbol{f}_{Saff}$	Saffman force
$\boldsymbol{f}_{Mag}$	Magnus force
$\boldsymbol{f}_{A,i}$	Archimedes force
k	Stiffness constant
k_e	Kinetic energy
k_c	Number of particles in collision with particle i
k_r	Rolling stiffness
ksl	Coefficient of momentum exchange
k_t	Tangential stiffness
l_{ip}	Length of impact plate
m_i	Mass of particle i
$m_i\boldsymbol{g}$	Gravitational force
m_{eff}	Effective mass
m_p	Mass of particles
t	Time
t_h	Hertz time step
t_r	Rayleigh time step
$\mathbf{u}_a$	Velocity of atmosphere B.C.

$\mathbf{u}_b$	Speed of belt conveyor
$\mathbf{u}_i$	Translational velocity of particle i
$\mathbf{u}_{fp}$	Superficial velocity
$\mathbf{u}_{ij}$	Relative velocity between particle i and j
$\mathbf{u}_{mf}$	Minimum Fluidization Velocity
$\mathbf{u}_t$	Terminal velocity of a particle
w_{ip}	Width of impact plate

Latin capitals

A_C	Acceleration number
A_v	Area of vessel
B_t	Belt thickness
C_A	Coefficient of the added mass
C_d	Drag coefficient
C_H	Coefficient of history term
D_{50}	Mass median diameter
D_h	Hydraulic diameter
D_p	Diameter of particle
CI	Coupling interval
E	Experimental result
E_{eff}	Effective Young's modulus
G	Shear modulus
G_{eff}	Effective shear modulus
H, h	Height
I_i	Moment of inertia for particle i
L, l	Length
$\boldsymbol{M}_i$	Momentum of particle i
$\boldsymbol{M}_r$	Momentum of rolling resistance
$\boldsymbol{M}_{r,ij}$	Rolling friction momentum between particle i and j
$\boldsymbol{M}_{t,ij}$	Tangential momentum between particle i and j
N_x	Number of CFD cells in x-direction
N_y	Number of CFD cells in y-direction
N_z	Number of CFD cells in z-direction
P_v	Perimeter of vessel
$\dot{Q}$	Volumetric flow rate
R	Reference value
R_{eff}	Effective radius
R_p	Radios of particle
R_r	Radios of roly
Re_p	Particle Reynolds number
Re_v	Vessel Reynolds number
S	Simulation result
V	Volume

V_b	Total volume of bed
V_f	Volume of bed occupied by fluid
$V_{p,i}$	Volume of particle i
W, w	Width

Greek non capitals

α_1	Inclination angle of conveyor
α_2	Inclination angle of impact plate
β_d	Dimensionless damping coefficient
γ	Visco-elastic damping constant
δ_{ij}	Overlap distance between particle i and j
ε_f	Fluid void fraction
ε_{mf}	Void fraction in Minimum Fluidization Velocity
ε_p	Particle void fraction
θ_r^m	Full mobilization rolling angle
μ_c	Coefficient of Coulomb friction
μ_f	Fluid viscosity
$\mu_{r,pb}$	Coefficient of rolling friction between particle-belt
$\mu_{r,ph}$	Coefficient of rolling friction between particle-impact plate
$\mu_{r,pp}$	Coefficient of rolling friction between particles
$\mu_{r,pw}$	Coefficient of rolling friction between particle-wall
$\mu_{s,pb}$	Coefficient of sliding friction between particle-belt
$\mu_{s,ph}$	Coefficient of sliding friction between particle-impact plate
$\mu_{s,pp}$	Coefficient of sliding friction between particles
$\mu_{s,pw}$	Coefficient of sliding friction between particle-wall
ν	Poisson ratio
ρ_f	Fluid density
ρ_p	Particle density
$\boldsymbol{\omega}_i$	Angular velocities of particle i

Greek capitals

Δp	Pressure drop
Δp_{exp}	Experimental pressure drop
Δp_{mf}	Pressure drop in Minimum Fluidization Velocity
Δt_{CFD}	CFD time step
Δt_{DEM}	DEM time step
Δx	CFD cell size in x-direction
Δy	CFD cell size in y-direction
Δz	CFD cell size in z-direction

Summary

Dust has negative effects on the environmental conditions, human health as well as industrial equipment and processes. In this thesis, the transfer point of a belt conveyor as a bulk material handling system with a very high potential place for dust liberation is studied. This study is conducted based on experimental and numerical methods as reliable tools in studying the dust liberation from bulk material handling systems.

The main objective of this thesis is to study the effect of design parameters on the rate of dust liberation at the transfer point with a numerical technique that is validated by experimental data. The following steps were taken to achieve the objectives of this thesis.

Firstly, a literature review was conducted to identify the proper numerical method for simulating dust liberation at the transfer point of a belt conveyor. It was concluded that a coupled CFD-DEM method is a cost effective, reliable, and accurate technique for modelling the inter-particle and particle-equipment collisions as well as simulating the airflow around a belt conveyor.

Secondly, the CFD-DEM model was calibrated, verified, and validated with the data to ensure that it is a realistic tool for simulating a dilute regime of particle flow through modelling a Single Particle Sedimentation (SPS). The SPS within water and silicon oil ($Re_p = 1.5$) was employed to calibrate the CFD-DEM model based on the terminal velocity of the particle. It was observed that the divided voidage model is not a proper voidage model where the ratio of domain width to particle diameter W/D_p is less than 10 while the big particle voidage model together with the ratio of particle diameter to the CFD cell size $D_p/\Delta x$ of 4 is applicable for $W/D_p > 5$ in the CFD-DEM model. Then, the sedimentation of a particle from air into water was used to verify the CFD-DEM model. Finally, the validation of the CFD-DEM model was assessed based on the experimental terminal velocity of a particle at different Reynolds numbers (Re_p=4.1, 11.6, and 31.9).

Thirdly, the CFD-DEM model was re-evaluated with experimental data for a dense regime of particle flow with a low rate of momentum exchange between the

particle and fluid phases. Quartz sand was used in this research, because it is the second most abundant mineral material on the surface of earth and the fine particles of the sand composition can be liberated as dust at the transfer point of a belt conveyor. For the model, it was assumed that the quartz sand consists of spherical, non-cohesive, and dried particles. The microscopic properties between sand particles such as coefficients of rolling and sliding friction ($\mu_{r,pp}$, $\mu_{s,pp}$) and its macroscopic properties like the Angle of Repose (AoR) and the discharging time of sand from an hourglass were experimentally and numerically determined to be used in subsequent parts of this research.

Fourthly, the experimental results of a fluidized bed were used to assess the CFD-DEM model at a high rate of momentum exchange between the particle and fluid phases. The effect of utilization of periodic and wall boundary conditions on the accuracy of the results was also investigated. In addition, mono-sized and poly-sized particles were utilized in the simulation to evaluate their effect on the macroscopic properties of the fluidized bed such as the pressure drop and size/shape of bubbles. At the end, the coefficient of restitution between particles and the coefficient of rolling and sliding friction between particles and walls were determined.

Finally, the CFD-DEM model together with the experimental investigations were used to determine the discharge trajectory of the sand particles. The influence of different factors such as the physical properties of materials and belt conveyor, the effect of surrounding air, and the working conditions of the belt conveyor on the dust liberation at the transfer point of a belt conveyor were studied. It was found that the segregation of materials at the transfer point due to the particle size and density is one of the important factors that should be considered in the design of belt conveyors. Also, the dominant factor at low Reynolds numbers ($Re < 0.5$) is the viscous force so that the fine particles in the order of $10\,\mu m$ are carried with the belt conveyor which constitutes a large portion of the dust. Therefore, recognition of the position of low pressure regions is a key factor in determining the location of the dust removal systems. These factors should be considered in the design of the transfer point of belt conveyor systems to reduce the rate of dust liberation from belt conveyor systems. It was concluded that the physical properties of materials and belt conveyor, the effect of surrounding air, and the working conditions of the belt conveyor are the important factors that should be considered in the design of the transfer point of a belt conveyor.

Samenvatting

Stof heeft negatieve effecten op milieu, gezondheid en industriële apparatuur en processen. In dit proefschrift wordt het overslagpunt van een transportband bestudeerd als systeem voor verwerking van bulkmateriaal met een zeer hoog potentieel voor stofontwikkeling. Het onderzoek is uitgevoerd met betrouwbare experimentele en numerieke methoden. De belangrijkste doelstelling van dit proefschrift is onderzoek naar de invloed van ontwerpparameters op de snelheid van stofontwikkeling bij het overslagpunt, waarbij een numerieke techniek is gebruikt die door experimentele gegevens is gevalideerd. Dit is in vijf stappen uitgevoerd.

Allereerst is er literatuuronderzoek uitgevoerd om vast te stellen wat de juiste numerieke methode is voor simulatie van stofontwikkeling bij het overslagpunt van een transportband. De conclusie is dat een gekoppelde CFD-DEM-methode een kostendekkende, betrouwbare en nauwkeurige techniek is voor het modelleren van botsingen tussen deeltjes onderling en tussen deeltjes en apparatuur, en ook voor simulatie van de luchtstroom rond een transportband.

In de tweede stap is het CFD-DEM-model gekalibreerd, geverifieerd en gevalideerd met de gegevens om te garanderen dat het een realistisch hulpmiddel is voor simulatie van een dunne deeltjesstroom, door middel van een model voor Single Particle Sedimentation (SPS, sedimentatie van één deeltje). SPS voor water en siliconenolie ($Re_p = 1.5$) is gebruikt om het CFD-DEM-model te kalibreren op basis van de eindsnelheid van het deeltje. Het gedeelde porositeitsmodel blijkt geen geschikt porositeitsmodel wanneer de verhouding tussen domeinbreedte en diameter van het deeltje W/D_p kleiner is dan 10, terwijl het grote deeltjes-porositeitsmodel - bij een verhouding van $D_p/\Delta x = 4$ tussen diameter van het deeltje en de CFD-celgrootte - van toepassing is voor $W/D_p > 5$ in het CFD-DEM-model. Vervolgens is het CFD-DEM-model geverifieerd met behulp van de sedimentatie van een deeltje uit de lucht in water. En ten slotte is het CFD-DEM-model gevalideerd op basis van de experimentele eindsnelheid van een deeltje bij verschillende Reynoldsgetallen (Re_p= 4,1, 11,6 en 31.9).

In de derde stap is het CFD-DEM-model opnieuw geëvalueerd met experimentele gegevens voor een dichte deeltjesstroom met een langzame impulsuitwisseling tussen

de deeltjesfase en de vloeibare fase. Bij dit onderzoek is kwartszand gebruikt, omdat dit het op een na meest voorkomende minerale materiaal aan de oppervlakte van de aarde is en de fijne deeltjes van het zand als stof kunnen vrijkomen bij het overslagpunt van een transportband. Voor het model is aangenomen dat kwartszand bestaat uit bolvormige, niet-samenhangende en droge deeltjes. De microscopische eigenschappen van de zanddeeltjes, zoals de coëfficiënten van rol- en glijwrijving ($\mu_{r,pp}$, $\mu_{s,pp}$), en de macroscopische eigenschappen, zoals de stort- of rusthoek (Angle of Repose, AoR) en de uitstromingssnelheid van zand uit een zandloper, zijn experimenteel en numeriek bepaald voor gebruik in latere onderdelen van dit onderzoek.

In de vierde stap zijn de experimentele resultaten van een wervelbed gebruikt om het CFD-DEM-model te beoordelen bij een snelle impulsuitwisseling tussen de deeltjesfase en de vloeibare fase. Het effect van het gebruik van periodieke en wandbegrensde omstandigheden op de nauwkeurigheid van de resultaten is ook onderzocht. Daarnaast zijn deeltjes met één grootte en met meerdere groottes gebruikt in de simulatie, om het effect daarvan op de macroscopische eigenschappen van het wervelbed, zoals drukdaling en de grootte en de vorm van bellen, te evalueren. Uiteindelijk zijn de restitutiecoëfficiënt tussen deeltjes onderling en de coëfficiënten van rol- en glijwrijving tussen deeltjes en wanden bepaald.

En ten slotte is het CFD-DEM-model in combinatie met experimenteel onderzoek gebruikt om het uitstroomtraject van de zanddeeltjes te bepalen. De invloed van verschillende factoren - zoals de fysische eigenschappen van materialen en de transportband, het effect van de omringende lucht en de werkomstandigheden van de transportband - op de stofontwikkeling bij het overslagpunt van een transportband is onderzocht. Er is geconstateerd dat de segregatie van materialen bij het overslagpunt als gevolg van de grootte en dichtheid van de deeltjes een van de belangrijke factoren is die in aanmerking moeten worden genomen bij het ontwerp van transportbanden. Ook geldt dat bij een laag Reynoldsgetal ($Re < 0.5$) de dominante factor de viskeuze kracht is, zodat fijne deeltjes van de orde van $10\,\mu m$ door de transportband worden meegenomen; dit vormt een groot deel van het stof. Voor het bepalen van de locatie van ontstoffingssystemen is daarom de positie van gebieden met lage druk een cruciale factor. Deze factoren moeten in aanmerking worden genomen bij het ontwerp van het overslagpunt van transportbandsystemen om stofontwikkeling hier te verminderen. De conclusie is dat de fysische eigenschappen van de materialen en de transportband, het effect van de omringende lucht en de werkomstandigheden van de transportband de belangrijke factoren zijn die in aanmerking moeten worden genomen bij het ontwerp van het overslagpunt van een transportband.

Acknowledgments

This period of my life passed in the blink of an eye. Thank you God for everything that you gave me and enabled me to successfully progress through this phase of life and I am sure your hidden and revealed favour will continue for the rest of my life.

I would like to compose this letter of appreciation to who supported me in the completion of this thesis. First and foremost, I am indebted to my PhD promoter, Professor Gabriel Lodewijks. You are a courageous gentleman and I have learned innumerable things from you professionally and personally and it is my great and true honour to be your PhD student. Second, I would like to thank Dr. Dingena Schott who was my wonderful co-promotor. I was under your direct supervision during the past four years of my PhD and, in my opinion, you are a meticulous and conscientious supervisor. I really enjoy your critical comments on my works and without your help it was not possible to finalize this research successfully. Thank you very much for supporting me and always being very kind to me.

During my PhD, I was so fortunate to interact with many experts within university and industry. I would like to thank Professor van Ommen for providing the possibility of doing my fluidized bed experiments in his laboratory and thank you Marjan for preparing the experimental set-up. Freek and Ed, I appreciate your helps and advises during the past years, also for the preparation of the experimental set-ups in a very short time. The conveyor set-up of DrySep B.V. and QToploader International B.V. helped me to validate my numerical model and to improve the quality of my research. Jos, I would like to thank you for your arrangements to use the conveyor set-up. Thank you very much, Josephina and Petty, for smoothly arranging all the things that I am continuously requesting from you during the past years.

My appreciation is also extended to my PhD committee members, Professor Boersma, Professor van Ommen, Professor Katterfeld, Professor Kuipers, and Doctor Thornton. Thank you for reviewing my PhD thesis and providing insightful comments in order to improve this dissertation.

I must send my gratitude to my friends and colleagues at TU Delft and University of Isfahan. I had a great time with my best room-mate, Stef, during the past four years who is a kind person regards to his international colleagues. Mohammad Jan, you are like a brother for me and supported me a lot especially when I left the Netherlands and you helped me arrange the official works of the defence ceremony. Amirreza Jan and Alireza Jan, thanks for your supports and hospitality at the last weeks before I left the Netherlands. Sadra Jan, Iman Jan, Mohammad Jan and Mahdi Jan, I appreciate your helps and advices during writing my thesis. Thank you all very much and many others who I have not named them.

My PhD journey might not have begun without the enormous support from my family, especially Baba and Maman Azizam, Nafiseh Jan and Agha Saeed, Amin Agha and Raziyeh Khanom, and my nephews and niece; Mohammad Jan, Sayed Mohammad, and Fatemeh Gole. Maman and Baba Aziz, my life transition from Esfahan to Mashhad, Mashhad to Tehran, and finally from Esfahan to Delft was so easy with your love and support. I am very indebted to you both.

Last, but not least, I would like to thank my dear wife, Faezeh Jan. During the past two years, which were the most crucial period of my PhD, you were so patient, supportive and helpful. I want to send my deepest gratitude to you. Thank you very much, Faezeh Jan, for your love, understanding my situation as well as late night work hours which sometimes lasted until midnight. Also, I would like to thank your dear family including Aghaye doctor and Khanom doctor, Mohammad Agha and Maedeh Khanom, Atefeh Khanom and Amin Khan.

Ebrahim
April 2016
Delft, The Netherlands

Publication

Journal papers:
S.M. Derakhshani, D.L. Schott, G. Lodewijks, Modelling dust liberation at the transfer point of a belt conveyor: Experimental investigation and CFD-DEM simulation, (Ready to be submitted).

S.M. Derakhshani, D.L. Schott, G. Lodewijks, Experimental study and CFD-DEM simulation of a Fluidized Bed of quartz Sand, (Ready to be submitted).

S.M. Derakhshani, D.L. Schott, G. Lodewijks, Modelling the Particle Sedimentation in the Viscous Fluid with the Coupled Immersed Boundary Method-Discrete Element Method, Particuology (Submitted).

S.M. Derakhshani, D.L. Schott, G. Lodewijks, Calibrating the microscopic properties of quartz sand with coupled CFD-DEM framework, Engineering Computations 2015 (Accepted).

S.M. Derakhshani, D.L. Schott, G. Lodewijks, Micro-macro properties of quartz Sand: Experimental investigation and DEM simulation, Powder Technol. (2014). doi:10.1016/j.powtec.2014.08.072.

Conference proceedings:
S.M. Derakhshani, D.L. Schott, G. Lodewijks, Assessing Reliability and Accuracy of IBM-DEM Coupling Method: Modelling Single Particle Sedimentation, 23rd Annual International Mechanical Engineering Conference, Amirkabir University of Technology, 12 May 2015.

S. M. Derakhshani, D. L. Schott, G. Lodewijks, 'Dust Emission Modelling around a Stockpile by Using Computational Fluid Dynamics and Discrete Element Method', Powders and Grains Conference, Sydney, Australia, July 8-12, 2013.

S. M. Derakhshani, D. L. Schott, G. Lodewijks, 'Modelling dust liberation at the belt conveyor transfer point with CFD and DEM coupling method', 11th International Congress on Bulk Materials Storage, Handling and Transportation, The University of Newcastle, July 2-4, 2013.

S. M. Derakhshani, D. L. Schott, G. Lodewijks, 'Reducing computational time by adjusting domain frame for fine granular materials with Discrete Element Method', Bulksolids Europe Conference, Berlin, Germany, October 2012.

About the Author

Sayed Mohammadebrahim Derakhshani was born in Isfahan, Iran. He studied Mechanical Engineering in the field of Thermo-Fluid mechanics at Ferdowsi University of Mashhad in Iran. In September 2007 he got his Master of Engineering degree in energy conversion engineering from Iran University of Science and Technology in Tehran, Iran. He then taught for four years at Ragheb university as a lecturer.

Sayed joined the section of Transport Engineering and Logistics at the faculty of Mechanical, Maritime and Material Engineering at Delft University of Technology in October 2011 as a PhD researcher. Studying the factors that affect the dust liberation from bulk material handling systems especially from the transfer point of a conveyor was the main goal of his research. During this period, he supervised the assignments and projects of master students related to his research; in addition, he contributed in a number of master courses at Delft University of Technology as an instructor.

Contact information:
Department of Mechanical Engineering,
Faculty of Engineering, University of Isfahan,
Isfahan, Iran

Email: e.derakhshani@gmail.com
Phone: +98 903 311 1559